

ISSN 0021-3438 (Print)  
ISSN 2412-8783 (Online)

**IZVESTIYA**

**NON-FERROUS  
METALLURGY**

**Vol. 30, No. 2, 2024**

Scientific and Technical Journal

Founded in 1958

4 Issues per year

**ИЗВЕСТИЯ ВУЗОВ**

**ЦВЕТНАЯ**

**МЕТАЛЛУРГИЯ**

**Том 30, № 2, 2024**

Научно-технический журнал

Основан в 1958 г.

Выходит 4 раза в год

IZVESTIYA

# NON-FERROUS METALLURGY

ISSN 0021-3438 (Print)  
ISSN 2412-8783 (Online)

Vol. 30, No. 2  
2024

Scientific and Technical Journal    Founded in 1958    4 Issues per year    <http://cvmet.misis.ru>

Journal is included into the List of the peer-reviewed scientific publications recommended by the Highest Attestation Commission of the Ministry of Education and Science of the Russian Federation for publishing the results of doctoral and candidate dissertations

Abstracting/Indexing: Russian Science Citation Index (RSCI), Chemical Abstracts (Online), INIS, OCLC ArticleFirst, Ulrich's Periodicals Directory, VINITI Database (Abstract Journal)

## Founder



National University of Science and Technology "MISIS"

Address: 4 build. 1 Leninskiy Prosp., Moscow 119049, Russia

<http://www.misis.ru>

## Editor-in-Chief

**Evgeny A. Levashov**

Prof., Dr. Sci. (Eng.), Acad. of the RANS, NUST MISIS, Moscow, Russia

## Deputy Editor

**Vladislava A. Ignatkina**

Prof., Dr. Sci., NUST MISIS, Moscow, Russia

## Editorial Board

**Abhilash** – Dr., Ph.D., CSIR – National Metallurgical Laboratory, Jamshedpur, India  
**E.V. Ageev** – Prof., Dr. Sci. (Eng.), SouthWest State University, Kursk, Russia  
**M.V. Ananyev** – Prof., Dr. Sci. (Chem.), Federal State Research and Development Institute of Rare Metal Industry (JSC "Giredmet"), Moscow, Russia  
**N.A. Belov** – Prof., Dr. Sci. (Eng.), NUST MISIS, Moscow, Russia  
**E.V. Bogatyreva** – Prof., Dr. Sci. (Eng.), NUST MISIS, Moscow, Russia  
**V.B. Deev** – Prof., Dr. Sci. (Eng.), NUST MISIS, Moscow, Russia  
**V.M. Denisov** – Prof., Dr. Sci. (Chem.), Siberian Federal University, Krasnoyarsk, Russia  
**D.V. Drobot** – Prof., Dr. Sci. (Chem.), Russian Technological University (MITHT), Moscow, Russia  
**F.V. Grechnikov** – Prof., Dr. Sci. (Eng.), Acad. of RAS, Samara National Research University n.a. S.P. Korolev (Samara University), Samara, Russia  
**D.V. Gunderov** – Dr. Sci. (Phys.-Math.), Institute of Molecule and Crystal Physics Ufa Research Center of the RAS, Ufa, Russia  
**B.B. Khina** – Dr. Sci. (Phys.-Math.), The Physical-Technical Institute of NAS of Belarus, Minsk, Belarus  
**D.V. Louzguine** – Prof., Dr. Sci., Tohoku University, Sendai, Japan  
**S.V. Mamychenkov** – Prof., Dr. Sci. (Eng.), Ural Federal University, Yekaterinburg, Russia  
**Z.A. Mansurov** – Dr. Sci. (Chem.), Prof., Institute of Combustion Problems, Almaty, Kazakhstan  
**N.V. Nemchinova** – Prof., Dr. Sci. (Eng.), Irkutsk National Research Technical University, Irkutsk, Russia  
**K.V. Nikitin** – Prof., Dr. Sci. (Eng.), Samara State Technical University, Samara, Russia  
**H.A. Oye** – Prof., Dr., Norwegian University of Science and Technology, Trondheim, Norway  
**P.V. Polyakov** – Prof., Dr. Sci. (Chem.), Siberian Federal University, Krasnoyarsk, Russia

**E.S. Prusov** – Cand. Sci. (Eng.), Vladimir State University, Vladimir, Russia  
**V.N. Richkov** – Prof., Dr. Sci. (Chem.), Ural Federal University, Ekaterinburg, Russia  
**D. Sadoway** – Prof., Dr., Massachusetts Institute of Technology, Boston, USA  
**G.A. Salishchev** – Prof., Dr. Sci. (Eng.), Belgorod National Research University, Belgorod, Russia  
**D.V. Shtansky** – Prof., Dr. Sci. (Phys.-Math.), NUST MISIS, Moscow, Russia  
**V.M. Sizyakov** – Prof., Dr. Sci. (Eng.), Saint-Petersburg Mining University, St. Petersburg, Russia  
**Stopic Srecko** – Dr.-Ing. habil., RWTH Aachen University, Aachen, Germany  
**B.B. Straumal** – Prof., Dr. Sci. (Phys.-Math.), Institute of Solid State Physics of the RAS, Chernogolovka, Moscow region  
**O.Yu. Tkacheva** – Dr. Sci. (Chem.), Institute of High Temperature Electrochemistry of the Ural Branch of the RAS, Yekaterinburg, Russia  
**M. Verhaege** – Prof., Dr., University of Gent, Belgium  
**G.M. Vol'dman** – Prof., Dr. Sci. (Chem.), Russian Technological University (MITHT), Moscow, Russia  
**G. Xanthopoulou** – Dr., National Center for Scientific Research "Demokritos", Agia Paraskevi, Attica, Greece  
**A.L. Yerokhin** – Prof., Dr., University of Manchester, United Kingdom  
**Onuralp Yücel** – Prof., Dr., Istanbul Technical University, Maslak, Istanbul, Turkey  
**Yu.P. Zaikov** – Prof., Dr. Sci. (Chem.), Institute of High Temperature Electrochemistry of the Ural Branch of the RAS, Yekaterinburg, Russia  
**R.Kh. Zalavutdinov** – Cand. Sci. (Phys.-Math.), A.N. Frumkin Institute of Physical Chemistry and Electrochemistry of the RAS, Moscow, Russia  
**M. Zinigrad** – Prof., Dr., Ariel University, Ariel, Israel  
**A.I. Zouboulis** – Prof., Dr., Aristotle University of Thessaloniki, Greece

## Editorial Staff

**Address:** NUST MISIS, 4 build. 1 Leninskiy Prosp., Moscow 119049, Russia

**Phone:** +7 (495) 638-45-35

**E-mail:** [izv.vuz@misis.ru](mailto:izv.vuz@misis.ru)

Certificate of registration No. 015842 (13.03.1997)

Re-registration PI No. ФС77-79229 (25.09.2020)

**Subscription:** Ural-Press Agency

**Leading Editor** – O.V. Sosnina

**Executive Editor** – A.A. Kudinova

**Layout Designer** – E.A. Legkaya

Signed print 24.06.2024. Format 60×90 1/8.

Offset paper No. 1. Digital printing. Quires 10,75

Order 20048. Free price

Printed in the printing house of the MISIS Publish House

4 build. 1 Leninskiy Prosp., Moscow 119049, Russia. Phone/fax: +7 (499) 236-76-17



© NUST MISIS, Moscow, 2024

© Izvestiya. Non-Ferrous Metallurgy, 2024



Articles are available under Creative Commons Attribution Non-Commercial No Derivatives

# ИЗВЕСТИЯ ВУЗОВ ЦВЕТНАЯ МЕТАЛЛУРГИЯ

ISSN 0021-3438 (Print)

ISSN 2412-8783 (Online)

## Том 30, № 2 2024

Научно-технический журнал Основан в 1958 г. Выходит 4 раза в год <http://cvmet.misis.ru>

Журнал включен в Перечень рецензируемых научных изданий, рекомендованных ВАК Минобрнауки РФ для публикации результатов диссертаций на соискание ученых степеней

Журнал включен в базы данных: Russian Science Citation Index (RSCI), Chemical Abstracts (Online), INIS, OCLC ArticleFirst, Ulrich's Periodicals Directory, РИНЦ, БД/РЖ ВИНТИ

### Учредитель



ФГАОУ ВО Национальный исследовательский технологический университет «МИСИС»  
Адрес: 119049, г. Москва, Ленинский пр-т, 4, стр. 1  
<http://www.misis.ru>

### Главный редактор

**Евгений Александрович Левашов**

д.т.н., академик РАЕН, профессор, НИТУ МИСИС, г. Москва

### Заместитель главного редактора

**Владислава Анатольевна Игнаткина**

д.т.н., профессор, НИТУ МИСИС, г. Москва

### Редакционная коллегия

**Е.В. Агеев** – д.т.н., ЮЗГУ, г. Курск  
**М.В. Ананьев** – д.х.н., АО «Гиредмет», г. Москва  
**Н.А. Белов** – д.т.н., проф., НИТУ МИСИС, г. Москва  
**Е.В. Богатырева** – д.т.н., НИТУ МИСИС, г. Москва  
**Г.М. Вольдман** – д.х.н., проф., РТУ (МИТХТ), г. Москва  
**Ф.В. Гречников** – д.т.н., акад. РАН, проф., СНИУ, г. Самара  
**Д.В. Гундеров** – д.ф.-м.н., ИФМК УНЦ РАН, г. Уфа  
**В.Б. Деев** – д.т.н., проф., НИТУ МИСИС, г. Москва  
**В.М. Денисов** – д.х.н., проф., СФУ, г. Красноярск  
**Д.В. Дробот** – д.х.н., проф., РТУ (МИТХТ), г. Москва  
**Ю.П. Зайков** – д.х.н., проф., ИВТЭ УрО РАН, г. Екатеринбург  
**Р.Х. Залавутдинов** – к.ф.-м.н., ИФХЭ РАН, г. Москва  
**С.В. Мамяченков** – д.т.н., проф., УрФУ, г. Екатеринбург  
**З.А. Мансуров** – д.х.н., проф., Институт проблем горения, г. Алматы, Казахстан  
**Н.В. Немчинова** – д.т.н., проф., ИРНИТУ, г. Иркутск  
**К.В. Никитин** – д.т.н., проф., СамГТУ, г. Самара  
**П.В. Поляков** – д.х.н., проф., СФУ, г. Красноярск  
**Е.С. Прусов** – к.т.н., доцент, ВлГУ, г. Владимир  
**В.Н. Рычков** – д.х.н., проф., УрФУ, г. Екатеринбург  
**Г.А. Салищев** – д.т.н., проф., НИУ «БелГУ», г. Белгород  
**В.М. Сизяков** – д.т.н., проф., СПГУ, г. Санкт-Петербург

**Б.Б. Страумал** – д.ф.-м.н., проф., ИФТТ РАН, г. Черноголовка  
**О.Ю. Ткачева** – д.х.н., ИВТЭ УрО РАН, г. Екатеринбург  
**Б.Б. Хина** – д.ф.-м.н., доц., ФТИ НАН Беларуси, г. Минск, Беларусь  
**Д.В. Штанский** – д.ф.-м.н., проф., НИТУ МИСИС, г. Москва  
**Abhilash** – Dr., Ph.D., CSIR – National Metallurgical Laboratory, Jamshedpur, India  
**D.V. Louzguine** – Prof., Dr., Tohoku University, Sendai, Japan  
**H.A. Oye** – Prof., Dr., Norwegian University of Science and Technology, Trondheim, Norway  
**D. Sadoway** – Prof., Dr., Massachusetts Institute of Technology, Boston, USA  
**Stopic Srecko** – Dr.-Ing. habil., RWTH Aachen University, Aachen, Germany  
**M. Verhaege** – Prof., Dr., University of Gent, Belgium  
**G. Xanthopoulou** – Dr., National Center for Scientific Research «Demokritos», Agia Paraskevi, Attica, Greece  
**A.L. Yerokhin** – Prof., Dr., University of Manchester, United Kingdom  
**Yücel Onuralp** – Prof., Dr., Istanbul Technical University, Maslak, Istanbul, Turkey  
**M. Zinigrad** – Prof., Dr., Ariel University, Ariel, Israel  
**A.I. Zouboulis** – Prof., Dr., Aristotle University of Thessaloniki, Greece

### Редакция журнала

Адрес: 119049, г. Москва, Ленинский пр-т, 4, стр. 1, НИТУ МИСИС

Тел.: +7 (495) 638-45-35

E-mail: [izv.vuz@misis.ru](mailto:izv.vuz@misis.ru)

Свидетельство о регистрации № 015842 от 13.03.1997 г.

Перерегистрация ПИ № ФС77-79229 от 25.09.2020 г.

Подписка: Агентство «Урал-пресс»

Ведущий редактор – О.В. Соснина

Выпускающий редактор – А.А. Кудинова

Дизайн и верстка – Е.А. Легкая

Подписано в печать 24.06.2024. Формат 60×90 1/8.

Бум. офсетная № 1. Печать цифровая. Усл. печ. л. 10,75

Заказ 20048. Цена свободная

Отпечатано в типографии Издательского Дома МИСИС

119049, г. Москва, Ленинский пр-т, 4, стр. 1. Тел./факс: +7 (499) 236-76-17



© НИТУ МИСИС, Москва, 2024

© «Известия вузов. Цветная металлургия», 2024



Статьи доступны под лицензией Creative Commons Attribution Non-Commercial No Derivatives

**Mineral Processing of Non-Ferrous Metals**

- 5 Lavrinenko A.A., Kuznetsova I.N., Golberg G.Yu., Lusinyan O.G.

Joint use of sodium silicate and polysaccharides in the flotation of talcose copper-nickel ores

**Physical Metallurgy and Heat Treatment**

- 16 Naumov S.V., Panov D.O., Chernichenko R.S., Sokolovsky V.S., Salishchev G.A., Alekseev E.B., Neulybin S.D., Belinin D.S., Shchitsyn Yu.D., Lukianov V.V.

Structure and mechanical properties of  $Ti_2AlNb$ -based alloy welded joints using keyhole plasma arc welding with subsequent heat treatment

- 30 Luts A.R., Sherina Yu.V., Amosov A.P., Minakov E.A., Ibatullin I.D.

Selection of heat treatment and its impact on the structure and properties of AK10M2N–10%TiC composite material obtained via SHS method in the melt

**Corrosion and Protection of Metals**

- 44 Buinachev S.V., Domashenkov M.A., Mashkovtsev M.A., Polivoda D.O., Zhirenkina N.V.

Synthesis and study of the properties of zirconium dioxide powders with different yttrium content

- 55 Akhmetov A., Eremeeva Zh.V., Kudryashov A.E., Loginov P.A., Shlyapin S.D., Samoshina M.E., Levashov E.A.

Fabrication of high speed steel electrodes with  $MoSi_2$ –MoB–HfB<sub>2</sub> ceramic additives for electrospark deposition on die steel

- 70 Mukanov S.K., Petrzhik M.I., Loginov P.A., Levashov E.A.

Influence of manganese alloying on the structure and properties of electrospark coatings of EP741NP heat-resistant nickel LPBF alloy

**Chronicle**

- 85 In memory of Lev Iosifovich Klyachko

**Обогащение руд цветных металлов**

- 5 Лавриненко А.А., Кузнецова И.Н., Гольберг Г.Ю., Лусинян О.Г.

Совместное применение жидкого стекла и полисахаридов при флотации оталькованных медно-никелевых руд

**Металловедение и термическая обработка**

- 16 Наумов С.В., Панов Д.О., Черниченко Р.С., Соколовский В.С., Салишев Г.А., Алексеев Е.Б., Неулыбин С.Д., Белинин Д.С., Щицын Ю.Д., Лукьянов В.В.

Структура и механические свойства сварных соединений из сплава на основе орторомбического алюминид титана, полученных плазменной сваркой проникающей дугой с последующей термической обработкой

- 30 Луц А.Р., Шерина Ю.В., Амосов А.П., Минаков Е.А., Ибатуллин И.Д.

Выбор термической обработки и исследование ее влияния на структуру и свойства композиционного материала АК10М2Н–10%TiC, полученного методом СВС в расплаве

**Коррозия и защита металлов**

- 44 Буйначев С.В., Домашенков М.А., Машковцев М.А., Поливода Д.О., Жиренкина Н.В.

Синтез и исследование свойств порошков диоксида циркония с различным содержанием иттрия

- 55 Ахметов А., Еремеева Ж.В., Кудряшов А.Е., Логинов П.А., Шляпин С.Д., Самошина М.Е., Левашов Е.А.

Получение электрода из быстрорежущей стали с керамической добавкой  $MoSi_2$ –MoB–HfB<sub>2</sub> для электроискровой обработки штамповой стали

- 70 Муканов С.К., Петржик М.И., Логинов П.А., Левашов Е.А.

Влияние легирования марганцем на структуру и свойства электроискровых покрытий на никелевом жаропрочном СЛС-сплаве ЭП741НП

**Хроника**

- 85 Памяти Льва Иосифовича Клячко

UDC 622.765

<https://doi.org/10.17073/0021-3438-2024-2-5-15>

Research article

Научная статья



## Joint use of sodium silicate and polysaccharides in the flotation of talcose copper-nickel ores

A.A. Lavrinenko, I.N. Kuznetsova, G.Yu. Golberg, O.G. Lusinyan

Institute of Comprehensive Exploitation of Mineral Resources n.a. Academician N.V. Melnikov of the Russian Academy of Sciences

4 Kryukovskiy impasse, Moscow 111020, Russia

✉ Anatoliy A. Lavrinenko (lavrin\_a@mail.ru)

**Abstract:** The paper considers the combined effect of polysaccharides (carboxymethyl cellulose and carboxymethyl starch) with sodium silicate in the flotation of talcose copper-nickel ore. The analysis of the flotation results and the assessment of hydrophobicity and surface charge of minerals showed that the composition of carboxymethylated polysaccharides and sodium silicate hydrophilizes the talc surface more effectively than each of the reagents separately. Moreover, sodium silicate alone hardly depresses the talc surface at all. The depression of flotation-active silicates is effective when polysaccharide and sodium silicate are sequentially supplied. Under these conditions, sodium silicate makes a significant contribution to increasing the negative charge on the talc particles surface. The effect is more pronounced for compositions with starch, characterized by a lower degree of substitution compared to cellulose. It results in a significantly reduced recovery of flotation-active magnesium-containing silicates and a slight decrease in sulfide recovery. To determine the features of the mechanism of talc and sulfide minerals depression in flotation, we performed calculations using the extended DLVO theory based on the obtained values of the zeta potential and force of detachment. We established that sulfide minerals have no potential barrier preventing their interaction with an air bubble, regardless of the compositions of the studied depressants used. We propose the following interaction mechanism: when sodium silicate is supplied first, the talc basal surface is very insignificantly hydrophilized as  $\text{SiO}(\text{OH})_3^-$  ions are not easy to fix. On the contrary, when the carboxymethylated polysaccharide is supplied first, significant hydrophilization of the talc surface with carboxyl groups occurs due to the hydrophobic interaction between the corresponding regions of the macromolecule and the talc basal surface.

**Keywords:** flotation, hydrophobicity, zeta potential, talc, sodium silicate, carboxymethyl cellulose, carboxymethyl starch, copper-nickel ore.

**For citation:** Lavrinenko A.A., Kuznetsova I.N., Golberg G.Yu., Lusinyan O.G. Joint use of sodium silicate and polysaccharides in the flotation of talcose copper-nickel ores. *Izvestiya. Non-Ferrous Metallurgy*. 2024;30(2):5–15.

<https://doi.org/10.17073/0021-3438-2024-2-5-15>

## Совместное применение жидкого стекла и полисахаридов при флотации оталькованных медно-никелевых руд

А.А. Лавриненко, И.Н. Кузнецова, Г.Ю. Гольберг, О.Г. Лусинян

Институт проблем комплексного освоения недр им. академика Н.В. Мельникова Российской академии наук  
Россия, 111020, г. Москва, Крюковский тупик, 4

✉ Анатолий Афанасьевич Лавриненко (lavrin\_a@mail.ru)

**Аннотация:** Рассмотрено совместное действие полисахаридов (карбоксиметилированной целлюлозы и карбоксиметилированного крахмала) с жидким стеклом при флотации оталькованной медно-никелевой руды. На основании анализа результатов фло-

тации, оценки гидрофобности и поверхностного заряда минералов показано, что композиция карбоксиметилированных полисахаридов и жидкого стекла гидрофилизует поверхность талька более эффективно, чем каждый из реагентов по отдельности. При этом одно жидкое стекло почти не депрессирует поверхность талька. Эффективная депрессия флотоактивных силикатов достигается при последовательной подаче полисахарида и жидкого стекла. В этих условиях жидкое стекло вносит существенный вклад в увеличение отрицательного заряда поверхности частиц талька. Эффект проявляется в большей мере для композиции с крахмалом, имеющим более низкую степень замещения по сравнению с целлюлозой. В результате существенно падает извлечение флотоактивных магнийсодержащих силикатов при небольшом снижении извлечения сульфидов. С целью определения особенностей механизма депрессии талька и сульфидных минералов при флотации на основании полученных данных по значениям электрокинетического потенциала и силы отрыва были выполнены расчеты по расширенной теории ДЛФО. Установлено, что для сульфидных минералов потенциальный барьер их взаимодействия с пузырьком воздуха отсутствует при применении любых композиций исследованных депрессоров. Предложен следующий механизм взаимодействия: в случае, если в первую очередь подается жидкое стекло, то гидрофилизация базальной поверхности талька весьма незначительна по причине затруднения закрепления ионов  $\text{SiO}(\text{OH})_3^-$ ; напротив, когда сначала вводится карбоксиметилированный полисахарид, происходит существенная гидрофилизация поверхности талька карбоксильными группами вследствие гидрофобного взаимодействия между соответствующими участками макромолекулы и базальной поверхности талька.

**Ключевые слова:** флотация, гидрофобность, электрокинетический потенциал, тальк, жидкое стекло, карбоксиметилированная целлюлоза, карбоксиметилированный крахмал, медно-никелевая руда.

**Для цитирования:** Лавриненко А.А., Кузнецова И.Н., Гольберг Г.Ю., Лусинян О.Г. Совместное применение жидкого стекла и полисахаридов при флотации оталькованных медно-никелевых руд. *Известия вузов. Цветная металлургия*. 2024;30(2):5–15. <https://doi.org/10.17073/0021-3438-2024-2-5-15>

## Introduction

Efficient depression of rock minerals is crucial in the flotation of copper nickel ores since naturally hydrophobic talc and other flotation-active magnesium-containing silicates may easily be recovered into the flotation concentrate, increasing the costs of further pyrometallurgical processing. Plant-based polysaccharides are widely used for talc depression [1]. Earlier research focused on various talc depressants, including the most effective one — carboxymethyl cellulose (CMC) [2]. The main difficulty in applying polysaccharides is their selectivity. With an increased molecular weight of the reagent, depressing ability improves, but the sulfides recovery in the concentrate deteriorates [3–7]. Therefore, it is important to look for ways to boost selectivity and reduce recovery of magnesium-containing silicates in the concentrate when using depressants of flotation-active rock minerals.

An analysis of literature data on the use of reagent complexes and their mechanism of action in the flotation of talcose copper-nickel ores proved the viability of using compositions of sodium silicate (SS) with carboxymethylated polysaccharides [8–12]. According to [13], the sequential supply of acidified sodium silicate (SS) and CMC enhances the efficiency of flotation separation of chalcopryrite and talc due to the hydrophilization of talc basal surfaces by polymeric silicic acid formed during SS acidification. Thus, in the flotation with a CMC concentration of 500 mg/L,

the recovery of chalcopryrite and talc in the concentrate amounted to 16 % and 45 % respectively, against 95 % and 90 % without a depressant. Moreover, the addition of acidified SS only during the flotation had practically no impact on the recovery of these minerals in the concentrate.

However, researchers in [14] note that the addition of sodium silicate acidified with oxalic or hydrochloric acids reduces the floatability of silicates. At the same time, the sequential supply of these depressants with an SS concentration of 250 mg/L and a CMC concentration of 300 mg/L ensured, respectively, 28 % and 43 % recovery of talc and chalcopryrite in the concentrate. The paper [15] showed that in the talc flotation with the pH medium increasing from 8.6 to 10.5 and the non-acidified SS concentration surging from 0 to 300 mg/l, the recovery of talc in the concentrate rises from 70 % to 78 %. However, with a further increase in pH and SS consumption, it drops, which, in our opinion, can be attributed to the enhanced concentration of double-charged anions  $\text{SiO}_2(\text{OH})_2^{2-}$  at pH above 10.5. It is also indicated that the use of CMC in combination with SS causes a reduction of roughly 7 % in the talc recovery in the concentrate. At the same time, it remains unclear how the order of feeding non-acidified SS and polysaccharides affects the surface properties of talc, sulfide minerals, and, in general, the results of talcose copper-nickel ore flotation.

Many researchers [12; 15; 16 et al.] attribute the depressing effect of sodium silicate to the hindrance of the collector's sorption on the mineral surface. Non-acidified SS is known to have a depressing effect on quartz in a weakly alkaline medium as  $\text{SiO}(\text{OH})_3^-$  ions are fixed on its surface [17]. It also affects flotation-active forsterite (forming a chemical compound with magnesium [18]) and serpentine in a strongly alkaline medium, as the positive surface charge of these minerals is compensated by  $\text{SiO}_2(\text{OH})_2^{2-}$  anions [19]. Thus, SS impacts silicate minerals through different mechanisms of depression.

The literature data on the properties of SS solutions (e.g., [20]) indicate that the molecular form  $\text{H}_4\text{SiO}_4$  predominates in a slightly alkaline medium at  $\text{pH} = 7.0 \div 9.4$ , with single-charged anions  $\text{SiO}(\text{OH})_3^-$  are also present in relatively small amounts. Considering that about 90 % of the surface of talc particles is represented by basal areas characterized by very high hydrophobicity due to relatively low-polarity Si—O bonds prevailing [21], there are reasons to believe that the adsorption value of  $\text{Si}(\text{OH})_4$  and  $\text{SiO}(\text{OH})_3^-$  in a weakly alkaline medium is relatively small. This is probably why these compounds do not contribute to talc hydrophilization or an increase in the absolute value of the negative  $\zeta$ -potential of the surface. The findings of [15] also support this assumption.

The purpose of this work is to determine, using the example of flotation of out-of-balance copper-nickel ore, the conditions under which compositions of non-acidified sodium silicate and polysaccharide depressants have a potent depressing effect on flotation-active silicates.

The objective of the research was to find out how depressants should be applied to reduce the concentrate yield while maintaining acceptable copper and nickel recovery.

## Materials and methods

The research aims to study the depressing effect of depressant compositions on talc and other flotation-active silicates in the flotation of talcose copper-nickel ore.

For flotation experiments, we used the ore comprising the following major elements, %:

Cu .....	0.12
Ni .....	0.2
Co .....	0.01
S .....	0.8
Fe .....	1.9
Mg .....	0.94
$\text{SiO}_2$ .....	50.5

Its mineral composition includes the following elements, wt.%:

Chalcopyrite .....	0.3
Pentlandite .....	0.6
Pyrrhotite .....	0.2
Pyrite .....	0.14
Pyroxene .....	58
Talc .....	12
Amphiboles .....	8
Magnesite .....	3.75
Plagioclases .....	1

By the content of valuable components, the ore is classified as out-of-balance.

The scheme shown in Fig. 1 was used to conduct flotation of the ore crushed to a size of 84 % grade  $-71 \mu\text{m}$ , at  $\text{pH} = 7$  (generated by the flotation medium). In the main flotation, the silicate depressant was fed first, to be followed by the collector — butyl xanthogenate 50 g/t. Methylisobutylcarbinol (MIBC), with consumption of 20 g/t, was used as a foaming agent. Reagent consumption in the control flotation amounted to 40 % of that in the main flotation. The concentrates from the main and control flotations were then combined. The following reagents were used as talc depressants:

- sodium silicate;
- carboxymethyl starch CMS-BUR (JSC NPO “Polycell”, Russia), with 0.4 degree of substitution of hydroxyl groups by carboxyl ones and 60 % content of the active substance;
- carboxymethyl cellulose (polyanionic cellulose) PAC-N (JSC NPO “Polycell”) with a 0.9 degree of substitution at 45 % of active substance.

Depressants concentrations and consumption were recalculated taking into account the content of the active ingredient in the reagent.

The changes in the minerals hydrophobicity caused by depressants were evaluated by determining the force of air bubble detachment from the mineral surface using a torsion balances. Sections of natural samples of pyrrhotite, pentlandite, and talc were measured [22]. NaOH was used to provide a  $\text{pH} = 7$  solution.

The zeta potential of the minerals was determined using a ZETA-check PMX 500 device (“Particle Metrix”, USA). A 0.2 g sample of finely ground mineral was placed in a 50 ml cell. The measurement principle is based on the evaluation of the flow potential.

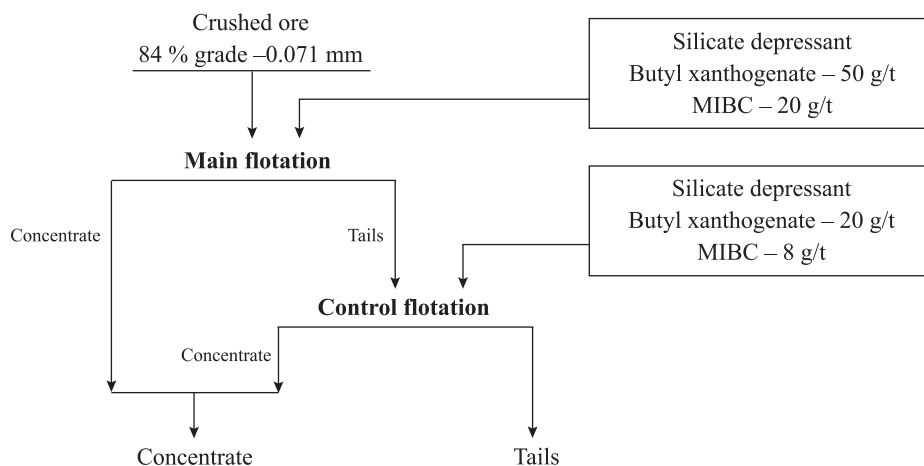


Fig. 1. Scheme of flotation experiments

Рис. 1. Схема флотационных опытов

## Results and discussion

Figure 2 shows the findings of flotation studies of copper-nickel ore with sodium silicate, carboxymethyl starch, and carboxymethyl cellulose, as well as combinations of SS + CMS-BUR and SS + PAC-N. Based on the analysis, we came to the following conclusions: sodium silicate does not significantly depress rock minerals; the concentrate yield decreased by 10 % from 52.9 % to 42.8 %, at an SS consumption of 5.6 kg/t. The PAC-N reagent demonstrates better depressing properties compared to CMS-BUR. At the same consumption of 700 g/t, the use of CMS-BUR reduced the concentrate yield from 52.9 % to 40.9 %, PAC-N reduced it to 22.6 %. The combinations of depressants in the compositions of SS + CMS-BUR and SS + PAC-N showed stronger depressant properties compared to each reagent separately. When the combination of SS + CMS-BUR is used, the order of feeding the depressant is important. When SS is introduced first, followed by CMS-BUR, the concentrate yield drops to 27.9 %. However, if SS is fed after starch, the yield plummets to 18.8 % (see Fig. 2, a). Therefore, it is recommended to feed SS after CMS-BUR. The combined use of PAC-N and SS also enhances the depressing effect in the flotation (see Fig. 2, b), but the order of feeding reagents does not significantly affect the result. With an SS consumption of 5.6 kg/t and PAC-N consumption of 700 g/t, the concentrate yield decreases from 52.9 % to 15.9 %. For the composition CMS-BUR + SS, the minimum required depressant consumption is 280 g/t of starch and 1.4 kg/t of SS, and its further increase does not affect depression (see Fig. 2, a). When PAC-N + SS is used, the concen-

trate yield gradually declines with increasing reagent consumption (see Fig. 2, b). 1.4 kg/t of SS; further increases do not affect depression (see Fig. 2, a). When PAC-N + SS is used, the concentrate yield gradually declines with increasing reagent consumption (see Fig. 2, b).

Figure 3 shows the results of copper and nickel recovery into the concentrate using compositions of SS + CMS-BUR and SS + PAC-N depressants. With an SS consumption of 5.6 kg/t and polysaccharide consumption of 700 g/t, CMS-BUR showed slightly better selectivity for nickel: nickel recovery was 58.6 %, while with PAC-N, this value was 54.4 %.

The results of measurements of the air bubble detachment force from the talc surface showed that the combined use of depressants (Fig. 4, a, curves 4 and 5) increases the hydrophilization of the mineral surface compared to each depressant used individually. For pentlandite and pyrrhotite (Fig. 4, b and c), the compositions reduce the hydrophobicity of sulfides, but to a lesser extent than for talc. Thus, for talc with the maximum concentration of each depressant (600 mg/L), the detachment force drops from 300  $\mu\text{N}$  to 50  $\mu\text{N}$ , while for sulfides under the same conditions, it decreases by 50–60  $\mu\text{N}$  to 280–290  $\mu\text{N}$ . It was found that the different order of feeding depressants barely affects the force of air bubble detachment from the mineral surface.

The zeta  $\zeta$ -potential of talc shifts more in the presence of different depressants (Fig. 5, a) when sodium silicate is added. With its content of 250 mg/L, the value of  $\zeta$ -potential is –48 mV, while with the same concentration of CMS-BUR and PAC-N, it is about –35 mV. The effect of SS addition to polysaccharides is most pro-

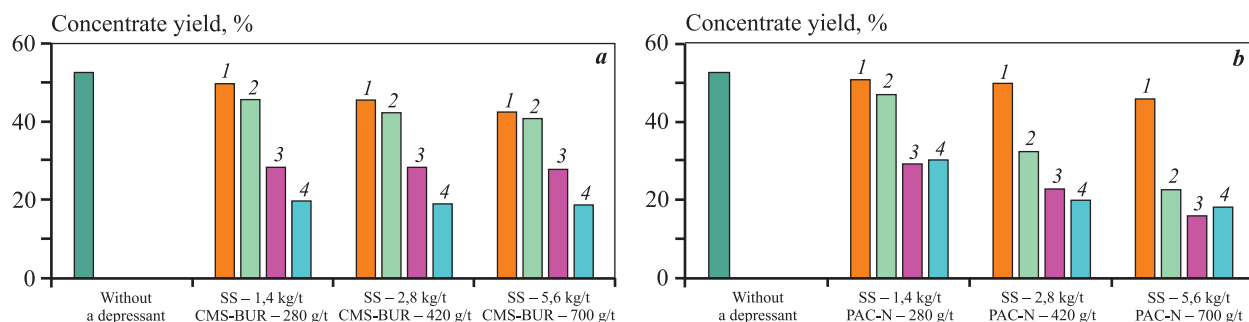


**Fig. 2.** Impact of the composition of depressants CMC-BUR with SS (a) and PAC-N with SS (b) on the concentrate yield in the flotation of copper nickel ore

a: 1 – SS, 2 – CMS-BUR, 3 – SS + CMS-BUR, 4 – CMS-BUR + SS

b: 1 – SS, 2 – PAC-N, 3 – SS + PAC-N, 4 – PAC-N + SS

**Рис. 2.** Влияние сочетания депрессоров КМК-БУР с ЖС (a) и ПАЦ-Н с ЖС (b) на выход концентрата при флотации медно-никелевой руды

a: 1 – ЖС, 2 – КМК-БУР, 3 – ЖС + КМК-БУР, 4 – КМК-БУР + ЖС

b: 1 – ЖС, 2 – ПАЦ-Н, 3 – ЖС + ПАЦ-Н, 4 – ПАЦ-Н + ЖС

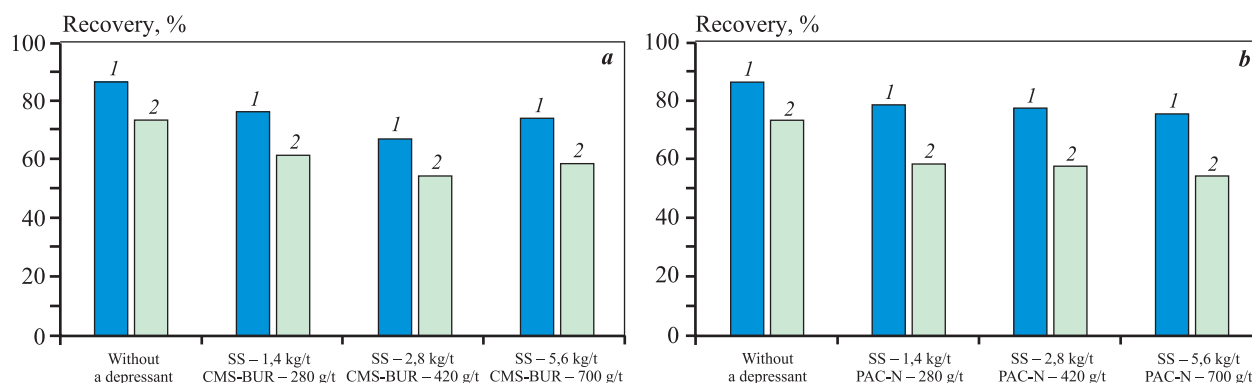


**Fig. 3.** Impact of the composition of depressants CMS-BUR + SS (a) and PAC-N + SS (b) on the recovery of Cu (1) and Ni (2) in the flotation of copper nickel ore

**Рис. 3.** Влияние композиции депрессоров КМК-БУР + ЖС (a) и ПАЦ-Н + ЖС (b) на извлечение Cu (1) и Ni (2) при флотации медно-никелевой руды

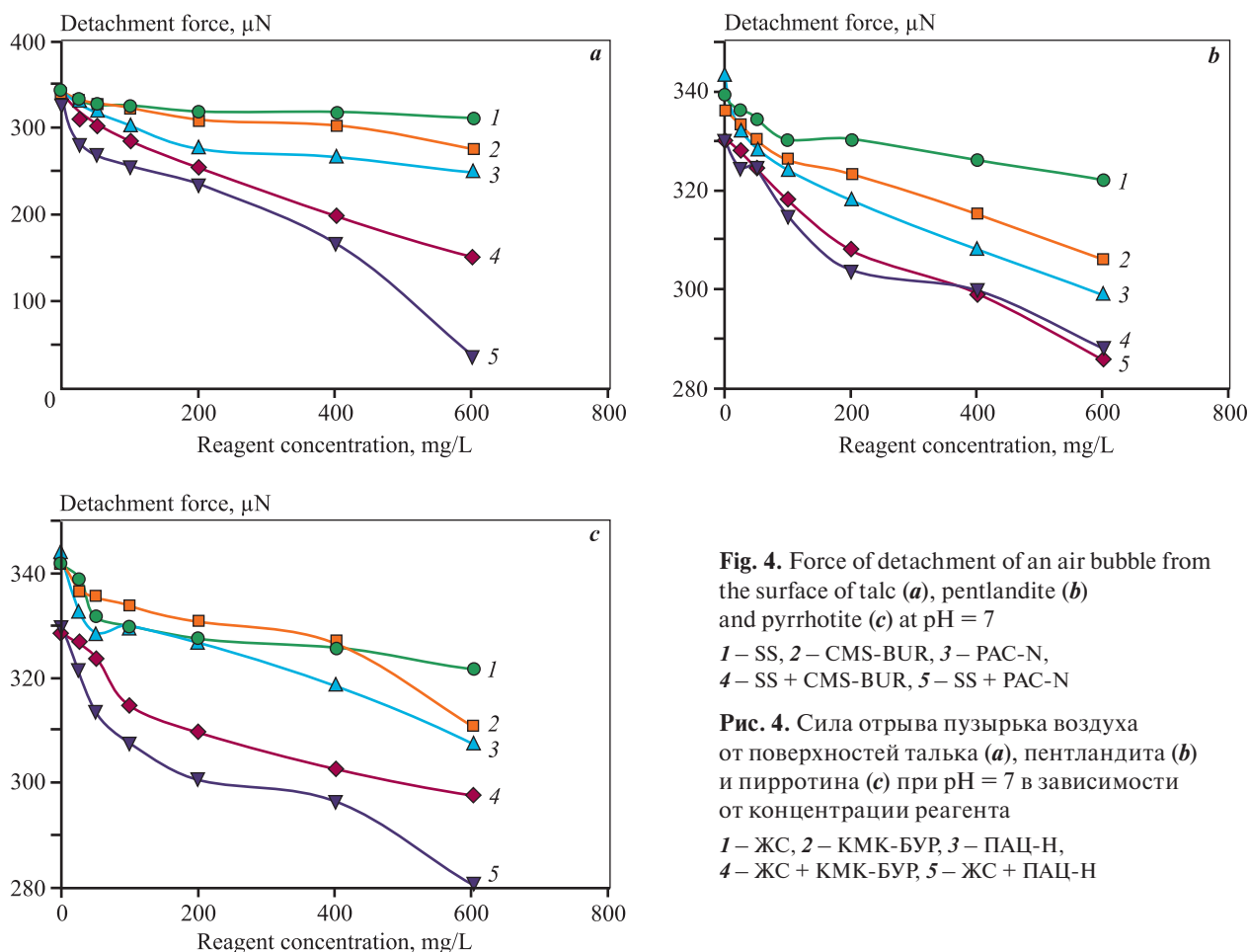
nounced with its content of 100 mg/L. When the concentration of polysaccharide was increased to 250 mg/L, the value of  $\zeta$ -potential was close to that in the presence of one SS.

For chalcopyrite, the shift of  $\zeta$ -potential was almost the same regardless of the depressant (Fig. 5, b). The value of zeta potential of chalcopyrite without reagents is  $-4$  mV, while in the presence of CMS-BUR and PAC-N, the concentration of each being 250 mg/L, it reaches  $-8.5$  mV, and when SS is added, this value amounts to about  $-10$  mV. The combination of depressants, with 100 mg/L SS concentration and 250 mg/L polysaccharide concentration, shifts the potential to  $-10$  mV.

The zeta potential of pyrrhotite without reagents reaches  $-8.8$  mV (Fig. 5, c), and it shifts more when sodium silicate is added. The combination of depressants shifts the potential toward negative values by 1–2 mV up to 11 mV.

Thus, when depressants affect talc at a concentration of 250 mg/L, the zeta potential shifts from the initial value by 16–28 mV to the values of  $-36$ ... $-48$  mV depending on the depressant. For sulfides (pyrrhotite and chalcopyrite)  $\zeta$ -potential is  $-8$ ... $-10$  mV with a shift from the initial one by 1–2 mV towards negative values.

To determine the features of the mechanism of talc and sulfide minerals depression in the flotation based



on the obtained values of the zeta potential and detachment force, we made calculations using the extended DLVO theory, taking into account the components of the potential energy of interaction between a mineral particle and an air bubble: electrostatic ( $U_E$  with the “+” sign), molecular ( $U_M$  with the “–” sign) and hydrophobic ( $U_H$  with the “–” sign). The calculation method based on this theory for talc depression is described in [23]. According to [24], if the curve showing dependence of the total potential energy ( $U$ ) of the particle interaction with a bubble on the distance between the surfaces of these objects ( $h$ ) has a barrier with a height of minimum  $10 kT$  (where  $k = 1.38 \cdot 10^{-23}$  J/K – Boltzmann constant;  $T$  – absolute temperature, K), the interaction of these objects is hampered. When the barrier is lower or non-existent, the interaction is unimpeded.

Considering the literature data, the following parameter values included in the equation of the extended DLVO theory were used in the calculations:

– ionic strength of the dispersion medium – 0.04 mol/L;

– Hamaker constants for talc particles and air bubbles are  $1.7 \cdot 10^{-20}$  and  $3.7 \cdot 10^{-20}$  J, respectively;

– the surface potential ( $\phi$ ) of air bubbles in the aqueous medium at pH = 7, according to various data, ranges from  $-0.037$  to  $-0.265$  V.

Figures 6 and 7 features the calculated curves of  $U$  dependence on  $h$  at pH = 7. The presented data demonstrates that in the absence of reagents the calculated curve is entirely in the region of negative  $U$  values, since talc particles, due to their natural hydrophobicity, freely interact with air bubbles. In the presence of individual reagents, including SS, CMS-BUR and PAC-N, maxima emerge on the curves corresponding to the value of  $h \sim 2\text{--}3$  nm. They are located above the curve for the reagentless mode, but still entirely within the region of negative values, even when the consumption of investigated reagents is at its maximum.

Figure 6 also shows that curve 4 corresponding to SS is located above curves 2 and 3 for PAC-N and CMS-BUR. We attribute this to the fact that some part of carboxyl groups does not participate in forming the

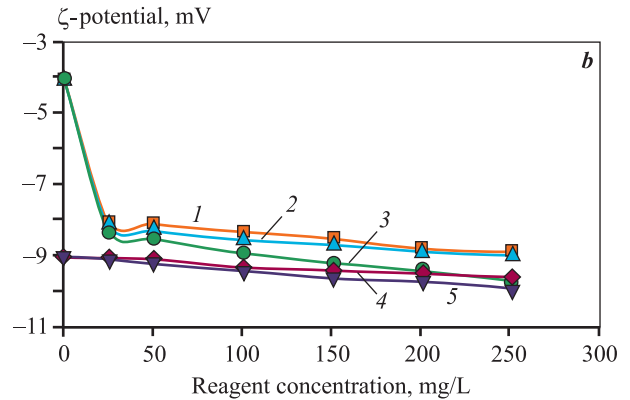
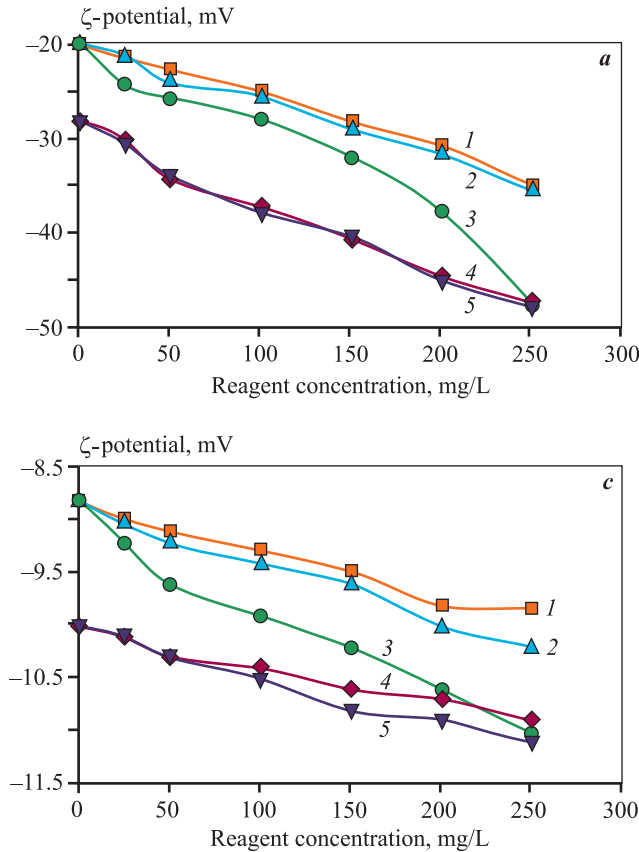


**Fig. 5.**  $\zeta$ -potential of talc (a), chalcopyrite (b) and pyrrhotite (c) with different depressants at pH = 7  
 1 – CMS-BUR, 2 – PAC-N, 3 – SS,  
 4 – SS (100 mg/l) + CMS-BUR,  
 5 – SS (100 mg/l) + PAC-N

**Рис. 5.**  $\zeta$ -потенциал талька (a), халькопирита (b) и пирротина (c) с разными депрессорами при pH = 7 в зависимости от концентрации реагента  
 1 – КМК-БУР, 2 – ПАЦ-Н, 3 – ЖС,  
 4 – ЖС (100 мг/л) + КМК-БУР,  
 5 – ЖС (100 мг/л) + ПАЦ-Н

negative charge of the talc surface due to steric hindrances and incomplete dissociation. At the same time, silicic acid ions are characterized by a denser arrangement on the talc surface, which causes a greater negative charge and, consequently, a greater value of the electrostatic component.

Figure 7 shows that the use of PAC-N composition with SS creates a potential barrier of interaction between the particle and the bubble with an ordinate of about  $10 kT$ . This is presumably due to the fact that PAC-H hydrophilizes the talc surface with carboxyl groups. This, in turn, creates favorable conditions for additional hydrophilization of talc by  $\text{SiO}(\text{OH})_3^-$  ions and increase in the negative charge of the surface. At the same time, compared to the mode without reagent supply at the point corresponding to the maximum height of the potential barrier ( $h = 1.7 \text{ nm}$ ), the value of  $U_E$  is 4.5 times higher, and that of  $U_H$  is 1.4 times lower. This gives reasons to suggest that the electrostatic component makes the most significant contribution to the barrier formation due to the increased number of negatively charged groups on the talc surface. This effect is the greatest for PAC-H, for which the degree of substitution is 0.9. At the same time, CMS-BUR, characterized by a much lower degree of substitution

(0.4), cannot create a potential barrier under the same conditions.

Also, the calculations revealed that for sulfide minerals, there was no potential barrier in their interaction with an air bubble no matter what compositions of investigated depressants were used.

Based on the above, the following mechanism of talc depression by the compositions of polysaccharides and SS seems feasible. If SS is fed first, the hydrophilization of the basal surface of talc is insignificant as  $\text{SiO}(\text{OH})_3^-$  ions are not easy to fix. On the contrary, when the carboxymethylated polysaccharide is fed first, according to the detachment force measurement data, the talc surface is substantially hydrophilized by the carboxyl groups due to hydrophobic interactions between the corresponding sites of the macromolecule and the talc basal surface. This, in turn, creates favorable conditions for additional hydrophilization of talc by  $\text{SiO}(\text{OH})_3^-$  ions, and their contribution to the increase in the negative charge of the surface is more noticeable for the CMC-BUR reagent with a 0.4 degree of substitution compared to PAC-N, for which this parameter is 0.9.

Thus, the depressant reagents decrease the hydrophobic component and increase the electrostatic one due to their negative charge.

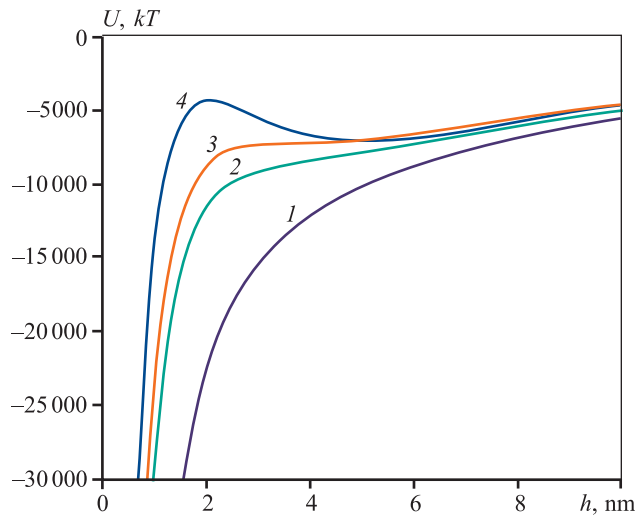


**Fig. 6.** Potential curves illustrating the interaction of air bubbles and talc particles with individual depressants in the quantity of 250 mg/L each at pH = 7

1 – without reagents, 2 – CMS-BUR, 3 – PAC-N, 4 – SS

**Рис. 6.** Потенциальные кривые взаимодействия пузырьков воздуха и частиц талька с индивидуальными депрессорами в количестве 250 мг/л каждого при pH = 7

1 – без реагентов, 2 – КМК-БУР, 3 – ПАЦ-Н, 4 – ЖС

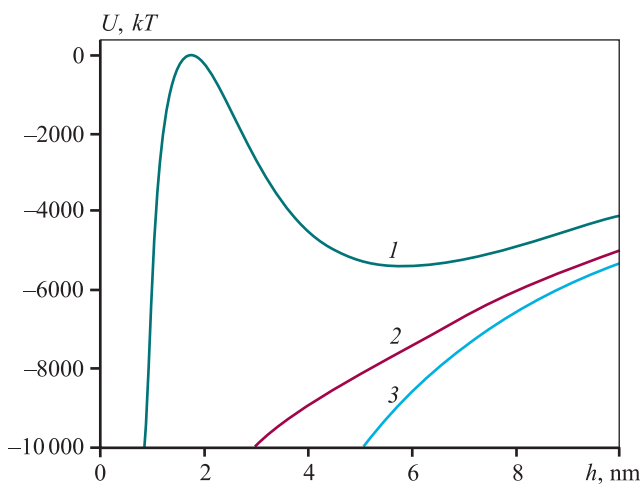


**Fig. 7.** Potential curves illustrating the interaction of air bubbles, talc particles (1, 2) and pyrrhotite (3) with depressant compositions

1 – PAC-N + SS, 2 – CMS-BUR + SS, 3 – PAC-N + SS  
Concentrations: SS – 100 mg/L, CMS-BUR – 250 mg/L, PAC-N – 250 mg/L

**Рис. 7.** Потенциальные кривые взаимодействия пузырьков воздуха и частиц талька (1, 2) и пирротина (3) с композициями депрессоров  
1 – ПАЦ-Н + ЖС, 2 – КМК-БУР + ЖС, 3 – ПАЦ-Н + ЖС  
Концентрации ЖС – 100 мг/л, КМК-БУР – 250 мг/л, ПАЦ-Н – 250 мг/л

## Conclusion

The investigation of the flotation of talcose copper-nickel ore, along with the assessment of the hydrophobicity and surface charge of minerals, revealed that the combination of carboxymethylated polysaccharides and sodium silicate hydrophilizes the talc surface more effectively than each of the reagents separately. However, sodium silicate alone hardly depresses the talc surface at all. The depression of flotation-active silicates is effective when polysaccharide and sodium silicate are sequentially supplied. Under these conditions, SS contributes significantly to the increase in the negative charge on the talc particle surfaces. This effect is more pronounced for compositions with starch characterized by a lower degree of substitution compared to cellulose.

The combined use of carboxymethylated polysaccharide and sodium silicate considerably reduces the yield of concentrate due to the depression of flotation-active magnesium-containing silicates, with a slight decrease in the recovery of sulfides. This subsequently creates conditions for enhancing the efficiency of the concentrate's pyrometallurgical processing.

## References

1. Srđyan M. Bulatovic. Handbook of flotation reagents: Chemistry, theory and practice. Vol. 2: Flotation of Gold, PGM and Oxide Minerals. Amsterdam: Elsevier Science, 2010. 230 p.
2. Lavrinenko A.A., Kuznetsova I.N., Lusinyan O.G., Golberg G.Yu. Utilizing Russian polymer anion active depressants in the flotation of out-of-balance talcose copper nickel ore. *Izvestiya. Non-Ferrous Metallurgy*. 2023;29(5):5–14.  
<https://doi.org/10.17073/0021-3438-2023-5-5-14>  
Лавриненко А.А., Кузнецова И.Н., Лусинян О.Г., Гольберг Г.Ю. Применение отечественных полимерных анионоактивных депрессоров при флотации забалансовой оталькованной медно-никелевой руды. *Известия вузов. Цветная металлургия*. 2023;29(5):5–14.  
<https://doi.org/10.17073/0021-3438-2023-5-5-14>
3. Feng B., Lu Y.P., Feng Q.M., Zhang M.Y., Gu Y.L. Talc-serpentine interactions and implications for talc depression. *Minerals Engineering*. 2012a;32:68–73.  
<https://doi.org/10.1016/j.mineng.2012.03.004>
4. Cawood S.R., Harris P.J., Bradshaw D.J. A simple method for establishing whether the adsorption of polysaccharides on talc is a reversible process. *Minerals Engineering*. 2005;18:1060–1063.  
<https://doi.org/10.1016/j.mineng.2005.01.012>

5. Wiese J., Harris P., Bradshaw D. The response of sulphide and gangue minerals in selected Merensky ores to increased depressant dosages. *Minerals Engineering*. 2007;20:986–995.  
<https://doi.org/10.1016/j.mineng.2007.03.008>
6. Morris G.E., Fornasiero D., Ralston J. Polymer depressants at the talc-water interface: adsorption isotherm, microflotation and electrokinetic studies. *International Journal of Mineral Processing*. 2002;67:211–227.  
[https://doi.org/10.1016/S0301-7516\(02\)00048-0](https://doi.org/10.1016/S0301-7516(02)00048-0)
7. Beattie David A., Huynh Le, Kaggwa Gillian B.N., Ralston J. The effect of polysaccharides and polyacrylamides on the depression of talc and the flotation of sulphide minerals. *Minerals Engineering*. 2006;19(6-8): 598–608.  
<https://doi.org/10.1016/j.mineng.2005.09.011>
8. Afanasova A.V., Aburova V.A., Prokhorova E.O., Lushina E.A. Investigation of the influence of depressors on flotation-active rock-forming minerals in sulphide goldbearing ore flotation. *МІАВ. Горний інформаційно-аналітичний бюллетень*. 2022;(6-2):161–174. (In Russ.).  
Афанасова А.В., Абурова В.А., Прохорова Е.О., Лушина Е.А. Исследование влияния депрессоров на флотоактивные породообразующие минералы при флотации сульфидных золотосодержащих руд. *Горный информационно-аналитический бюллетень*. 2022;(6-2):161–174.  
<https://doi.org/10.25018/0236-1493-2022-62-0-161>
9. Bragin V.I., Burdakova E.A., Usmanova N.F., Kinyakin A.I. Comprehensive assessment of flotation reagents by their influence on metal losses and flotation selectivity. *Izvestiya. Non-Ferrous Metallurgy*. 2021;27(5): 4–12. (In Russ.).  
<https://doi.org/10.17073/0021-3438-2021-5-4-12>  
Брагин В.И., Бурдакова Е.А., Усманова Н.Ф., Кинякин А.И. Комплексная оценка флотационных реагентов по их влиянию на потери металлов и селективность флотации. *Известия вузов. Цветная металлургия*. 2021;27(5):4–12.  
<https://doi.org/10.17073/0021-3438-2021-5-4-12>
10. Lygach A.V., Ignatkina V.A. Study of the flotation properties of the main minerals contained in nodular phosphorites of the Yegoryevskoe deposit. *Gornyi informatsionno-analiticheskii byulleten'*. 2018;8: 163–175.  
<https://doi.org/10.25018/0236-1493-2018-8-0-163-175>  
Лыгач А.В., Игнаткина В.А. Изучение флотационных свойств основных минералов, содержащихся в желваковых фосфоритах Егорьевского месторождения. *Горный информационно-аналитический бюллетень*. 2018;8:163–175.  
<https://doi.org/10.25018/0236-1493-2018-8-0-163-175>
11. Tao Long, Huahua Zhao, Yaping Wang, Wei Yang, Sha Deng, Wei Xiao, Xuechen Lan, Qian Wang. Synergistic mechanism of acidified water glass and carboxymethyl cellulose in flotation of nickel sulfide ore. *Minerals Engineering*. 2022;181:107547.  
<https://doi.org/10.1016/j.mineng.2022.107547>
12. Glembofsky V.A., Klassen V.I. Flotation methods of enrichment. Textbook for universities. 2nd ed. Moscow: Nedra, 1981. 304 p. (In Russ.).  
Глембоцкий В.А., Классен В.И. Флотационные методы обогащения. Учебник для вузов: 2-е изд., перераб. и доп. М.: Недра, 1981. 304 с.
13. Ji-Wei Xue, Hua-Zhen Tu, Jin Shi, Yan-Ni An, He Wan, Xian-Zhong Bu. Enhanced inhibition of talc flotation using acidified sodium silicate and sodium carboxymethyl cellulose as the combined inhibitor. *International Journal of Minerals, Metallurgy and Materials*. 2023;30(7): 1310–1319.  
<https://doi.org/10.1007/s12613-022-2582-5>
14. Kupka N., Möckel R., Rudolph M. Acidified water glass in the selective flotation of scheelite from calcite, Part I: performance and impact of the acid type. *Physicochemical Problems of Mineral Processing*. 2020;56(2):238–251.  
<https://doi.org/10.37190/ppmp19101>
15. Molifie A., Becker M., Geldenhuys S., McFadzean B. Investigating the reasons for the improvement in flotation grade and recovery of an altered PGE ore when using sodium silicate. *Minerals Engineering*. 2023;195:108024.  
<https://doi.org/10.1016/j.mineng.2023.108024>
16. Feng Bo, Luo Xianping, Wang Jinqing, Wang Pengcheng. The flotation separation of scheelite from calcite using acidified sodiumsilicate as depressant. *Minerals Engineering*. 2015;80:45–49.  
<http://dx.doi.org/10.1016/j.mineng.2015.06.017>
17. Silva J.P.P., Baltar C.A.M., Gonzaga R.S.G., Peres A.E.C., Leite J.Y.P. Identification of sodium silicate species used as flotation depressants. *Minerals & Metallurgical Processing*. 2012;29(4):207–210.  
<https://doi.org/10.1007/bf03402458>
18. Weiqing Wang, Hongbin Wang, Qiang Wua, Yu Zhenga, Yating Cui, Wu Yanc, Jie Deng, Tiefeng Peng. Comparative study on adsorption and depressant effects of carboxymethyl cellulose and sodium silicate in flotation. *Journal of Molecular Liquids*. 2018;268:140–148.  
<https://doi.org/10.1016/j.molliq.2018.07.048>
19. Bo Feng, Yi-Ping Lu, Qi-Ming Feng, Peng Ding, Na Luo. Mechanisms of surface charge development of serpentine mineral. *Transactions of Nonferrous Metals Society of China*. 2013;23(4):1123–1128.  
[https://doi.org/10.1016/S1003-6326\(13\)62574-1](https://doi.org/10.1016/S1003-6326(13)62574-1)
20. Weiqing Wang, Hongbin Wang, Qiang Wua, Yu Zheng, Yating Cui, Wu Yan, Jie Deng, Tiefeng Peng. Compar-

- tive study on adsorption and depressant effects of carboxymethyl cellulose and sodium silicate in flotation. *Journal of Molecular Liquids*. 2018;268:140–148.  
<https://doi.org/10.1016/j.molliq.2018.07.048>
21. Bazaar J.A., Rahimi M., Fathinia S., Jafari M., Chipakwe V., Chelgani S.C. Talc flotation — an overview. *Minerals*. 2021;11(662):19.  
<https://doi.org/10.3390/min11070662>
  22. Chanturia V.A., Nedosekina T.V., Fedorov A.A. Some features of the interaction of sulfhydryl collectors of the xanthate and dithiocarbamate class with pyrite and arsenopyrite. *Tsvetnye metally*. 2000;(5):12–15. (In Russ.). Чантурия В.А., Недосекина Т.В., Федоров А.А. Некоторые особенности взаимодействия сульфгидрильных собирателей класса ксантогенатов и дитиокарбаматов с пиритом и арсенопиритом. *Цветные металлы*. 2000;(5):12–15.
  23. Lavrinenko A.A., Golberg G.Yu., Shrader E.A., Sarkisova L.M., Kuznetsova I.N. Talcum particle-air bubble attachment in the presence of carboxymethyl cellulose depressant. *MIAB. Gornyi informatsionno-analiticheskii byulleten'*. 2021;(11):68–79. (In Russ).  
<https://doi.org/10.25018/0236-1493-2021-11-0-68>  
Лавриненко А.А., Гольберг Г.Ю., Шрадер Э.А., Саркисова Л.М., Кузнецова И.Н. Поверхностные взаимодействия частиц талька с пузырьками воздуха в присутствии депрессора карбоксиметилцеллюлозы. *Горный информационно-аналитический бюллетень*. 2021;(11):68–79.  
<https://doi.org/10.25018/0236-1493-2021-11-0-68>
  24. Aimara P., Vacchin P. Slow colloidal aggregation and membrane fouling. *Journal of Membrane Science*. 2010; 360(1-2):70–76.  
<https://doi.org/10.1016/j.memsci.2010.05.001>

## Information about the authors

**Anatoliy A. Lavrinenko** — Dr. Sci. (Eng.), Chief Researcher, Head of Laboratory, Institute of Comprehensive Exploitation of Mineral Resources n.a. Academician N.V. Melnikov of the Russian Academy of Sciences (ICEMR RAS).

<https://orcid.org/0000-0002-7955-5273>

E-mail: lavrin\_a@mail.ru

**Irina N. Kuznetsova** — Cand. Sci. (Eng.), Senior Researcher, ICEMR RAS.

<https://orcid.org/0000-0002-5980-8472>

E-mail: iren-kuznetsova@mail.ru

**Grigoriy Yu. Golberg** — Dr. Sc. (Eng.), Leading Researcher, ICEMR RAS.

<https://orcid.org/0000-0002-7968-3144>

E-mail: gr\_yu\_g@mail.ru

**Oganes G. Lusinyan** — Cand. Sci. (Eng.), Leading Engineer, ICEMR RAS.

<https://orcid.org/0000-0002-5655-1747>

E-mail: lusinyan.oganes@yandex.ru

## Информация об авторах

**Анатолий Афанасьевич Лавриненко** — д.т.н., гл. науч. сотрудник, зав. лабораторией, Институт проблем комплексного освоения недр им. академика Н.В. Мельникова Российской академии наук (ИПКОН РАН).

<https://orcid.org/0000-0002-7955-5273>

E-mail: lavrin\_a@mail.ru

**Ирина Николаевна Кузнецова** — к.т.н., ст. науч. сотрудник, ИПКОН РАН.

<https://orcid.org/0000-0002-5980-8472>

E-mail: iren-kuznetsova@mail.ru

**Григорий Юрьевич Гольберг** — д.т.н., вед. науч. сотрудник, ИПКОН РАН.

<https://orcid.org/0000-0002-7968-3144>

E-mail: gr\_yu\_g@mail.ru

**Оганес Георгиевич Лусинян** — к.т.н., вед. инженер, ИПКОН РАН.

<https://orcid.org/0000-0002-5655-1747>

E-mail: lusinyan.oganes@yandex.ru

## Contribution of the authors

**A.A. Lavrinenko** – formulating the concept of the work, determining the purpose of the work, analyzing the experimental data, writing the article.

**I.N. Kuznetsova** – preparing the samples of ore for investigation, conducting the flotation experiments, measuring the detachment force and zeta potential, processing experimental data, participating in the discussion of the results.

**G.Yu. Golberg** – collecting and analyzing the literature data, analyzing the experimental data, participating in the discussion of the results, making theoretical calculations.

**O.G. Lusinyan** – preparing the samples of ore for investigation, conducting the flotation experiments and calculations, participating in the discussion of the results.

## Вклад авторов

**А.А. Лавриненко** – формулировка концепции работы, определение цели работы, анализ экспериментальных данных, написание текста статьи.

**И.Н. Кузнецова** – подготовка пробы руды для исследований, проведение экспериментов по флотации, измерению силы отрыва и электрокинетического потенциала, обработка экспериментальных данных, участие в обсуждении результатов.

**Г.Ю. Гольберг** – сбор и анализ литературы, анализ экспериментальных данных, участие в обсуждении результатов, проведение теоретических расчетов.

**О.Г. Лусинян** – подготовка пробы руды для исследований, проведение экспериментов по флотации, выполнение расчетов, участие в обсуждении результатов.

---

*The article was submitted 20.03.2024, revised 22.04.2024, accepted for publication 25.04.2024*

*Статья поступила в редакцию 20.03.2024, доработана 22.04.2024, подписана в печать 25.04.2024*

UDC 621.791.755, 621.785.01

<https://doi.org/10.17073/0021-3438-2024-2-16-29>

Research article

Научная статья



# Structure and mechanical properties of Ti<sub>2</sub>AlNb-based alloy welded joints using keyhole plasma arc welding with subsequent heat treatment

S.V. Naumov<sup>1</sup>, D.O. Panov<sup>1</sup>, R.S. Chernichenko<sup>1</sup>, V.S. Sokolovsky<sup>1</sup>, G.A. Salishchev<sup>1</sup>, E.B. Alekseev<sup>2</sup>, S.D. Neulybin<sup>3</sup>, D.S. Belinin<sup>3</sup>, Yu.D. Shchitsyn<sup>3</sup>, V.V. Lukianov<sup>4</sup>

<sup>1</sup> Belgorod National Research University  
85 Pobedy Str., Belgorod 308015, Russia

<sup>2</sup> All-Russian Research Institute of Aviation Materials  
of the National Research Center “Kurchatov Institute”  
17 Radio Str., Moscow 105005, Russia

<sup>3</sup> Perm National Research Polytechnic University  
29 Komsomolskiy Prosp., Perm 614990, Russia

<sup>4</sup> NPA “Technopark AT”  
5 bld. 1 Tramvaynaya Str., Ufa 450027, Russia

✉ Stanislav V. Naumov (NaumovStanislav@yandex.ru)

**Abstract:** Using keyhole plasma arc welding, welded joints of a Ti<sub>2</sub>AlNb-based alloy, VTI-4, were obtained, and their structure and mechanical properties were studied. It has been established that the dynamic effect of a keyhole arc had a positive effect on the quality of the welded joint; namely, lack of penetration, porosity, and microcracks were eliminated. The welded joint consisted of a fusion zone (FZ), a heat-affected zone (HAZ), and a base metal (BM). Depending on the phase composition and morphology of the obtained phases, the HAZ can be divided into four zones: HAZ1 with large  $\beta$ -phase grains near the melting line, HAZ2 with large  $\beta$ -phase grains +  $\alpha_2$ , HAZ3 with more fragmented  $\beta$ -phase grains retaining more  $\alpha_2$ -phase, and HAZ4 with the phase composition  $\beta$  +  $\alpha_2$  + O. Subsequent heat treatment (HT: quenching at 920 °C for 2 h, cooling in air, followed by aging at 800 °C for 6 h, cooling in air) preserved the zone structure of the weld but led to the formation of the O-phase within  $\beta$ -grains. The microhardness of the weld in the zone corresponds to  $360 \pm 15$  HV<sub>0.2</sub>, but after HT, it increased to  $382 \pm 20$  HV<sub>0.2</sub>. The strength properties of the welded joint after HT were above 90 % of the base metal ( $\sigma_{ucs} = 1120$  MPa,  $\sigma_{0.2} = 1090$  MPa), while elongation to failure is close to the initial condition ( $\delta = 2.1$  %).

**Keywords:** VTI-4 alloy based on orthorhombic titanium aluminide, Ti<sub>2</sub>AlNb, keyhole plasma arc welding, weld seam, BSE analysis, EBSD analysis, mechanical properties, microhardness.

**Acknowledgments:** This work was supported by the Russian Science Foundation (Agreement No. 19-79-30066) using the equipment of BSU Shared Research Facilities “Technologies and Materials”.

**For citation:** Naumov S.V., Panov D.O., Chernichenko R.S., Sokolovsky V.S., Salishchev G.A., Alekseev E.B., Neulybin S.D., Belinin D.S., Shchitsyn Yu.D., Lukianov V.V. Structure and mechanical properties of Ti<sub>2</sub>AlNb-based alloy welded joints using keyhole plasma arc welding with subsequent heat treatment. *Izvestiya. Non-Ferrous Metallurgy*. 2024;30(2):16–29.

<https://doi.org/10.17073/0021-3438-2024-2-16-29>

# Структура и механические свойства сварных соединений из сплава на основе орторомбического алюминид титана, полученных плазменной сваркой проникающей дугой с последующей термической обработкой

С.В. Наумов<sup>1</sup>, Д.О. Панов<sup>1</sup>, Р.С. Черниченко<sup>1</sup>, В.С. Соколовский<sup>1</sup>,  
Г.А. Салищев<sup>1</sup>, Е.Б. Алексеев<sup>2</sup>, С.Д. Неулыбин<sup>3</sup>, Д.С. Белинин<sup>3</sup>,  
Ю.Д. Щицын<sup>3</sup>, В.В. Лукьянов<sup>4</sup>

<sup>1</sup> Белгородский государственный национальный исследовательский университет  
Россия, 308015, г. Белгород, ул. Победы, 85

<sup>2</sup> Всероссийский научно-исследовательский институт авиационных материалов  
Национального исследовательского центра «Курчатовский институт»  
Россия, 105005, г. Москва, ул. Радио, 17

<sup>3</sup> Пермский национальный исследовательский политехнический университет  
Россия, 614990, г. Пермь, Комсомольский пр-т, 29

<sup>4</sup> НПА «Технопарк АТ»  
Россия, 450027, г. Уфа, ул. Трамвайная, 5, корп. 1

✉ Станислав Валентинович Наумов (NaumovStanislav@yandex.ru)

**Аннотация:** Методом плазменной сварки проникающей дугой заготовок из сплава ВТИ-4 на основе орторомбического алюминид титана  $Ti_2AlNb$  получены сварные соединения и исследованы их структура и механические свойства. Установлено, что динамическое воздействие проникающей дуги оказывает положительное влияние на качество сварного соединения: исключаются непровар, возникновение пористости и микротрещин, а также формируется благоприятная форма корня шва. Обнаружено, что сварное соединение состоит из зоны плавления (ЗП), зоны термического влияния (ЗТВ) и основного металла (ОМ). В зависимости от фазового состава и морфологии фаз ЗТВ можно разделить на 4 области: ЗТВ1 из крупных зерен  $\beta$ -фазы вблизи линии сплавления, ЗТВ2 из крупных зерен  $\beta$ -фазы +  $\alpha_2$ , ЗТВ3 с более фрагментированными зернами  $\beta$ -фазы с сохранением большего количества  $\alpha_2$ -фазы и ЗТВ4, имеющей фазовый состав  $\beta + \alpha_2 + O$ . Последующая термическая обработка (ТО: закалка при температуре 920 °С с выдержкой 2 ч и охлаждением на воздухе с последующей выдержкой 6 ч при 800 °С и дальнейшим охлаждением на воздухе) обеспечивает сохранение зонной структуры сварного шва, но приводит к формированию во всех зонах внутри  $\beta$ -зерен частиц О-фазы. Микротвердость сварного шва в зоне плавления соответствует  $360 \pm 15 HV_{0,2}$ , а после ТО она возрастает до  $382 \pm 20 HV_{0,2}$ . Прочностные свойства сварного соединения после ТО находятся на уровне выше 90 % от показателей исходной ковальной заготовки ( $\sigma_B = 1120$  МПа,  $\sigma_{0,2} = 1090$  МПа), а пластичность близка к исходному состоянию ( $\delta = 2,1$  %).

**Ключевые слова:** сплав ВТИ-4 на основе орторомбического алюминид титана,  $Ti_2AlNb$ , плазменная сварка проникающей дугой, сварной шов, BSE-анализ, EBSD-анализ, механические свойства, микротвердость.

**Благодарности:** Работа выполнена при финансовой поддержке РФФИ (Соглашение № 19-79-30066) с использованием оборудования Центра коллективного пользования «Технологии и Материалы НИУ «БелГУ».

**Для цитирования:** Наумов С.В., Панов Д.О., Черниченко Р.С., Соколовский В.С., Салищев Г.А., Алексеев Е.Б., Неулыбин С.Д., Белинин Д.С., Щицын Ю.Д., Лукьянов В.В. Структура и механические свойства сварных соединений из сплава на основе орторомбического алюминид титана, полученных плазменной сваркой проникающей дугой с последующей термической обработкой. *Известия вузов. Цветная металлургия*. 2024;30(2):16–29.

<https://doi.org/10.17073/0021-3438-2024-2-16-29>

## Introduction

Titanium alloys based on orthorhombic titanium aluminide (Ti<sub>2</sub>AlNb alloys) are considered as a potential replacement for Ni-based superalloys in the aerospace industry [1]. The interest in these materials is due to their high creep resistance and burn resistance compared to conventional titanium alloys, allowing their use at temperatures up to 650 °C [2]. Additionally, they have higher ductility and crack resistance compared to  $\gamma$ -TiAl- and  $\alpha_2$ -Ti<sub>3</sub>Al-based alloys and lower density ( $\rho = 5\div 6 \text{ gm/cm}^3$ ) compared to Ni-based superalloys [3–6].

One of the main obstacles to the widespread use of Ti<sub>2</sub>AlNb alloys is the difficulty in obtaining high-quality weld joints due to low thermal conductivity, high residual stresses, and a cascade of phase transformations during cooling. These characteristics require the selection of welding parameters to achieve the optimal structure of the weld joint for the desired mechanical properties. Technologies for creating non-dismountable joints have been proposed to manufacture high-quality structures, expanding the application range of Ti<sub>2</sub>AlNb alloys [7]: tungsten inert gas welding (TIG) [8; 9], diffusion bonding [10; 11], friction stir welding [12; 13], laser beam welding [14–16], electron beam welding [17–19], etc. Among the welding methods for titanium alloys, TIG welding is the most widely used in the industry [20].

Common problems when using TIG welding with Ti<sub>2</sub>AlNb alloys include low productivity, porosity of the weld joint, and the formation of a coarse dendritic structure of the  $\beta$ -phase in the fusion zone. Additionally, when welding thick (>4 mm) products, it is necessary to use filler material with a corresponding chemical composition, which requires the manufacturing of such consumables [21]. Moreover, multi-pass welding leads to repeated overheating of the weld joint, resulting in significant grain growth and consequently low ductility. On the other hand, keyhole plasma arc welding (K-PAW) can serve as the most technologically advanced alternative among arc welding methods for obtaining non-dismountable joints, allowing for defect-free welds of titanium alloys over a wide range of thicknesses. This method has not been used to obtain non-dismountable joints from Ti<sub>2</sub>AlNb alloys, requiring research on the influence of welding parameters on the quality of the weld joint, its structure, and mechanical properties.

Thus, the aim of this study was to develop K-PAW parameters and determine the influence of the optimal welding regime and subsequent heat treatment on the structure and properties of welded joints made from the

VTi-4 alloy based on orthorhombic titanium aluminide (Ti<sub>2</sub>AlNb).

## Materials and research methods

The study utilized plates made from the VTi-4 alloy, the chemical composition of which is provided below, in at. %:

Ti.....	Base
Al.....	23
Nb.....	23
V.....	1.4
Zr.....	0.8
Mo.....	0.4
Si.....	0.4

The investigated alloy in its initial forged state possesses the following mechanical properties: ultimate tensile strength ( $\sigma_{\text{ucs}} = 1230 \text{ MPa}$ ), yield strength ( $\sigma_{\text{ys}} = 1190 \text{ MPa}$ ), elongation to failure ( $\delta = 3.5 \%$ ), microhardness  $420 \pm 15 \text{ HV}_{0.2}$ .

The microstructure of the initial billet in the form of a hot-rolled plate is shown in Fig. 1. It exhibits large  $\beta$ -grains with a size of  $300 \pm 50 \mu\text{m}$ , with globular  $\alpha_2$ -phase grains of  $10 \pm 5 \mu\text{m}$  located along the grain boundaries. Additionally, uniformly distributed within the volume of the  $\beta$ -grains, there are needle-like  $\omega$ -phase precipitates with a length of  $8 \pm 3 \mu\text{m}$  and a thickness of  $1\text{--}3 \mu\text{m}$ .

K-PAW was performed using the PMI-350 AC/DC TL power source (SBI, Austria) on an automated gantry-type console [22]. Fixing plates were welded to the welding locations to secure the workpieces

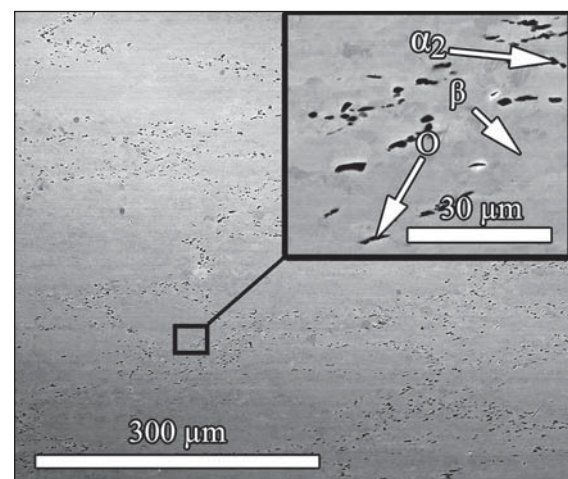


Fig. 1. Microstructure of forged plate of the VTi-4 alloy

Рис. 1. Микроструктура горячекованной плиты из сплава ВТИ-4

in the fixture, allowing for the delivery of shielding gas to the root of the weld joint and ensuring uniform movement of the plasma torch with the shielding block. Samples for K-PAW with dimensions of  $50 \times 25 \times 4$  mm were cut from the forged plate. Prior to welding, the entire surface of the samples was ground with abrasive paper with a grain size of  $68 \mu\text{m}$  FEPA P № 220, and the mating surface at the joint was ground with grinding wheels with a grain size of  $18 \mu\text{m}$  FEPA P № 1000.

Welding of 4 mm thick plates made from the VTi-4 alloy was performed end-to-end without gaps or filler material. The melting current required to form a hole at the root of the weld (keyhole) was set at 150–160 A and applied for 0.5 sec. As a result of the melting, the welding process transitions to the keyhole mode, and part of the arc energy is dissipated. The main welding current in this process is reduced to 140–150 A, the arc voltage is 21–22 V, welding speed is 20 m/h, and the current at the end of welding (at the moment of exiting the fixating plates) drops to 15–20 A. Since non-consumable (copper) fixating plates were used, the welding process was completed at minimal currents. The plasma-forming gas flow rate was 3 L/min, the shielding gas flow rate was 3 L/min, and the additional shielding gas flow rate for the shielding block was 8 L/min. Argon grade 5.0 (99.999 % Ar) was used as the plasma-forming gas.

The interaction of the compressed arc with the weld pool occurs in the formed crater cavity.

The magnitude and nature of the distribution of the compressive arc's force impact in the weld pool largely determine the characteristics of the melting front ablation process, molten metal movement, bath retention, and the quality of weld root formation.

Welded joints underwent heat treatment in a split-type folding tube furnace RS80/300/13 (“Nabertherm”, Germany) according to the quenching + aging: quenching at a temperature of 920 °C for 2 h followed by air cooling and subsequent aging for 6 h at 800 °C with further air cooling. Prior to loading the samples into the furnace, they were subjected to a 3-cycle argon purging and vacuum evacuation. Heating was performed in an argon atmosphere with excess pressure.

Samples for mechanical testing and microstructural analysis were cut using a Sodick VL400Q wire EDM machine (China). The surfaces of the samples were ground using Struers SiC FEPA P № 220-2000 abrasive materials (from 68 to  $10 \mu\text{m}$ ) on Metrotest (Russia), Baipol Metco (India), and LaboPol-5 (“Struers”, Denmark) equipment. Subsequent surface polishing was carried out using Struers MD Chem suspension with OP-S NonDry suspension. Samples for further microstructural analysis were cleaned of organic matter, suspension particles, or abrasive in an ultrasonic bath model 3404 (“Sapphire”, Russia) with acetone for 15 minutes.

The microstructure was examined using a Q600 3D electron microscope (FEI, Czech Republic) equipped with a standard Everhart-Thornley secondary and scattered electron (SEM) and detector of backscat-

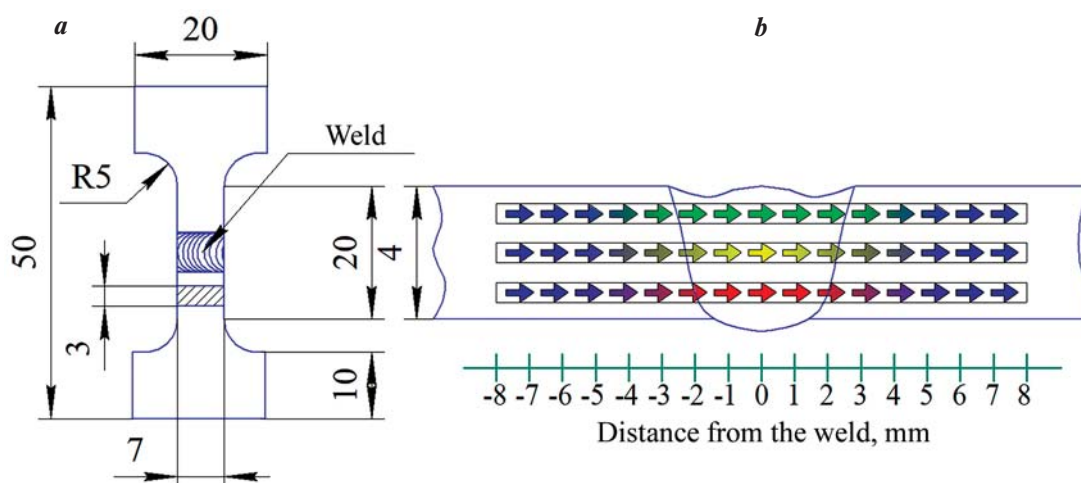


**Fig. 2.** Samples for uniaxial tensile tests: from VTi-4 plates after K-PAW (a); area for measuring microhardness in the cross section of a welded joint of the VTi-4 alloy (b)

The dimensions are specified in millimeters

**Рис. 2.** Образцы для испытаний на одноосное растяжение из пластин ВТИ-4 после плазменной сварки (a) и область измерения микротвердости в поперечном сечении сварного соединения (b)

Размеры указаны в мм

tered electron (BSE) at an accelerating voltage of 20–30 kV. EBSD analysis was performed in backscattered electron diffraction mode with grain orientation mapping. Samples for BSE analysis were fixed on an instrument table with a 45° tilt using carbon conductive adhesive 502 (EMS, USA) or clamps, while NEM TAPE carbon tape (“Nisshin”, Japan) was used for ETD analysis. The sample, additionally tilted at a 25° angle (total angle of 70° to the horizontal), was scanned with a 3 μm step. Data processing and analysis were carried out using OIM Analysis 9 software (EDAX, USA).

Tensile tests on welded joints were conducted using a “5882 testing machine” (Instron, UK) at room temperature with a deformation rate of 10<sup>-4</sup> s<sup>-1</sup>. Control and data collection were performed using “Bluehill 2” software (Instron, UK). The scheme and dimensions of the samples for tensile testing are shown in Fig. 2, *a*. For testing, at least two samples of the base material, welded joints before and after heat treatment, were used.

Microhardness was determined on microgrinds in the cross-section of welded joints using a Vickers 402MVD microhardness tester (Netherlands) with a load of 200 g and an indentation time of 10 sec (HV<sub>0.2</sub>) with a 0.2 mm step. Microhardness in the cross-section of the weld joint was evaluated at 3 points: in the area closer to the weld bead, in the middle of the weld joint, and closer to the weld root (Fig. 2, *b*). Control and data collection were performed using “Hardtest Wolpert Group” software (Netherlands).

## Research results

The results of the study are presented in Table 1, which shows the tested parameters of keyhole plasma arc welding (K-PAW) for 4 mm thick plates made of the VTI-4 alloy. The selection of optimal K-PAW conditions was carried out on a control sample. It was found that at low currents, a melting channel is not formed, leading to disruption of the keyhole plasma arc weld-

ing process. Preliminary investigations showed that a high-quality welded joint was obtained with K-PAW in mode 4 (Table 2): the melting current of the keyhole was set at 160 A, the main welding current was 150 A, and the current at the end of welding was 20 A. In this case, the width of the weld bead is 6.0 mm, and the root of the weld is 3.0 mm. No external defects such as pores and cracks were observed in the resulting welded joints (Fig. 3). Thus, welded joints obtained in mode 4 were used for subsequent research.

Technological plates used for fixture fixation leave traces on the edges of the welded joint (Fig. 3). At the beginning of the weld, there is a zone with a buildup where through melting is formed, and at its end, a zone with edge melting is detected, formed as a result of the displacement of liquid metal to the newly melted weld pool. All detected defects are of a technological nature, which can be eliminated using fixating plates at the beginning and end of welding.

The cross-sectional structure of the welded joint, as determined by BSE-SEM analysis, is shown in Fig. 4. It exhibits an hourglass shape. Interestingly, the boundary of the fusion zone is less curved compared to welded joints after laser and electron beam welding (Fig. 4). This difference can be attributed to the plasma arc passing from top to bottom, resulting in a more evenly distributed heat across the cross-section of the central and root parts of the weld.

In the welded joint, three main zones can be distinguished: the weld zone or fusion zone (FZ), the heat-affected zone (HAZ), and the base metal (BM) (see Fig. 4–6). The fusion zone consists of large columnar β-phase dendrites oriented perpendicular to the fusion line (FL), with an average length of approximately ~750 μm (Fig. 6, *a*). According to EBSD analysis, large equiaxed crystals with a diameter of 350±50 μm were found in the middle of the weld, attributed to the larger volume of the liquid pool and reduced heat dissipation rate from the central part of the weld [23]. Due to the increased cooling rate, no formation of

Table 1. The modes of keyhole plasma arc welding of the VTI-4 alloy plates with a thickness of 4 mm

Таблица 1. Режимы плазменной сварки проникающей дугой пластин из сплава ВТИ-4 толщиной 4 мм

Mode number	Melting point of the lock bore, A	Main welding current, A	Current at the end of welding, A	Consumption of plasma-forming/protective gases, L/min
1	150	140	15	3/3
2	160	140	15	3/3
3	150	150	20	3/3
4	160	150	20	3/3

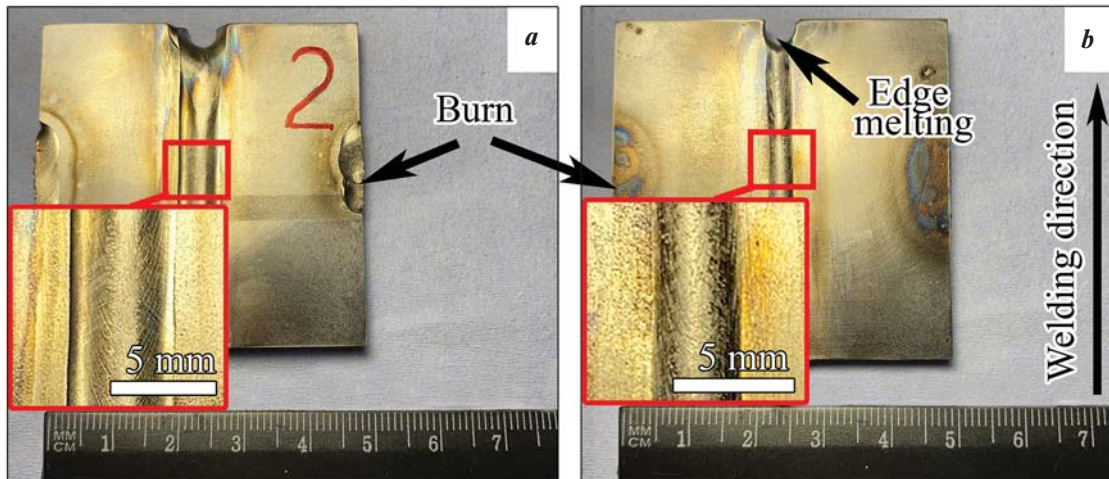


Fig. 3. Appearance of a welded joint of the VTI-4 alloy produced by K-PAW according to mode 4

*a* – weld bead; *b* – root of the weld

Рис. 3. Внешний вид сварного соединения из сплава ВТИ-4, полученного плазменной сваркой проникающей дугой по режиму 4

*a* – валик сварного шва; *b* – корень сварного шва

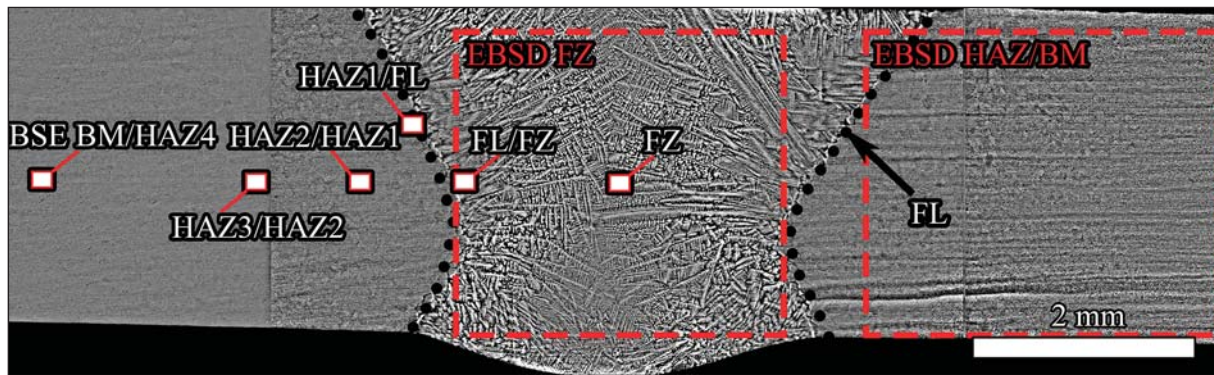


Fig. 4. Cross-section of a weld of the VTI-4 alloy produced by K-PAW with marking of areas for BSE and EBSD microstructural analysis, which are presented in Fig. 5 and 6, respectively

Рис. 4. Поперечное сечение сварного шва сплава ВТИ-4, полученного плазменной сваркой проникающей дугой, с разметкой областей съемки BSE- и EBSD-анализов (см. рис. 5 и 6)

Table 2. Phase composition of the zones of the welded joint of the VTI-4 alloy obtained by K-PAW with subsequent heat treatment

Таблица 2. Фазовый состав зон сварного соединения из сплава ВТИ-4, полученного плазменной сваркой проникающей дугой с последующей термической обработкой

Phases	Contentment, %					
	FZ	HAZ1	HAZ2	HAZ3	HAZ4	BM
$\alpha_2$	–	<1	6.5	7.8	9.0	10.3
O	46.0	43.0	44.0	44.0	45.0	46.0
$\beta$	54.0	57.0	49.5	48.2	46.0	43.7

O- or  $\alpha_2$ -phases occurs in the FZ [24]. Additionally, the high Nb content also contributes to the stabilization of the  $\beta$ -phase [25]. Internal pores were not detected in both the FZ and at the fusion line boundary (Fig. 5, *a, b*). In the near-fusion zone, large globular  $\beta$ -grains with an average size of  $\approx 160 \pm 100 \mu\text{m}$  are formed along the fusion line. In the HAZ at a distance of  $3.5 \pm 0.5 \text{ mm}$  from the center of the weld, smaller equiaxed grains with an average size of  $\approx 100 \pm 40 \mu\text{m}$  are observed (zone HAZ3, Fig. 6, *b*).

The structure of the HAZ after K-PAW can be divided into 4 zones depending on the phase composition and morphology. In the HAZ1 zone, close to the fusion line, large  $\beta$ -phase grains with diameters of 60–260  $\mu\text{m}$  are observed (Fig. 5, *c*). Here,  $\alpha_2$ - and

O-phases completely dissolved during the heating process of welding, and no reverse transformation occurred during cooling. In the HAZ2 and HAZ3 zones, the globular  $\alpha_2$ -phase is partially preserved, as higher

temperatures are required to complete the  $\alpha_2 \rightarrow \beta$  transformation [25]. At the same time, large  $\beta$ -phase grains have sizes ranging from 40–160  $\mu\text{m}$  (Fig. 5, d, e). HAZ4 consists of  $\beta$ -, O-, and  $\alpha_2$ -phases (Fig. 5, f).

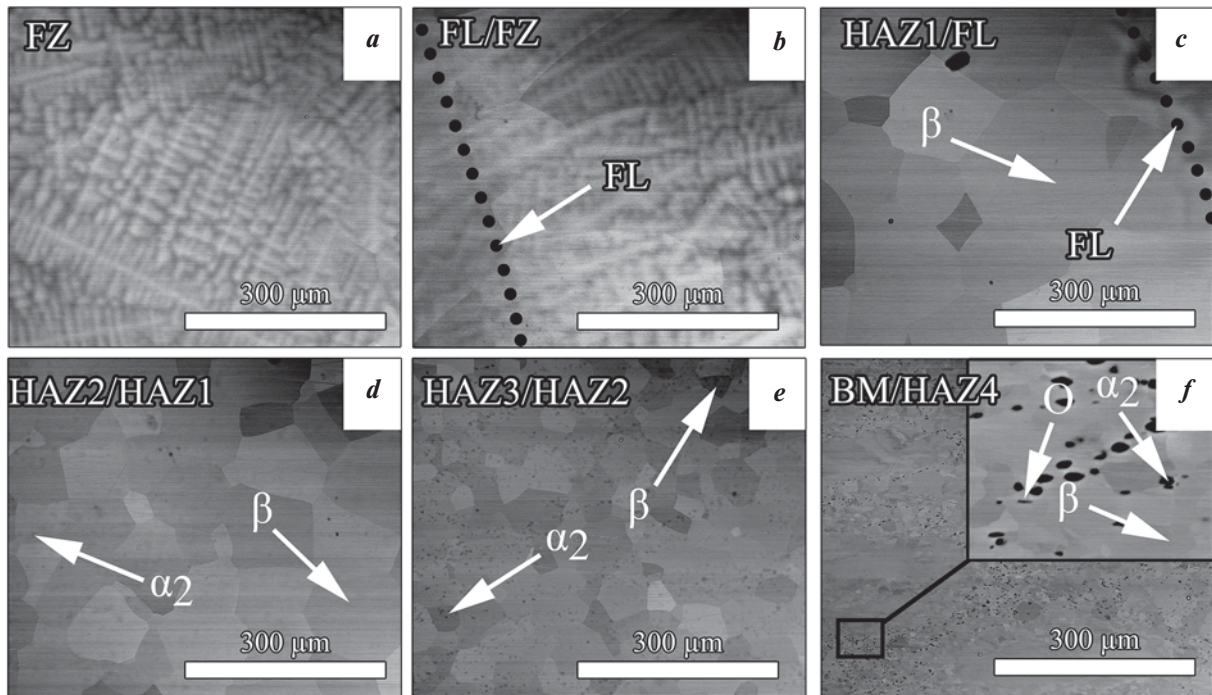


**Fig. 5.** BSE analysis of the microstructure in the cross section of the welded joint of the VTI-4 alloy produced by K-PAW

*a* – fusion zone (FZ); *b* – fusion line (FL); *c* – HAZ1; *d* – HAZ2; *e* – HAZ3; *f* – HAZ4 and base material (BM)

**Рис. 5.** Результаты BSE-анализа микроструктуры в поперечном сечении сварного соединения из сплава ВТИ-4, полученного плазменной сваркой проникающей дугой

*a* – зона плавления (ЗП); *b* – линия сплавления (ЛС); *c* – ЗТВ1; *d* – ЗТВ2; *e* – ЗТВ3; *f* – ЗТВ4 и основной материал (ОМ)

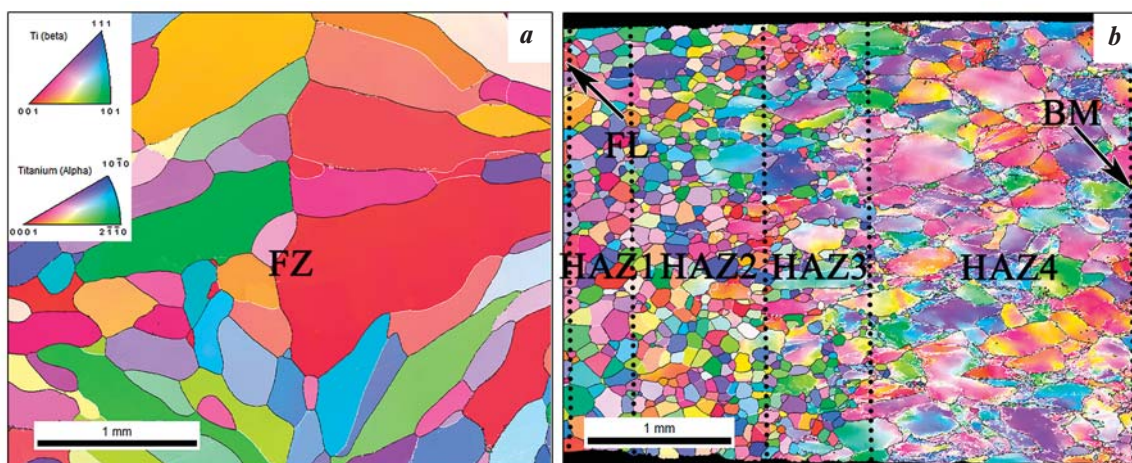


**Fig. 6.** EBSD analysis of a welded joint of VTI-4 alloy in the cross section of the weld obtained by K-PAW

*a* – center of the weld; *b* – from the fusion zone to the base metal

**Рис. 6.** EBSD-карты сварного соединения из сплава ВТИ-4 в поперечном сечении сварного шва, полученного плазменной сваркой проникающей дугой

*a* – центр сварного шва; *b* – участок от зоны плавления до основного металла

Unlike the BM, in HAZ4, during heating, the O-phase partially transforms into the  $\beta$ -phase, while the  $\alpha_2$ -phase mainly remains.

The transition from HAZ2 to HAZ3 and HAZ4 is gradual and accompanied by the appearance of the  $\alpha_2$ -phase and an increase in its proportion in the structure. During the transition from HAZ4 to BM, an increase in the O-phase content is observed. Zones of thermal influence with phase composition, morphology, and size similar to those described above were also observed in previous studies [25–27].

During the heat treatment process, within the fusion zone (FZ), needle-like O-phase particles with lengths ranging from 1.1–2.9  $\mu\text{m}$  and thicknesses of  $0.21 \pm 0.15 \mu\text{m}$  were precipitated (Fig. 7, a). In the HAZ1, precipitations of  $\alpha_2$ -phase with sizes of  $0.6 \pm 0.2 \mu\text{m}$  formed along the boundaries of large  $\beta$ -grains, with an overall volume fraction not exceeding 1%. Inside the  $\beta$ -grains, particles of the O-phase with lengths ranging from 0.8–2.1  $\mu\text{m}$  were observed (Fig. 7, b). In the HAZ2, needle-like O-phase and  $\alpha_2$ -phase precipitations were observed inside and along the boundaries of  $\beta$ -grains, respectively. Additionally, globular  $\alpha_2$ -phase

particles were found inside the  $\beta$ -grains (Fig. 7, c, d). In the HAZ4, particles of  $\alpha_2$ -phase close to equiaxed shape with diameters of 0.7–3.5  $\mu\text{m}$ , located along the boundaries of  $\beta$ -grains, and needle-like particles of the O-phase with lengths of 1.1–2.4  $\mu\text{m}$  inside the  $\beta$ -grains were also observed (Fig. 7, e). In the base metal (BM) zone, a large number of globular  $\alpha_2$ -phase particles with sizes ranging from 1.2–4.5  $\mu\text{m}$  were present, predominantly along the boundaries of primary  $\beta$ -grains (Fig. 7, f). The BM zone differs from HAZ4 in its lower content of  $\beta$ -phase and higher content of O- and  $\alpha_2$ -phases: 43.7 %, 46.0 %, and 10.3 %, respectively, compared to 46.0 %, 45.0 %, and 9.0 % in HAZ4.

The distribution of microhardness across the transverse section of the weld is shown in Fig. 8. The width of the fusion zone (FZ) ranges from 3 to 6 mm and is within the range of –3 to 3 mm on the graphs, with a microhardness of  $360 \pm 15 \text{HV}_{0.2}$ . The heat-affected zone (HAZ) extends several millimeters on both sides, and the microhardness approaches the values of the base metal (BM) ( $420 \pm 15 \text{HV}_{0.2}$ ). Thus, the width of the HAZ is 4–5 mm.

It is noteworthy that the microhardness profile at dif-

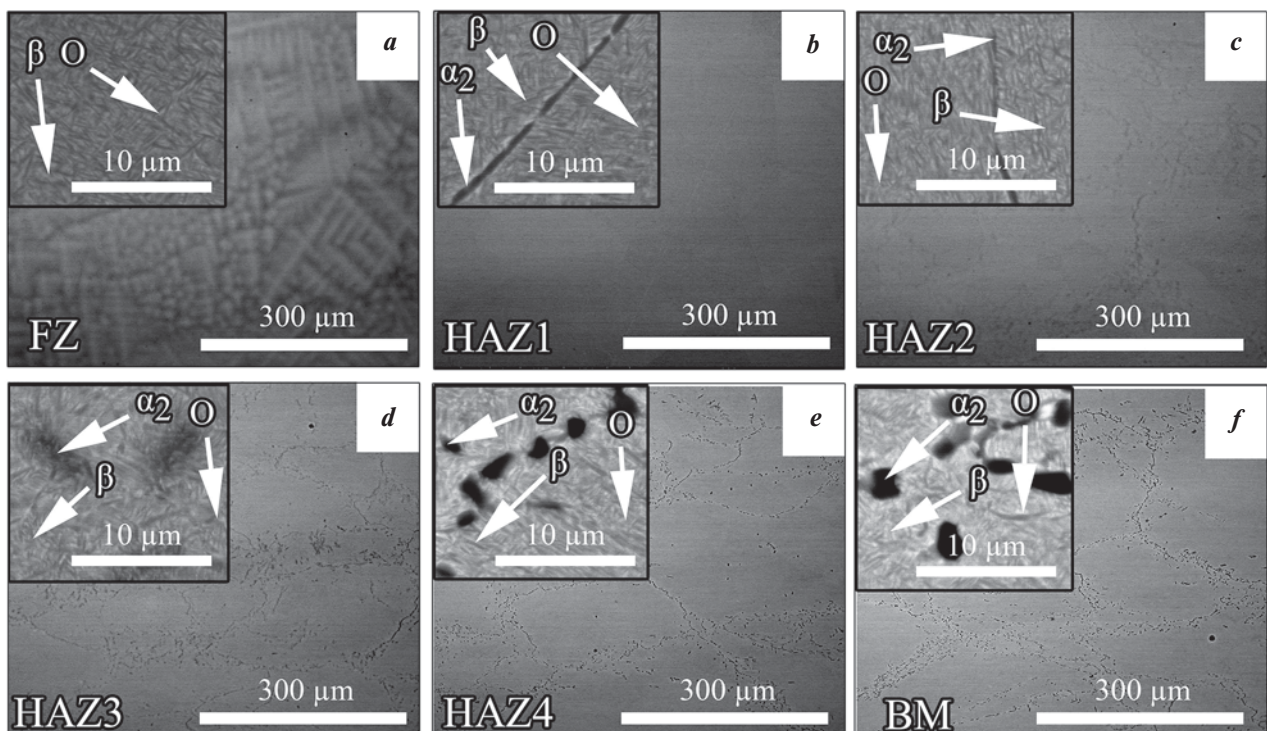


**Fig. 7.** The results of the BSE analysis of the microstructure in the cross-section of the welded joint of the VTI-4 alloy, obtained by K-PAW followed by heat treatment

*a* – fusion zone (FZ); *b* – HAZ1; *c* – HAZ2; *d* – HAZ3; *e* – HAZ4; *f* – base metal (BM)

**Рис. 7.** Результаты BSE-анализа микроструктуры в поперечном сечении сварного соединения из сплава ВТИ-4, полученного плазменной сваркой проникающей дугой с последующей термической обработкой

*a* – зона плавления (ЗП); *b* – ЗТВ1; *c* – ЗТВ2; *d* – ЗТВ3; *e* – ЗТВ4; *f* – основной металл (ОМ)

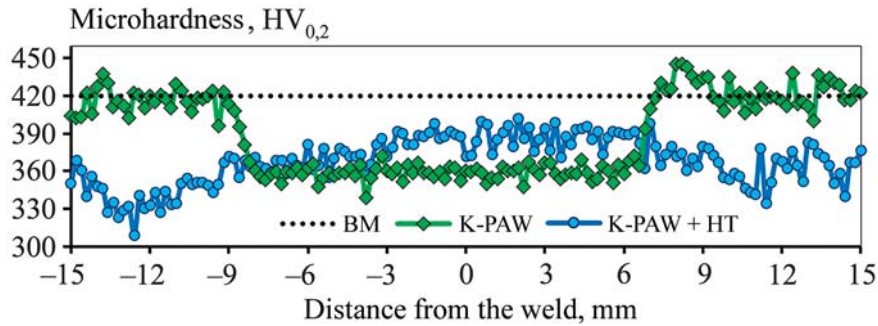


**Fig. 8.** Microhardness of the initial plate ( $HV_{0.2}$  BM) and welded joints of the VTI-4 alloy in the cross section of the weld obtained by K-PAW ( $HV_{0.2}$  K-PAW) with subsequent heat treatment ( $HV_{0.2}$  K-PAW + HT) [K-PAW – keyhole plasma arc welding, HT – heat treatment]

**Рис. 8.** Усредненные значения микротвердости исходной заготовки (ОМ) и сварных соединений из сплава ВТИ-4 в поперечном сечении сварного шва, полученных плазменной сваркой проникающей дугой (ПС) с последующей термической обработкой (ПС + ТО)

ferent levels of the weld remains nearly the same. It is known [28] that for Ti<sub>2</sub>AlNb alloys, dispersion strengthening of the O-phase is the main strengthening mechanism. Therefore, due to the absence of the O-phase, the microhardness is lowest in the FZ and HAZ1 immediately after welding. However, as the transition from the FZ to the BM occurs, it increases [29].

After heat treatment (quenching + aging), the microhardness level slightly increases in the FZ and HAZ1 to  $382 \pm 20 HV_{0.2}$  (Fig. 8). At the same time, a decrease in microhardness to 310–380  $HV_{0.2}$  is observed in HAZ3 and the BM. The hardness profile is closely related to the structural state in each zone. The increase in microhardness in the FZ is primarily associated with the precipitation of fine O-phase during heat treatment [24; 28]. However, a noticeable decrease in microhardness was observed in the BM and HAZ4, which can be explained by the softening effect of static recovery and recrystallization [30].

The tensile test diagrams of samples cut from the original forged blank, as well as the welded joint before and after heat treatment (HT), are presented in Fig. 9. The mechanical properties of the welded joint without HT are at a level higher than 80 % of the parameters of the original blank ( $\sigma_{ucs} = 1020$  MPa,  $\sigma_{ys} = 1010$  MPa); however, elongation to failure of the weld is substantially lower (0.5 %), which may be attributed to the formation of large dendrites of the  $\beta$ -phase in the fusion zone (FZ) [31]. The mechanical properties of the welded joint after HT reach a level exceeding 90 % of the initial state ( $\sigma_{ucs} = 1120$  MPa,  $\sigma_{ys} = 1090$  MPa). Thus, heat treatment contributes to an increase in mechanical properties by approximately 10 % compared to welded joints obtained under plasma welding conditions without subsequent heat treat-

ment. At the same time, elongation to failure of the welded joint reached 2.1 %.

Fracture of the base metal after tensile testing mostly exhibits a ductile relief; however, zones of ductile failure with the formation of dimples and quasi-brittle cleavage facets are identified, explaining the higher ductility of the material (Fig. 10, c, d). In the welded joint, failure occurs through the FZ, and a ductile relief is observed on the fracture surface (Fig. 10, a, b). Microcracks and pores, which could have opened up or become place of failure, were not detected.

The observed fracture is characteristic of welds with a  $\beta$ -phase structure [24; 25], where fracture involves the splitting of the crack at the base of the ductile pattern. In this case, transgranular brittle fracture explains the low ductility of the material [31]. Welded joints after HT fail through a mixed mechanism of inter- and transgranular fracture (Fig. 10, e–h).

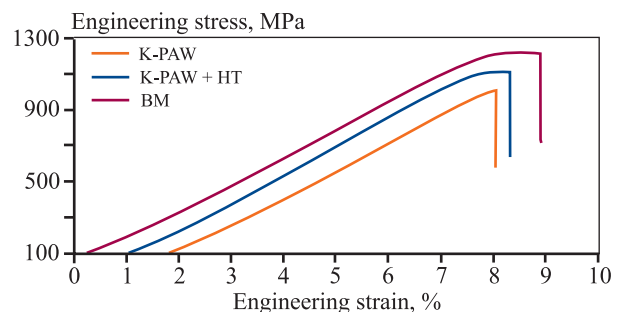


**Fig. 9.** Tensile diagram of the base metal (BM), welded joint (K-PAW) of the VTI-4 alloy with subsequent heat treatment (K-PAW + HT) obtained by K-PAW

**Рис. 9.** Диаграммы растяжения основного металла (ОМ), сварного соединения (ПС) из сплава ВТИ-4, полученного плазменной сваркой с последующей термической обработкой (ПС + ТО)

The fracture occurs at the boundary (fusion line) between the weld and the HAZ1. Obviously, the precipitation of the O-phase in the FZ contributed to the strengthening of the weld, and failure occurred at the FZ/HAZ1 interface. Cracks along the boundaries of large  $\beta$ -phase grains are observed on the fracture surface (Fig. 10, *g, h*), as well as facets of transgranular fracture.

Thus, compared to TIG welding of  $Ti_2AlNb$ -based alloys [8; 32], keyhole plasma arc welding maintains

a large dendritic structure in the weld, but due to the increased thickness of the welded metal and welding speed, the productivity of the process for producing non-detachable joints significantly increases. Furthermore, after heat treatment (HT), the mechanical properties of the welded joints reach levels close to those of the base metal (>90 %).

In comparison to laser beam welding of VT1-4 titanium aluminide-based alloys, which are similar in structure and properties to the original blanks [15],

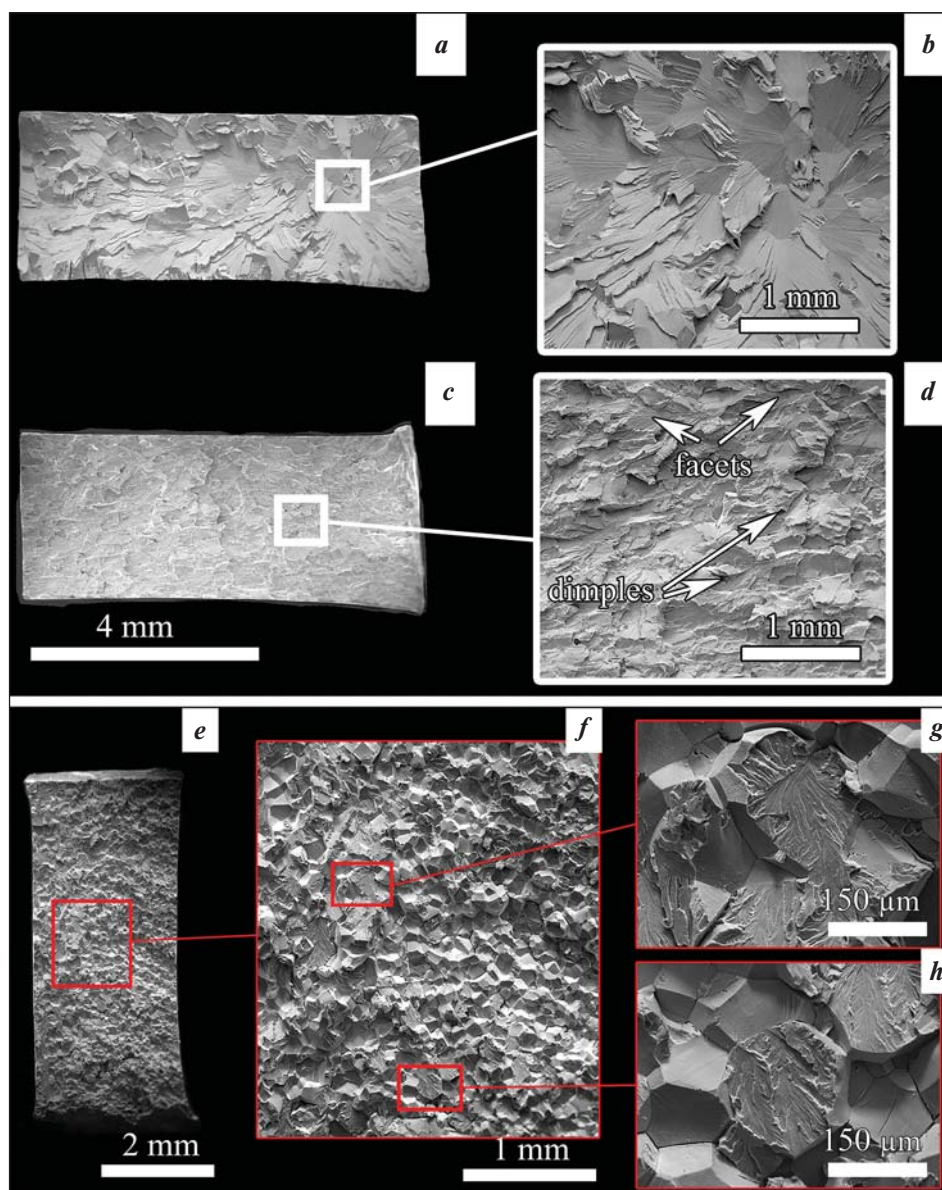


**Fig. 10.** Morphology of fracture surface of samples after tensile tests: *a* – general view of the fracture of the welded joint (WJ); *b* – morphology of the fracture surface of the WJ; *c* – general view of the fracture of the base metal (BM); *d* – morphology of the fracture surface of the BM; *e* – general view of the fracture of the WJ after heat treatment (HT); *f–h* – morphology of the fracture surface of the WJ after HT

**Рис. 10.** Поверхности разрушения образцов после испытаний на растяжение: общий вид и микростроение изломов сварного соединения (*a, b*), основного металла (*c, d*) и сварного соединения после термообработки (*e–h*)

K-PAW ensures the absence of porosity in the weld due to the specific dynamic impact of the plasma arc during welding. Despite the large dendritic structure of the weld after K-PAW (~750 μm), the level of mechanical properties of such dense, defect-free (no porosity) welded joints is close to that of welds obtained by pulsed laser beam welding [15].

## Conclusion

Within the scope of this study, the keyhole plasma arc welding (K-PAW) mode for 4 mm thick plates made of VT1-4 alloy was determined to achieve defect-free welded joints, consisting of the fusion zone, heat-affected zone, and base metal. The HAZ structure after welding, depending on the phase composition and morphology of the phases, can be divided into the following zones: HAZ1 — zone of large β-phase grains near the fusion line; HAZ2 — zone of large β-phase grains with α<sub>2</sub>-phase particles; HAZ3 — zone with more fragmented β-phase grains with a large amount of α<sub>2</sub>-phase preserved; HAZ4 — zone containing β-, α<sub>2</sub>-, and O-phases.

The microhardness of the weld in the FZ corresponds to 360±15 HV<sub>0.2</sub>, and after heat treatment (HT) (quenching at  $t = 920$  °C, holding for 2 h, air cooling, aging at 800 °C,  $\tau = 6$  h, air cooling), it increases to 382±20 HV<sub>0.2</sub> due to strengthening from the precipitation of fine O-phase particles. The mechanical properties of the welded joint after HT are above 90 % of the parameters of the original forged blank ( $\sigma_{ucs} = 1120$  MPa,  $\sigma_{ys} = 1090$  MPa), with elongation to failure approaching the original state ( $\delta = 2.1$  %).

## References

- Goyal K., Bera C., Sardana N. Temperature-dependent structural, mechanical, and thermodynamic properties of B2-phase Ti<sub>2</sub>AlNb for aerospace applications. *Journal of Materials Science*. 2022;57(41):19553–19570. <https://doi.org/10.1007/s10853-022-07788-3>
- Shagiev M.R., Galeev R.M., Valiakhmetov O.R. Ti<sub>2</sub>AlNb-Based intermetallic alloys and composites. *Materials Physics and Mechanics*. 2017;33(1):12–18. [https://doi.org/10.18720/MPM.3312017\\_2](https://doi.org/10.18720/MPM.3312017_2)
- Nandy T.K., Banerjee D. Creep of the orthorhombic phase based on the intermetallic Ti<sub>2</sub>AlNb. *Intermetallics*. 2000;8(8):915–928. [https://doi.org/10.1016/S0966-9795\(00\)00059-5](https://doi.org/10.1016/S0966-9795(00)00059-5)
- Emura S., Araoka A., Hagiwara M. B2 grain size refinement and its effect on room temperature tensile properties of a Ti–22Al–27Nb orthorhombic intermetallic alloy. *Scripta Materialia*. 2003;48:629–634. [https://doi.org/10.1016/S1359-6462\(02\)00462-1](https://doi.org/10.1016/S1359-6462(02)00462-1)
- Kim Y.-W., Dimiduk D.M. Progress in the understanding of gamma titanium aluminides. *Journal of Minerals, Metals & Materials Society*. 1991;43:40–47. <https://doi.org/10.1007/BF03221103>
- Kumpfert J., Leyens C. Orthorhombic titanium aluminides: Intermetallics with improved damage tolerance. In: *Titanium and Titanium Alloys — Fundamentals and Applications*. GmbH & Co.: Wiley–VCH Verlag, 2005. P. 59–88. <https://doi.org/10.1002/3527602119.ch3>
- Li Y.-J., Wu A.-P., Li Q., Zhao Y., Zhu R.-C., Wang G.-Q. Effects of welding parameters on weld shape and residual stresses in electron beam welded Ti<sub>2</sub>AlNb alloy joints. *Transactions of Nonferrous Metals Society of China*. 2019;29(1):67–76. [https://doi.org/10.1016/S1003-6326\(18\)64916-7](https://doi.org/10.1016/S1003-6326(18)64916-7)
- Liu X., Shao L., Ji Y., Zhao H., Wan X. Ultrasonic frequency pulse tungsten inert gas welding of Ti<sub>2</sub>AlNb-based alloy. *Chinese Journal of Rare Metals*. 2014;38(4):541–547. <https://doi.org/10.13373/j.cnki.cjrm.2014.04.001>
- Shao L., Wu S., Datye A., Zhao H., Petterson M., Peng W. Microstructure and mechanical properties of ultrasonic pulse frequency tungsten inert gas welded Ti–22Al–25Nb (at.%) alloy butt joint. *Journal of Materials Processing Technology*. 2018;259:416–423. <https://doi.org/10.1016/j.jmatprotec.2018.03.018>
- Bu Z., Ma X., Li R., Wu J., Li J. Effect of pressure on microstructure and mechanical properties of diffusion bonded joints of Ti<sub>2</sub>AlNb alloy. *Journal of Aeronautical Materials*. 2023;43:51–58. <https://doi.org/10.11868/j.issn.1005-5053.2022.000162>
- Niu T., Jiang B., Zhang N., Wang Y. Microstructure and mechanical properties of Ti–Ti<sub>2</sub>AlNb interface. *Composites and Advanced Materials*. 2021;30:1–7. <https://doi.org/10.1177/2633366X20929>
- Chen X., Zhang Z., Xie F., Wu X., Ma T., Li W., Sun D. Optimizing the integrity of linear friction welded Ti<sub>2</sub>AlNb alloys. *Metals*. 2021;11(5):802. <https://doi.org/10.3390/met11050802>
- Cui D., Wu Q., Jin F., Xu C., Wang M., Wang Z., Li J., He F., Li J., Wang J. Heterogeneous deformation behaviors of an inertia friction welded Ti<sub>2</sub>AlNb joint: an in-situ study. *Acta Metallurgica Sinica*. 2023;36(4):611–622. <https://doi.org/10.1007/s40195-022-01477-5>
- Panov D., Naumov S., Stepanov N., Sokolovsky V., Volokitina E., Kashaev N., Ventzke V., Dinse R., Riekehr S., Povolyaeva E., Nochovnaya N., Alekseev E., Zhreb-tsov S., Salishchev G. Effect of pre-heating and post-weld heat treatment on structure and mechanical properties of

- laser beam-welded Ti<sub>2</sub>AlNb-based joints. *Intermetallics*. 2022;143:107466.  
<https://doi.org/10.1016/j.intermet.2022.107466>
15. Naumov S.V., Panov D.O., Chernichenko R.S., Sokolovsky V.S., Volokitina E.I., Stepanov N.D., Zherebtsov S.V., Alekseev E.B., Nochovnaya N.A., Salishchev G.A. Structure and mechanical properties of welded joints from alloy based on VTI-4 orthorhombic titanium aluminide produced by pulse laser welding. *Izvestiya. Non-Ferrous Metallurgy*. 2023;29(2):57–73.  
<https://doi.org/10.17073/0021-3438-2023-2-57-73>  
Наумов С.В., Панов Д.О., Черниченко Р.С., Соколовский В.С., Волокитина Е.И., Степанов Н.Д., Жеребцов С.В., Алексеев Е.Б., Ночовная Н.А., Салищев Г.А. Структура и механические свойства сварных соединений из сплава на основе орторомбического алюминид титана ВТИ-4, полученных импульсной лазерной сваркой. *Известия вузов. Цветная металлургия*. 2023;29(2):57–73.  
<https://doi.org/10.17073/0021-3438-2023-2-57-73>
  16. Lei Z., Zhang K., Zhou H., Ni L., Chen Y. A comparative study of microstructure and tensile properties of Ti<sub>2</sub>AlNb joints prepared by laser welding and laser-additive welding with the addition of filler powder. *Journal of Materials Processing Technology*. 2018;255:477–487.  
<https://doi.org/10.1016/j.jmatprotec.2017.12.044>
  17. Bu Z., Wu J., Ma X., Li Z., Li J. Microstructure and mechanical properties of electron beam welded joints of Ti<sub>2</sub>AlNb alloy. *Journal of Materials Engineering and Performance*. 2022;20:5329–5337.  
<https://doi.org/10.1007/s11665-022-07514-9>
  18. Li L., Fu P., Zhao T., Tang Z., Mao Z. Effect of preheating on the microstructure evolution and mechanical properties of electron beam welded Ti<sub>2</sub>AlNb alloy. *Journal of Materials Engineering and Performance*. 2022;32(8):3648–3657. <https://doi.org/10.1007/s11665-022-07346-7>
  19. Li Y., Zhao Y., Li Q., Wu A., Zhu R., Wang G. Effects of welding condition on weld shape and distortion in electron beam welded Ti<sub>2</sub>AlNb alloy joints. *Materials & Design*. 2017;114:226–233.  
<https://doi.org/10.1016/j.matdes.2016.11.083>
  20. Short A.B. Gas tungsten arc welding of  $\alpha + \beta$  titanium alloys: A review. *Materials Science and Technology*. 2009;25(3):309–324.  
<https://doi.org/10.1179/174328408X389463>
  21. Li Z., Cui Y., Yu Z., Liu C. In-situ fabrication of Ti<sub>2</sub>AlNb-based alloy through double-wire arc additive manufacturing. *Journal of Alloys and Compounds*. 2021;876:160021. <https://doi.org/10.1016/j.jallcom.2021.160021>
  22. Shchitsyn Yu.D., Tytkin Yu.M. Interaction of a compressed arc with a crater cavity during keyhole plasma arc welding. *Svarochnoe proizvodstvo*. 1994;6:32–33. (In Russ.).  
Щицын Ю.Д., Тыткин Ю.М. Взаимодействие сжатой дуги с полостью кратера при плазменной сварке проникающей дугой. *Сварочное производство*. 1994;6:32–33.
  23. Stefanescu D.M., Ruxanda R. Solidification structures of titanium alloys. In: *ASM Handbook Metallography and Microstructures*. 2004. P. 116–126.  
<https://doi.org/10.31399/asm.hb.v09.a0003728>
  24. Wu J. Xu L., Lu Z., Cui Y., Yang R. Preparation of powder metallurgy Ti–22Al–24Nb–0.5Mo alloys and electron beam welding. *Acta Metallurgica Sinica*. 2016;52(9):1070–1078.  
<https://doi.org/10.11900/0412.1961.2016.00019>
  25. Zhang K., Lei Z., Chen Y., Yang K., Bao Y. Heat treatment of laser-additive welded Ti<sub>2</sub>AlNb joints: Microstructure and tensile properties. *Materials Science and Engineering: A*. 2019;744:436–444.  
<https://doi.org/10.1016/j.msea.2018.12.058>
  26. Zhang K., Ni L., Lei Z., Chen Y., Hu X. Microstructure and tensile properties of laser welded dissimilar Ti–22Al–27Nb and TA15 joints. *The International Journal of Advanced Manufacturing Technology*. 2016;87:1685–1692.  
<https://doi.org/10.1007/s00170-016-8579-3>
  27. Wang L., Sun D., Li H., Gu X., Shen C. Microstructures and mechanical properties of a laser-welded joint of Ti<sub>3</sub>Al–Nb alloy using pure Nb filler metal. *Metals*. 2018;8(10):785. <https://doi.org/10.3390/met8100785>
  28. Chen X., Xie F.Q., Ma T.J., Li W.Y., Wu X.Q. Effects of post-weld heat treatment on microstructure and mechanical properties of linear friction welded Ti<sub>2</sub>AlNb alloy. *Materials & Design*. 2016;94:45–53.  
<https://doi.org/10.1016/j.matdes.2016.01.017>
  29. Chen W., Chen Z.Y., Wu C.C., Li J.W., Tang Z.Y., Wang Q.J. The effect of annealing on microstructure and tensile properties of Ti–22Al–25Nb electron beam weld joint. *Intermetallics*. 2016;75:8–14.  
<https://doi.org/10.1016/j.intermet.2016.02.006>
  30. Jiao X., Kong B., Tao W., Liu G., Ning H. Effects of annealing on microstructure and deformation uniformity of Ti–22Al–24Nb–0.5Mo laser-welded joints. *Materials & Design*. 2017;130:166–174.  
<https://doi.org/10.1016/j.matdes.2017.05.005>
  31. Lei Z., Zhou H., Chen Y., Zhang K., Li B. A comparative study of deformation behaviors between laser-welded joints and base metal of Ti–22Al–24.5Nb–0.5Mo alloy. *Journal of Materials Engineering and Performance*. 2019;28(8):5009–5020.  
<https://doi.org/10.1007/s11665-019-04224-7>
  32. Lu B., Yin J., Wang Y., Yang R. Gas tungsten arc welding of Ti<sub>2</sub>AlNb based alloy sheet. In: *Proc. 12<sup>th</sup> World Conf. Titan* (China, Beijing, 19–24 June 2011). 2012. Vol. 1. P. 816–818.

## Information about the authors

**Stanislav V. Naumov** – Cand. Sci. (Eng.), Associate Professor of the Department of Materials Science and Nanotechnology (MSN), Senior Research Scientist of the Laboratory of Bulk Nanostructured Materials (BNM), Belgorod National Research University (BSU).

<https://orcid.org/0000-0002-4084-8861>

E-mail: NaumovStanislav@yandex.ru

**Dmitrii O. Panov** – Cand. Sci. (Eng.), Associate Professor of the Department MSN, Senior Research Scientist of the Laboratory BNM, BSU.

<https://orcid.org/0000-0002-8971-1268>

E-mail: dimmak-panov@mail.ru

**Ruslan S. Chernichenko** – Junior Researcher of the Laboratory BNM, BSU.

<https://orcid.org/0000-0002-8619-0700>

E-mail: chernichenko@bsu.edu.ru

**Vitaly S. Sokolovsky** – Cand. Sci. (Eng.), Research Scientist of the Laboratory BNM, BSU.

<https://orcid.org/0000-0001-5607-2765>

E-mail: sokolovskiy@bsu.edu.ru

**Gennady A. Salishchev** – Dr. Sci. (Eng.), Professor of the Department MSN, Head of the Laboratory BNM, BSU.

<https://orcid.org/0000-0002-0815-3525>

E-mail: salishchev\_g@bsu.edu.ru

**Evgeny B. Alekseev** – Cand. Sci. (Eng.), Head of the Sector of All-Russia Institute of Aviation Materials of the National Research Center “Kurchatov Institute”.

Scopus-ID: 56581528500

E-mail: hiten\_@mail.ru

**Sergey D. Neulybin** – Cand. Sci. (Eng.), Head of the Laboratory of methods for creating and designing systems “Material–Technology–Design”, Perm National Research Polytechnic University (PNRPU).

<https://orcid.org/0000-0003-1846-1502>

E-mail: sn-1991@mail.ru

**Dmitry S. Belinin** – Cand. Sci. (Eng.), Associate Prof. of the Department of Welding, Metrology and Materials Engineering (WMME), PNRPU.

<https://orcid.org/0000-0001-5462-0908>

E-mail: 5ly87@mail.ru

**Yuri D. Shchitsyn** – Dr. Sci. (Eng.), Professor, Head of the Department WMME, PNRPU.

<https://orcid.org/0000-0002-3499-4184>

E-mail: schicin@pstu.ru

**Vasily V. Lukianov** – Cand. Sci. (Eng.), Head of the Department of Complex-Profile Shaping, NPA “Technopark AT”.

<https://orcid.org/0009-0006-3621-3966>

E-mail: lukianovv@bk.ru

## Информация об авторах

**Станислав Валентинович Наумов** – к.т.н., доцент кафедры материаловедения и нанотехнологий (МиН), ст. науч. сотрудник лаборатории объемных наноструктурных материалов (ОНМ), Белгородский государственный национальный исследовательский университет (НИУ «БелГУ»).

<https://orcid.org/0000-0002-4084-8861>

E-mail: NaumovStanislav@yandex.ru

**Дмитрий Олегович Панов** – к.т.н., доцент кафедры МиН, ст. науч. сотрудник лаборатории ОНМ, НИУ «БелГУ».

<https://orcid.org/0000-0002-8971-1268>

E-mail: dimmak-panov@mail.ru

**Руслан Сергеевич Черниченко** – мл. науч. сотрудник лаборатории ОНМ, НИУ «БелГУ».

<https://orcid.org/0000-0002-8619-0700>

E-mail: chernichenko@bsu.edu.ru

**Виталий Сергеевич Соколовский** – к.т.н., науч. сотрудник лаборатории ОНМ, НИУ «БелГУ».

<https://orcid.org/0000-0001-5607-2765>

E-mail: sokolovskiy@bsu.edu.ru

**Геннадий Алексеевич Салищев** – д.т.н., профессор кафедры МиН, зав. лабораторией ОНМ, НИУ «БелГУ».

<https://orcid.org/0000-0002-0815-3525>

E-mail: salishchev\_g@bsu.edu.ru

**Евгений Борисович Алексеев** – к.т.н., начальник сектора Всероссийского научно-исследовательского института авиационных материалов Национального исследовательского центра «Курчатовский институт».

Scopus-ID: 56581528500

E-mail: hiten\_@mail.ru

**Сергей Дмитриевич Неulybin** – к.т.н., руководитель лаборатории методов создания и проектирования систем «Материал–Технология–Конструкция», Пермский национальный исследовательский политехнический университет (ПНИПУ).

<https://orcid.org/0000-0003-1846-1502>

E-mail: sn-1991@mail.ru

**Дмитрий Сергеевич Белинин** – к.т.н., доцент кафедры сварочного производства, метрологии и технологии материалов (СПМТМ), ПНИПУ.

<https://orcid.org/0000-0001-5462-0908>

E-mail: 5ly87@mail.ru

**Юрий Дмитриевич Щицын** – д.т.н., профессор, зав. кафедрой СПМТМ, ПНИПУ.

<https://orcid.org/0000-0002-3499-4184>

E-mail: schicin@pstu.ru

**Василий Васильевич Лукьянов** – к.т.н., начальник отдела сложнопрофильного формообразования, НПА «Технопарк АТ».

<https://orcid.org/0009-0006-3621-3966>

E-mail: lukianovv@bk.ru

## Contribution of the authors

**S.V. Naumov** – formation of the main concept, planning and conducting experiments, writing the text, formulation of the conclusions.

**D.O. Panov** – organization and conducting of microstructural studies, writing the text, correction of the text and conclusions.

**R.S. Chernichenko** – carrying out mechanical tests of samples, analysis of the research results.

**V.S. Sokolovsky** – preparing samples for experiments, conducting EBSD analysis.

**G.A. Salishchev** – scientific guidance, goal and objectives of the study, participating in the discussion of the results, correcting the article.

**E.B. Alekseev** – producing the initial alloy for experiments.

**S.D. Neulybin** – management and conducting of welding studies, participating in the discussion of the results, correction of the text.

**D.S. Belinin** – preparing samples and conducting of welding studies.

**Yu.D. Shchitsyn** – provision of the resources, participating in the discussion of the welding results.

**V.V. Lukianov** – provision of the resources, planning experiments.

## Вклад авторов

**С.В. Наумов** – формирование основной концепции, планирование и проведение экспериментальных работ, подготовка текста, формулировка выводов.

**Д.О. Панов** – организация и проведение микроструктурных исследований, подготовка текста статьи, корректировка выводов.

**Р.С. Черниченко** – проведение механических испытаний образцов, анализ результатов исследований.

**В.С. Соколовский** – подготовка образцов для экспериментов, проведение EBSD-анализа.

**Г.А. Салищев** – научное руководство, постановка цели и задач работы, участие в обсуждении результатов, правка статьи.

**Е.Б. Алексеев** – изготовление исходного сплава для экспериментов.

**С.Д. Неулыбин** – руководство и проведение сварочно-технологических работ, участие в обсуждении результатов, корректировка текста статьи.

**Д.С. Белинин** – подготовка образцов и проведение сварочно-технологических работ.

**Ю.Д. Щицын** – обеспечение ресурсами, участие в обсуждении результатов сварочно-технологических работ.

**В.В. Лукьянов** – обеспечение ресурсами, планирование экспериментальных работ.

*The article was submitted 20.12.2023, revised 28.01.2024, accepted for publication 01.02.2024*

*Статья поступила в редакцию 20.12.2023, доработана 28.01.2024, подписана в печать 01.02.2024*

UDC 621.74 + 669.018

<https://doi.org/10.17073/0021-3438-2024-2-30-43>

Research article

Научная статья



# Selection of heat treatment and its impact on the structure and properties of AK10M2N–10%TiC composite material obtained via SHS method in the melt

A.R. Luts, Yu.V. Sherina, A.P. Amosov, E.A. Minakov, I.D. Ibatullin

Samara State Technical University

244 Molodogvardeyskaya Str., Samara 443100, Russia

✉ Alfiya R. Luts (alya\_luts@mail.ru)

**Abstract:** The composite materials based on the Al–Si system alloys, strengthened with a highly dispersed titanium carbide phase, possess improved characteristics and belong to the group of promising structural materials. Currently, self-propagating high-temperature synthesis (SHS) based on the exothermic interaction, wherein titanium and carbon precursors directly involve in the melt, is the most accessible and effective method to obtain them. This paper proves the feasibility and demonstrates the successful synthesis of a 10 wt.% titanium carbide phase in the melt of the AK10M2N alloy, resulting in the AK10M2H-10% TiC composite material. Samples of the matrix alloy and the composite material were subjected to heat treatment according to the T6 mode, with various temperature-time parameters for hardening and aging operations. Based on the results, optimal heat treatment modes were selected to ensure maximum hardness. We studied the macro- and microstructure of the obtained samples and performed micro X-ray spectral and X-ray diffraction phase analyses. Different groups of properties underwent comparative tests. It was established that the density of AK10M2N–10%TiC samples before and after heat treatment, according to optimal modes, is close to the calculated value. We showed that the combination of reinforcement and heat treatment significantly increases hardness, microhardness, and compressive strength, with a slight decrease in ductility. Additionally, it maintains the values of the coefficient of thermal linear expansion, high-temperature strength, and resistance to carbon dioxide and hydrogen sulfide corrosion at the level of the original alloy. The greatest effect was observed during the investigation of tribological characteristics: heat treatment of the composite material according to the recommended mode significantly reduces the wear rate and friction coefficient, eliminates seizure and tearing, and prevents temperature rise due to friction heating.

**Keywords:** composite material, aluminum, melt, titanium carbide, self-propagating high-temperature synthesis (SHS), heat treatment.

**For citation:** Luts A.R., Sherina Yu.V., Amosov A.P., Minakov E.A., Ibatullin I.D. Selection of heat treatment and its impact on the structure and properties of AK10M2N–10% TiC composite material obtained via SHS method in the melt. *Izvestiya. Non-Ferrous Metallurgy*. 2024;30(2):30–43.

<https://doi.org/10.17073/0021-3438-2024-2-30-43>

# Выбор термической обработки и исследование ее влияния на структуру и свойства композиционного материала АК10М2Н–10%TiС, полученного методом СВС в расплаве

А.Р. Луц, Ю.В. Шерина, А.П. Амосов, Е.А. Минаков, И.Д. Ибатуллин

Самарский государственный технический университет  
Россия, 443100, г. Самара, ул. Молодогвардейская, 244

✉ Альфия Расимовна Луц (alya\_luts@mail.ru)

**Аннотация:** Композиционные материалы на основе сплавов системы Al–Si, упрочненные высокодисперсной фазой карбида титана, характеризуются улучшенными свойствами и относятся к группе перспективных конструкционных материалов. В настоящее время наиболее доступным и эффективным способом их получения является самораспространяющийся высокотемпературный синтез (СВС), основанный на экзотермическом взаимодействии прекурсоров титана и углерода непосредственно в расплаве. В работе обоснована целесообразность и показан успешный опыт синтеза 10 мас.% фазы карбида титана в расплаве сплава АК10М2Н и получения композиционного материала АК10М2Н–10%TiС. На образцах матричного сплава и полученного на его основе композиционного материала реализована термическая обработка по режиму Т6 с различными температурно-временными параметрами операций закалки и старения, по результатам которых выбраны оптимальные условия термообработки, обеспечивающие получение максимальной твердости. Исследована макро- и микроструктура, проведены микрорентгеноспектральный и рентгенофазовый анализы полученных образцов. Выполнен комплекс сравнительных испытаний разных групп свойств. Установлено, что образцы АК10М2Н–10%TiС до и после проведения термической обработки по оптимальным режимам имеют плотность, близкую к расчетному значению. Показано, что совместное проведение армирования и термообработки способствует существенному повышению показателей твердости, микротвердости и прочности на сжатие при незначительном уменьшении пластичности, а также позволяет сохранить значения коэффициента термического линейного расширения, жаропрочности и стойкости к углекислотной и сероводородной коррозии на уровне исходного сплава. Наибольший эффект отмечен при исследовании трибологических характеристик: проведение термической обработки композиционного материала по рекомендованному режиму способствует существенному снижению скорости изнашивания и коэффициента трения, позволяет исключить схватывание и появление задиров, а также не допустить повышения температуры вследствие разогрева при трении.

**Ключевые слова:** композиционный материал, алюминий, расплав, карбид титана, самораспространяющийся высокотемпературный синтез (СВС), термическая обработка.

**Для цитирования:** Луц А.Р., Шерина Ю.В., Амосов А.П., Минаков Е.А., Ибатуллин И.Д. Выбор термической обработки и исследование ее влияния на структуру и свойства композиционного материала АК10М2Н–10%TiС, полученного методом СВС в расплаве. *Известия вузов. Цветная металлургия.* 2024;30(2):30–43.  
<https://doi.org/10.17073/0021-3438-2024-2-30-43>

## Introduction

The Al–Si system alloys, commonly known as silumins, are among the most common cast aluminum alloys. They are characterized by high casting properties, satisfactory weldability, and corrosion resistance, making them suitable for manufacturing medium and large critical duty cast parts such as compressor housings, crankcases, cylinder heads, pistons, and more.

Special alloys, which contain additional alloying components besides silicon, such as Cu, Mg, Mn, Ti, and less frequently Ni, Zr, Cr, etc., are the most com-

mon. The introduction of such additives enhances the strength characteristics of silumins, and the presence of copper and magnesium allows for heat treatment according to the T6 mode, which includes hardening followed by artificial aging to achieve additional strengthening. However, it remains important to find ways to further enhance the mechanical properties of silumins, as even after alloying and heat treatment, their properties remain lower than those of duralumins [1].

One of the most promising approaches is creating casting composite materials based on silumins by combining a matrix alloy with a dispersed phase constituted of particles of silicon or titanium carbides [2; 3]. Silicon carbide is produced in large volumes and is more affordable. However, it can react with the SiC filler and the matrix, forming the hexagonal lamellar Al<sub>4</sub>C<sub>3</sub> phase, which leads to instability in physical and mechanical properties and a decrease in corrosion resistance [4]. Titanium carbide reinforcement is less common but is a better choice: firstly, unlike the SiC hexagonal lattice, titanium carbide has a FCC lattice close in size to the lattice of matrix aluminum, so dispersed particles of this compound can effectively act as crystallization centers. Secondly, titanium carbide is characterized by higher physical and mechanical properties, such as a melting point of  $T_{\text{melt}} = 3433$  K (compared to 2873–2970 K for SiC); Young's modulus  $E = 440 \cdot 10^9$  N/m<sup>2</sup> ( $\geq 3350 \cdot 10^9$  N/m<sup>2</sup>); hardness  $HV = 32 \cdot 10^9$  N/m<sup>2</sup> ( $24 \div 28 \cdot 10^9$  N/m<sup>2</sup>); strength  $\sigma_{\text{ucs}} = 1.2 \div 1.54 \cdot 10^9$  N/m<sup>2</sup> ( $0.4 \div 1.7 \cdot 10^9$  N/m<sup>2</sup>) [5].

The final characteristics of composite material reinforced with dispersed carbide phases are largely determined by its production method [6; 7]. In terms of technological availability and cost-effectiveness, liquid-phase methods are preferable. These methods are subdivided into *ex situ*, where reinforcing particles are prepared in advance outside the matrix and later introduced into the melt, and *in situ*, where reinforcing particles are synthesized by chemical reactions directly in the matrix alloy during composite fabrication [8]. The most common method from the first group is mechanical mixing, which often leads to contamination with oxides and impurity elements and excludes the possibility of obtaining a highly dispersed reinforcing phase, as the particles tend to agglomerate [9]. The more promising method from the second group, self-propagating high-temperature synthesis (SHS), does not have these disadvantages. It can be implemented on standard foundry equipment, is characterized by low energy consumption due to the short duration of the process, and most importantly, it enables the synthesis of the titanium carbide phase from initial powders of carbon and titanium (or their compounds) with particle sizes from 100 nm in a wide range of concentrations [10].

A number of studies on liquid-phase reinforcement of silumins with carbide phases have been conducted in Russia. The study in [11] shows that mechanically mixing SiC particles into AK12, AK9, and AL25 alloys contributes to a deterioration of the castings' dendritic parameter and an increase in the modulus of elasticity,

hardness, and bearing capacity. In [5; 12], researchers compared antifriction compositions based on the AK12 and AK12M2MgN alloys reinforced with dispersed SiC or TiC particles in amounts of 5 or 10 wt.%, with and without intermetallic phases (Al<sub>3</sub>Me type compounds). It was found that the optimal filler is a titanium carbide phase in the amount of 10 wt.%, as this increased wear resistance up to 10 times and reduced the coefficient of friction by 60 %.

There are also several publications on heat treatment of silumin-based composites [13–16]. The paper [14] showed that the AK12M2MgN alloy, reinforced with endogenous (formed in the melt) AlTi, Al<sub>3</sub>Ti, Al<sub>3</sub>Ni, etc. phases and exogenous (introduced from outside) SiC and Al<sub>2</sub>O<sub>3</sub> nano- and microparticles in the amount of 0.1 wt.%, exhibits a hardness increase of 50 MPa at  $t = 20$  °C and 30 MPa at 300 °C. After heat treatment (holding at 515 °C, quenching in water, and aging at 210 °C), the hardness increased by 110–160 MPa and 60–80 MPa, respectively. Similar results were obtained in [15; 16], where mechanical stirring of SiC dispersed phase up to 15 wt.% into the AK9h, AK12MMrN, and A359 alloys with subsequent T6 heat treatment accelerated the aging process and increased hardness overall. The authors attributed this to the enhanced density of dislocations in the composites and the difference in elastic moduli between the matrix and the reinforcing phase.

These studies provide convincing evidence that producing and thermally treating composites based on silumins is promising. However, it is also clear that domestic developments mainly focus on obtaining composites through mechanical stirring and primarily use silicon carbide as the filler. In contrast, foreign studies cover a wider range of production methods and composite structures. For instance, foreign researchers show significant interest in titanium carbide, both introduced from the outside and formed in the melt of silumins by the SHS method [17–20]. In [20], researchers added an Al + Si powder mixture in amounts of 0–40 % to a charge of titanium and graphite, then mixed, pressed in an argon atmosphere, and introduced it into the Al–Si eutectic melt heated to 900 °C. X-ray phase analysis showed that at any content of Al and Si powders, the final composite structure included only Al, Si, and TiC phases, confirming that SHS of the carbide phase can be conducted directly in the silumin melt.

Care must be taken when selecting the temperature modes for creating and heat treating such composites, as several studies indicate that the titanium carbide phase becomes thermally unstable at high

temperatures and long holding periods in the presence of silicon [21–24]. In [22], 10 wt.% TiC particles were introduced into the Al–7%Si melt heated to 700 °C. After crystallization, the samples were oven-exposed at temperatures ranging from 500 to 1000 °C for 6 hours. It was found that in the range of 600–800 °C, titanium carbide decomposes, forming Ti–Al–Si ternary phase and Al<sub>4</sub>C<sub>3</sub> intermetallic phase, while at temperatures above 800 °C, the reverse process occurs, and the carbide phase content nearly restores to the initial level. However, [23] demonstrated that during a 20-minute holding at 800 °C of the Al–12Si/TiC composite, titanium carbide decomposes completely and irretrievably because silicon atoms diffuse into the lattice of titanium carbide.

A similar conclusion was made in [24]. At temperatures of 750 and 800 °C, TiC particles decompose to form Al<sub>4</sub>C<sub>3</sub> and TiAl<sub>x</sub>Si<sub>y</sub> phases, and at 900 and 1000 °C, they form Al<sub>4</sub>C<sub>3</sub> and TiAl<sub>x</sub>Si<sub>y</sub> phases, and at  $t = 900$  and 1000 °C, to form Al<sub>4</sub>C<sub>3</sub> and Ti<sub>3</sub>SiC<sub>2</sub>.

All authors agree that the carbide phase can degrade at high temperatures of the silumin melt and during prolonged holding times. Therefore, the SHS method is particularly relevant, as it requires minimal time and the entire cycle of obtaining the composite material, from charge input to crystallization of the finished product, lasts no more than 10 minutes, which is insufficient for carbide phase decomposition.

Another important issue is phase formation in the presence of other alloying elements and carbide phase particles. The study [25] explores the influence of 1 % Fe on the structure and properties of the Al–12%Si–1%Fe–(0.4–0.8)%TiC composite obtained by the SHS method. It was found that with increasing titanium carbide content,  $\alpha$ -Al<sub>8</sub>Fe<sub>2</sub>Si of favorable morphology forms instead of the sharp-angled  $\beta$ -Al<sub>3</sub>FeSi phase, enhancing the tensile strength from 148.2 to 198.7 MPa, the yield strength from 84.7 to 93.5 MPa, and the relative elongation from 2.3 to 4.93 %.

Several studies have focused on the addition of magnesium, with varying findings. The authors of [26] mixed 10 wt.% TiC into the silumin composition Al–14.2%Si–0.3%Mg, additionally introduced 1 wt.% Mg, and subjected the mixture to heat treatment (holding at 525 °C, quenching in cold water, and aging at 151–155 °C). They attributed the significant increase in wear resistance to the uniform carbide phase distribution, decreased surface tension, and increased wettability caused by the presence of magnesium. However, in [27], which studied phase formation in an Al–Mg–Si alloy reinforced with 2 % TiC during aging at 160 °C, it was found that the carbide phase

prevents the formation of Guinier–Preston zones and the release of strengthening metastable Mg–Si phases in the aluminum matrix. As a result, after heat treatment, the maximum hardness of the composite (75.8 HV) was lower than that of the matrix alloy (123 HV). The role of magnesium is also negatively evaluated in [28], where the Al–3.5vol.%TiC alloy obtained by the SHS method was introduced into the Al–10%Si melt at 850 °C to form 2 vol.% TiC, with 0.2–0.4 wt.% Mg added to some samples. After synthesis, the samples were subjected to heat treatment (holding at 540 °C, quenching in cold water, and aging at 160 °C). Based on the microstructure analysis, the authors concluded that the Mg<sub>2</sub>Si compound forms but segregates near TiC particles and facilitates the interaction between carbide particles and silicon. This leads to the formation of complex phases such as Al<sub>3</sub>TiSi<sub>x</sub>C<sub>y</sub> and Al<sub>3</sub>Ti, which slightly enhance hardness and strength but significantly reduce the material's ductility.

Thus, the process of structure formation in composites based on special silumins is not entirely clear, but it is evident that their aging kinetics differ significantly from those of initial silumins, and the phase composition can undergo significant changes. However, all studies indicate that the presence of a carbide phase contributes to enhanced hardness and wear resistance [29; 30]. This suggests that such reinforcement is most appropriate for tribological materials requiring this complex of properties, such as heat-resistant piston aluminum alloys. In this group, the most widespread materials are special silumins with nickel, particularly the AK10M2N alloy, which is extensively used to manufacture piston castings for internal combustion engines. Previous studies conducted by Samara State Technical University demonstrated the feasibility of conducting SHS with AK10M2H silumin containing 10 wt.% TiC. This process reduced the friction coefficient of the composite material by three times without subsequent heat treatment, while increasing the seizure load by at least 1.5 times compared to the matrix alloy [31].

To further enhance the material's characteristics, we conducted this study to select the optimal heat treatment mode and investigate its effect on the structure and properties of the AK10M2N–10%TiC composite material obtained via SHS in the melt.

## Research methodology

The AK10M2N alloy produced by “Sammet” LLC (Russia) according to GOST 30620-98, was used as

a matrix for the melt. To obtain a charge mixture, powders of titanium (TPP-7, TS 1715-449-05785388) and carbon (P-701, GOST 7585-86), taken in a stoichiometric ratio for the SHS reaction  $\text{Ti} + \text{C} = \text{TiC}$ , were mixed with salt  $\text{Na}_2\text{TiF}_6$  (GOST 10561-80) in the amount of 5 % of the charge mass. The resulting composition was then divided into 3 equal portions, wrapped in aluminum foil and alternately introduced into the silumin melt heated to a temperature of 900 °C in a graphite crucible of a PS-20/12 melting furnace (Russia) for conducting SHS reaction and obtaining composites.

To study the microstructure, the samples were etched with a solution of 50%HF + 50%HNO<sub>3</sub> for 10–15 s. Metallographic analysis was carried out on a JSM-6390A scanning electron microscope (“Jeol”, Japan) equipped with a JSM-2200 module for micro X-ray spectral analysis (MXSA).

The phase composition was determined by X-ray diffraction (XRD) phase analysis. X-ray spectra were recorded on an ARL X'tra automated diffractometer (“Thermo Scientific”, Switzerland) using  $\text{CuK}\alpha$ -radiation with continuous scanning in the range of angles  $2\theta = 20^\circ\text{--}80^\circ$  at a speed of 2 degrees/min. HighScore Plus software (PANalytical B.V., the Netherlands) was used to analyze the diffractograms.

The samples were subjected to thermal treatment in a SNOL laboratory chamber furnace with an operating temperature reaching 1300 °C.

The density of experimental samples was determined by hydrostatic weighing on VK-300 scales (Russia) of the 4th accuracy class according to GOST 20018-74.

The method based on measuring the elongation of cylindrical rods, 60 mm long and 7 mm in diameter, during heating was used to estimate the coefficient of thermal linear expansion (CTLE). The CTLE value was measured on a mechanical dilatometer under the following conditions: TXA thermocouple, type K; duration — 5 h; temperature limit value — 300 °C; the measurement interval — 25 °C. CTLE was calculated according to the formula

$$\alpha = \frac{l_2 - l_1}{l_1(t_2 - t_1)},$$

where  $\alpha$  is the temperature coefficient of linear expansion,  $\text{K}^{-1}$ ;  $t_1$  and  $t_2$  are initial and final test temperatures, K;  $l_1$  and  $l_2$  are sample lengths corresponding to  $t_1$  and  $t_2$ , mm.

Hardness of samples was determined on TSH-2M hardness tester (Russia) according to GOST 9012-59, after which the impression diameter was assessed on a Motic DM-111 microscope (Russia) and analyzed

using the Motic Educator software. The microhardness of the samples was measured on a standard PTM-3 microhardness tester (Russia) according to GOST 9450-76 using a diamond-pyramid hardness test with a square base and an interface angle at the apex of 136°; the weight on the indenter was 100 g. Compression tests were carried out according to GOST 25.503-97 on type III samples with the diameter  $d_0 = 20$  mm under a load up to 300 kN. To evaluate the heat resistance, compression tests were performed at temperatures of 150 and 250 °C using an Instron 8802 universal machine (USA) with a 3119-406 thermal chamber at a load of 100 kN; the thermocouple was mounted directly on the sample; the traverse speed reached 1 mm/min.

Corrosion resistance was evaluated according to GOST 13819-68 in the Coat Test 3.3.150.150 autoclave complex under the following conditions: an aqueous solution of 5 % NaCl; gas phase CO<sub>2</sub> (1 Pa) + H<sub>2</sub>S (0.5 MPa) + N<sub>2</sub> (3.5 MPa) at 80 °C; duration — 240 h; total pressure — 5 MPa. Corrosion resistance parameters were calculated according to GOST 9.908-85.

Tribological tests were carried out using the “Universal-1B” universal tribological complex (Russia), according to the ring-plane test scheme, which simulates the operating conditions of friction surfaces “piston — piston pin” in the internal combustion engine in the following mode: normal contact load — 400 N; counterbody rotation speed — 600 rpm (average linear velocity in the contact zone is 0.157 m/s); test duration — 60 min (or until complete seizure).

## Results and discussion

During the TiC synthesis, an active and rapid SHS reaction with bright flashes was observed in the AK10M2N melt. The fractures of AK10M2N-10%TiC samples obtained after solidification were characterized by homogeneous gray color, had neither foreign inclusions nor residues of unreacted charge.

The AK10M2N alloy belongs to the group of special piston silumins with nickel addition. The T1 mode, that includes artificial aging only, can be used for its heat treatment aimed at enhancing its strength characteristics. Moreover, the material partially hardens during cooling in the casting mold, but in this case hardening will not be significant. More frequently the T6 mode is used. It includes hardening within the range of 515–535 °C and artificial aging in the interval of 160–190 °C [32–34]. Based on the review of the recommended modes, the following were selected as experimental ones:

1) heating for hardening at  $t = 515$  °C for 1–2 h with cooling in cold water and aging at  $t = 190$  °C for 1–6 h;

2) heating for hardening at  $t = 535$  °C for 1–2 h with cooling in cold water and aging at  $t = 160$  °C for 1–6 h.

Hardness was used as a quantitative criterion to evaluate the heating effect.

The analysis of the obtained results showed that the maximum hardness values are achieved by heating for hardening at  $t = 515$  °C followed by artificial aging at  $t = 190$  °C for 2 h, but with different periods of holding for hardening: for the AK10M2N matrix alloy the maximum hardness of 152 HB was observed after 2 h of holding, while for the AK10M2N–10%TiC sample, the hardness of 171 HB was registered after 1 h of holding (Fig. 1). The highly dispersed particles of titanium carbide obviously contribute to the increase in vacancy concentration, dislocation density, grain refinement, which, in combination, intensify structural transformations. The above modes were found to be optimal, and further studies were performed after these types of heat treatment.

The microstructural study of the samples after heat treatment revealed that many rounded particles, their sizes ranging from 180 nm to 2  $\mu$ m, were present in the composite (Fig. 2). MXSA that was conducted further (Fig. 3) indicates the presence of Ti and C in the composite structure, which confirms their assimilation in the melt, as well as other elements (Si, Cu, Mg, Ni, and Fe) included in the initial AK10M2N alloy.

According to the sources [1; 32], after heat treatment of piston silumins, magnesium is usually present in their structure in an amount of about 1% in the

form of eutectic inclusions of the  $Mg_2Si$  phase, but it can also form other Mg-containing compounds. Copper in alloys with nickel forms the main strengthening phases  $Al_2Cu$  and  $Al_5Cu_2Mg_8Si_6$ , as well as ternary compounds  $Al_7Cu_4Ni$  and  $Al_3CuNi$ . Nickel with iron can form the  $Al_9FeNi$  compound, eutectic inclusions of which are undesirable due to rough morphology. However, the following phases are most likely to form:  $Al_3Ni$ ,  $Al_6Cu_3Ni$  and  $Al_3(Ni,Cu)_2$ . The XRD analysis was performed to clarify the obtained phase composition, which revealed the presence of  $Al_2Cu$  and  $Al_3Ni$  intermetallic phases in the matrix alloy and TiC ceramic phase (9 wt.%) in the composite, which is quite an acceptable level, taking into account some inhomogeneity of its distribution, as well as the presence of the same  $Al_2Cu$ ,  $Al_3Ni$  phases (Fig. 4). We can also assume the presence of other phases from the above-mentioned list in too small an amount to be detected by the XRD method.

### Investigation of properties of the AK10M2N alloy and the AK10M2N–10%TiC composite material after heat treatment

We conducted comparative studies of the samples of the initial alloy and the AK10M2N–10%TiC composite material before and after heat treatment according to the recommended modes.

Initially, the density and porosity of the samples were determined. The obtained data are presented in Table 1. The comparison of theoretical ( $\rho_t$ ) and experimental ( $\rho_e$ ) density revealed that these values are very close and the porosity is 0. This phenomenon is not typical for pro-

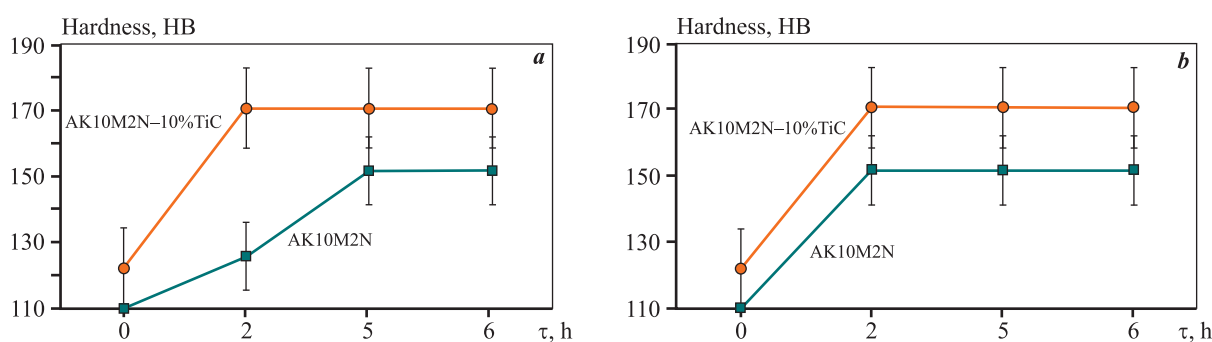


**Fig. 1.** The hardness change of the AK10M2N alloy and the AK10M2N–10%TiC composite material after heating for hardening with holding for 1 h (a) and 2 h (b) at  $t = 515$  °C, cooling in cold water and artificial aging at a temperature of  $t = 190$  °C for 1–6 h

**Рис. 1.** Изменение твердости сплава АК10М2Н и композиционного материала АК10М2Н–10%ТiС после нагрева под закалку с выдержкой 1 ч (а) и 2 ч (б) при  $t = 515$  °C, охлаждения в холодной воде и искусственного старения при  $t = 190$  °C в течение 1–6 ч

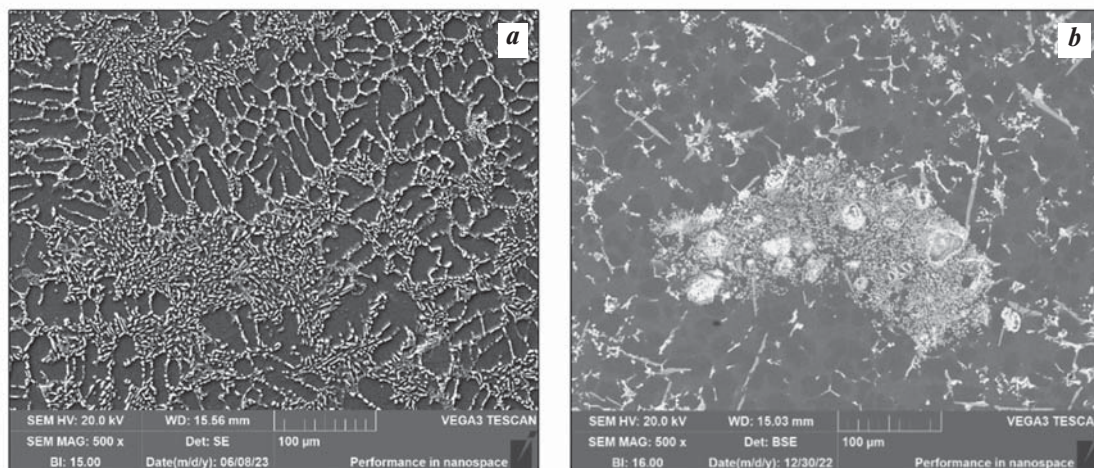
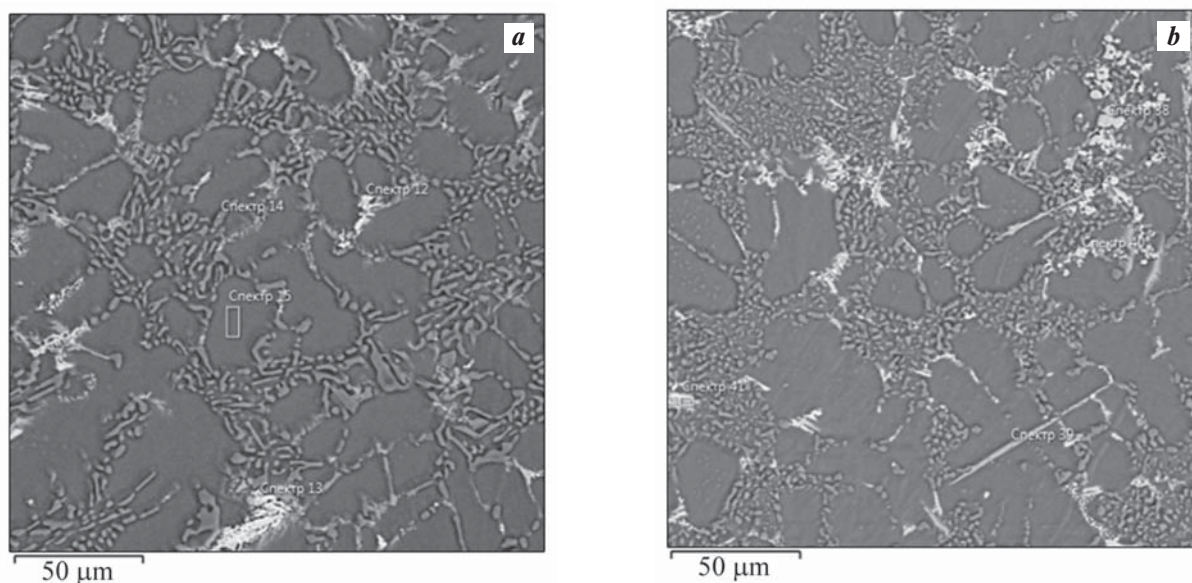


**Fig. 2.** Microstructure (×500) of the AK10M2N alloy (a) and the AK10M2N–10%TiC composite material (b) after heat treatment according to optimal modes

**Рис. 2.** Микроструктуры (×500) сплава АК10М2Н (a) и композиционного материала АК10М2Н–10%TiC (b) после термической обработки по оптимальному режиму



Marker number	Element content, wt.%				
	Al	Si	Ni	Cu	Mg
12	45.86	1.93	23.00	28.24	0.96
13	41.56	3.26	28.65	26.53	–
14	28.01	70.89	1.10	–	–
15	97.15	0.97	–	1.72	0.17

Marker number	Element content, wt.%						
	Al	Si	Ti	C	Ni	Cu	Fe
38	0.44	0.13	79.98	19.45	–	–	–
39	57.71	12.84	28.09	1.36	–	–	–
40	14.78	0.30	58.02	23.15	1.96	1.23	0.57
41	64.47	2.79	–	5.58	14.04	8.96	4.15

**Fig. 3.** MXSA analysis of the AK10M2N alloy (a) and the AK10M2N–10%TiC composite material (b) after heat treatment according to the optimal mode

**Рис. 3.** Результаты МРСА сплава АК10М2Н (a) и композиционного материала АК10М2Н–10%TiC (b) после термической обработки по оптимальному режиму

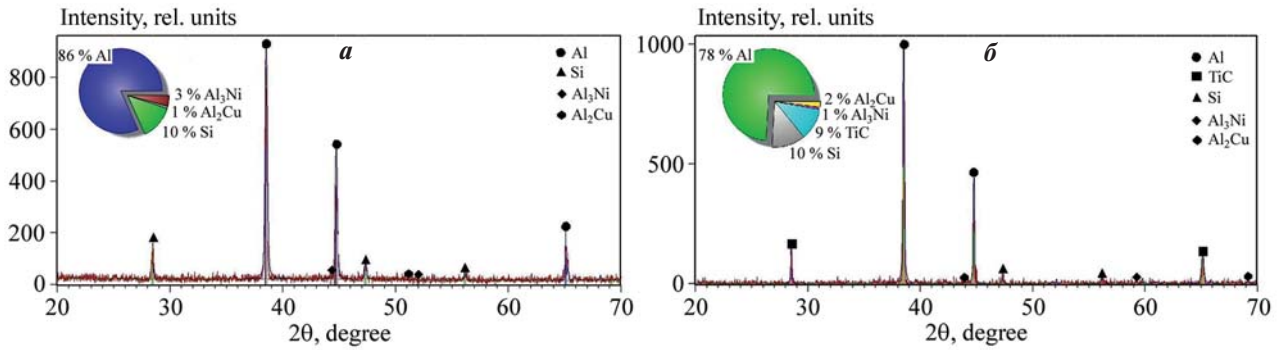


**Fig. 4.** X-ray diffraction patterns of the AK10M2N alloy (a) and the AK10M2N–10%TiC composite material (b) after heat treatment according to the optimal mode

**Рис. 4.** Дифрактограммы сплава АК10М2Н (а) и композиционного материала АК10М2Н–10%TiC (b) после термической обработки по оптимальному режиму

ducts obtained by SHS, but in this case it may indicate a high level of adhesive bonding at the interfaces.

For piston silumins, which include the AK10M2N alloy, the coefficient of thermal linear expansion (CTLE) is an important parameter [35; 36]. Figure 5 presents the results obtained at temperatures ranging from 30 to 300 °C. The maximum CTLE values were  $29.6 \cdot 10^{-6} \text{ K}^{-1}$  and  $25.1 \cdot 10^{-6} \text{ K}^{-1}$  for the AK10M2N sample and  $27.8 \cdot 10^{-6} \text{ K}^{-1}$  and  $26.1 \cdot 10^{-6} \text{ K}^{-1}$  for AK10M2N–10%TiC before and after heat treatment, respectively. The obtained values are close and after heat treatment in both cases slightly decrease, but the main conclusion is that reinforcement does not lower this index. This is especially important if we keep in mind that the titanium carbide compound’s own CTLE is higher than, for example, that of silicon carbide ( $6.52 \div 7.15 \cdot 10^{-6} \text{ K}^{-1}$  and  $4.63 \div 4.7 \cdot 10^{-6} \text{ K}^{-1}$ , respectively).

It should be noted that the obtained results are not consistent with the conclusions given in [37]. The latter study proves that CTLE of the composite material based on the aluminum alloy of the Al–Cu–Mg sys-

tem reinforced with 60 vol.% SiC using the compression impregnation method depends on the size of reinforcing particles. It was also found that as the size of silicon carbide particles increase (from 50 to 320 μm), the CTLE value decreases by 15–20 % at  $t = 20 \text{ °C}$  due to the shrinking proportion of interfacial boundaries with an unstable structure. In our case, there are highly dispersed particles that obviously form a significant number of interfacial boundaries, however, no increase in CTLE is registered. This can probably be attributed to the high degree of the particles coherence with the aluminum matrix as crystal lattice parameters are quite similar.

To evaluate the mechanical properties, we investigated the flow stress under uniaxial compression (until the first crack emerges), relative strain, hardness and microhardness (Table 2).

The results obtained showed that reinforcement with TiC particles to be followed by heat treatment can significantly enhance the strength and hardness values while maintaining sufficient plasticity reserve. These results are particularly noteworthy in view of

**Table 1. Density and porosity of the AK10M2N alloy and the AK10M2N–10%TiC composite material**

**Таблица 1. Плотность и пористость образцов АК10М2Н и АК10М2Н–10%TiC**

Composition	$\rho_t, \text{g/cm}^3$	$\rho_e, \text{g/cm}^3$	$P, \%$
AK10M2N without HT	2.720	–	–
AK10M2N after HT (hardening $t = 515 \text{ °C}$ , $\tau = 2 \text{ h}$ + aging $190 \text{ °C}$ , $2 \text{ h}$ )	2.720	–	–
AK10M2N–10%TiC without HT	2.847	2.831	0
AK10M2N–10%TiC after HT (hardening $515 \text{ °C}$ , $1 \text{ h}$ + aging $190 \text{ °C}$ , $2 \text{ h}$ )	2.847	2.840	0

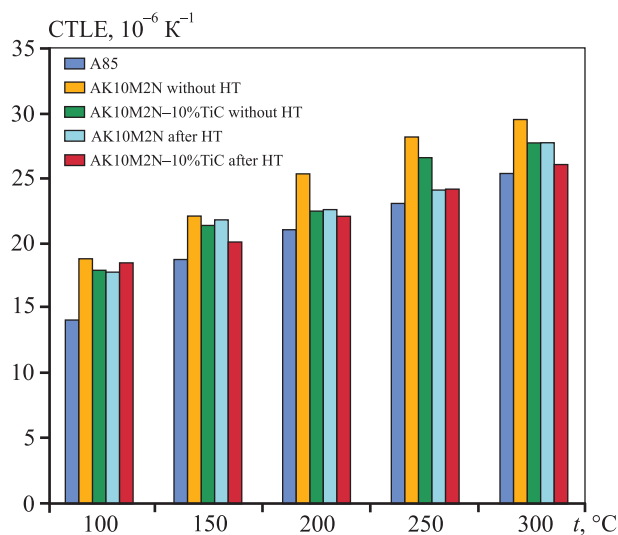


**Fig. 5.** Change in CTLE of the AK10M2N alloy and the AK10M2N–10%TiC composite material as a function of temperature

**Рис. 5.** Изменение КТЛР сплава АК10М2Н и композиционного материала АК10М2Н–10%TiC в зависимости от температуры

the fact that, according to [5], the introduction of 10 wt.% of reinforcing TiC particles, 40–100  $\mu\text{m}$  in size, into the AK12M2MgN aluminum alloy leads to a decrease in compressive strength from 489 to 470 MPa, and that of the deformation degree from 17.01 to 12.65 %. Obviously, the increased strength in our study can be attributed to the higher dispersion of the reinforcing phase and, consequently, its good wettability and adhesion.

The AK10M2N alloy belongs to the group of heat-resistant alloys, therefore, the compressive strength was further evaluated at elevated temperatures of 150 and 250  $^{\circ}\text{C}$  under a constant load of 100 kN (Fig. 6).

The analysis of the obtained data indicates that the values of the flow stress of both the matrix alloy and the composite material do not change throughout the temperature range.

Table 3 presents the results of evaluating the reinforcement and heat treatment impact on the samples corrosion resistance. The composites had a slightly higher corrosion depth index. However, in general, as

**Table 2. Mechanical and technological properties of the AK10M2N alloy and the AK10M2N–10%TiC composite material**

Таблица 2. Механические свойства сплава АК10М2Н и композиционного материала АК10М2Н–10%TiC

Sample composition	Hardness, HB	Micro-hardness HV, MPa	Compression tests	
			$\sigma_s$ , MPa	$\epsilon$ , %
AK10M2N without HT	1100	1135	464	24
AK10M2N after HT (hardening 515 $^{\circ}\text{C}$ , 2 h + aging 190 $^{\circ}\text{C}$ , 2 h)	1360	1363	558	33
AK10M2N–10%TiC without HT	1520	1502	447	22
AK10M2N–10%TiC after HT (hardening 515 $^{\circ}\text{C}$ , 1 h + aging 190 $^{\circ}\text{C}$ , 2 h)	1710	1779	587	20

**Table 3. Corrosion parameters of the AK10M2N alloy and the AK10M2N–10%TiC composite material**

Таблица 3. Коррозионные показатели сплава АК10М2Н и композиционного материала АК10М2Н–10%TiC

Sample composition	Mass loss, g	Mass loss per unit area, $\text{kg}/\text{m}^2$	Change in sample thickness, m	Corrosion rate, $\text{g}/(\text{m}^2 \cdot \text{h})$	Corrosion depth index, mm/year
AK10M2N without HT	0.0009	0.0003	0.0001	0.0012	0.000004
AK10M2N after HT (hardening 515 $^{\circ}\text{C}$ , 2 h + aging 190 $^{\circ}\text{C}$ , 2 h)	0.0038	0.0012	0.0004	0.0050	0.000020
AK10M2N–10%TiC without HT	0.0238	0.0076	0.0027	0.0316	0.000009
AK10M2N–10%TiC after HT (hardening 515 $^{\circ}\text{C}$ , 1 h + aging 190 $^{\circ}\text{C}$ , 2 h)	0.2193	0.0698	0.0245	0.2910	0.000090

**Table 4. Results of comparative tribological tests of the AK10M2N alloy and the AK10M2N–10%TiC composite material**

Таблица 4. Результаты сравнительных триботехнических испытаний сплава АК10М2Н и композиционного материала АК10М2Н–10%TiC

Sample	Wear rate, $\mu\text{m/h}$	Friction coefficient	Self-heating temperature at friction, $^{\circ}\text{C}$
AK10M2N without HT	22.25	0.57	75
AK10M2N after HT (hardening 515 $^{\circ}\text{C}$ , 2 h + aging 190 $^{\circ}\text{C}$ , 2 h)	4.25	0.12	70
AK10M2N–10%TiC without HT	0.5	0.09	60
AK10M2N–10%TiC after HT (hardening 515 $^{\circ}\text{C}$ , 1 h + aging 190 $^{\circ}\text{C}$ , 2 h)	0.25	0.03	66

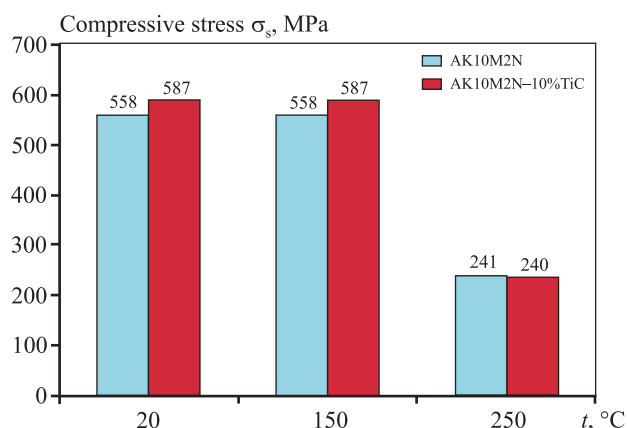


**Fig. 6.** Evaluation of the heat resistance of the AK10M2N alloy and the AK10M2N–10%TiC composite material after heat treatment according to the optimal mode

**Рис. 6.** Оценка жаропрочности сплава АК10М2Н и композиционного материала АК10М2Н–10%TiC после термической обработки по оптимальному режиму

it is the case with the matrix alloy, it does not exceed 0.001 mm/year, so we can state that the obtained materials are quite resistant to corrosion [38].

For the final analysis of tribological characteristics of prototypes, the conditions for operating friction surfaces “piston-piston pin” in the internal combustion engine were modeled (Table 4).

During the tests, the AK10M2N sample showed a tendency for seizure at friction and deep grooves were detected along the direction of friction, characteristic of abrasive wear. Heat treatment of the AK10M2N alloy significantly reduced the rate of wear and tearing, but the friction coefficient also increased by the end of the test. Reinforcement of the matrix alloy with the titanium carbide phase led to a significant improvement of tribological characteristics of the AK10M2N–10%TiC

composite, however, it is heat treatment that enables to achieve the minimum values of wear rate and friction coefficient.

## Conclusion

The conducted studies showed that heat treatment of composite materials with a silumin AK10M2N matrix reinforced with a highly dispersed titanium carbide phase is an effective way to control their structure and properties. The study established that SHS of the AK10M2N–10%TiC composite, followed by hardening at 515  $^{\circ}\text{C}$  and aging at 190  $^{\circ}\text{C}$ , produces a practically non-porous material and increases hardness by 35 HB, microhardness by 416 MPa, and compression yield stress by 29 MPa. Additionally, it reduces the wear rate by 17 times and the friction coefficient by 4 times, while maintaining the values of the coefficient of thermal linear expansion, corrosion resistance, and heat resistance at levels typical for the matrix alloy.

## References

1. Belov N.A. Phase composition of aluminum alloys. Moscow: MISIS, 2009. 234 p. (In Russ.).  
Белов Н.А. Фазовый состав алюминиевых сплавов. М.: МИСИС, 2009. 234 с.
2. Nyafkin A.N., Kosolapov D.V., Kurbatkina E.I. Influence of thermomechanical treatment on the formation of the structure in dispersed-reinforced aluminum alloy-based metal composite materials. *Powder Metallurgy and Functional Coatings*. 2023;17(3):22–29.  
<https://doi.org/10.17073/1997-308X-2023-3-22-29>  
Няфкин А.Н., Косолапов Д.В., Курбаткина Е.И. Влияние деформационно-термической обработки

- на формирование структуры дисперсно-армированного металлического композиционного материала на основе алюминиевого сплава. *Известия вузов. Порошковая металлургия и функциональные покрытия*. 2023;17(3):22–29.  
<https://doi.org/10.17073/1997-308X-2023-3-22-29>
3. Golla C.B., Babar Pasha M., Rao R.N., Ismail S., Gupta M. Influence of TiC Particles on mechanical and tribological characteristics of advanced aluminium matrix composites fabricated through ultrasonic-assisted stir casting. *Crystals*. 2023;13:1360.  
<https://doi.org/10.3390/cryst13091360>
  4. Kurbatkina E.I., Kosolapov D.V., Khodykin L.D., Nigmatov M.S. Study of the influence of silicon additives on the phase composition of aluminum composite materials reinforced with silicon carbide particles. *Aviatsionnyye materialy i tekhnologii*. 2014;S6:35–38. (In Russ.).  
<https://doi.org/10.18577/2071-9140-2014-0-s6-35-38>  
Курбаткина Е.И., Косолапов Д. В., Ходыкин Л.Д., Нигметов М.С. Исследование влияния добавки кремния на фазовый состав алюминиевых композиционных материалов, армированных частицами карбида кремния. *Авиационные материалы и технологии*. 2014;S6:35–38.  
<https://doi.org/10.18577/2071-9140-2014-0-s6-35-38>
  5. Mikheyev R.S., Chernyshova T.A. Aluminum-matrix composite materials with carbide hardening for solving problems of new technology. Moscow: Izdaniye RFFI, 2013. 353 p. (In Russ.).  
Михеев Р.С., Чернышова Т.А. Алюмоматричные композиционные материалы с карбидным упрочнением для решения задач новой техники. М.: Издание РФФИ, 2013. 353 с.
  6. Kurganova Yu. A., Kolmakov A. G. Structural metal matrix composite materials: textbook. Moscow: MGТУ im. N. E. Baumana, 2015. 141 p. (In Russ.). [https://urss.ru/images/add\\_ru/202831-1.pdf](https://urss.ru/images/add_ru/202831-1.pdf) (accessed: 19.01.2024).  
Курганова Ю.А., Колмаков А.Г. Конструкционные металломатричные композиционные материалы: Учебное пособие. М.: Издательство МГТУ им. Н.Э. Баумана, 2015. 141 с. [https://urss.ru/images/add\\_ru/202831-1.pdf](https://urss.ru/images/add_ru/202831-1.pdf) (дата обращения: 19.01.2024).
  7. Arunkumar S., Subramani Sundaram M., Suketh Kanna K.M., Vigneshwara S.A review on aluminium matrix composite with various reinforcement particles and their behavior. *Materials Today: Proceedings*. 2020;33(1):484–490.  
<https://doi.org/10.1016/j.matpr.2020.05.053>
  8. Luts A.R., Sherina Yu.V., Amosov A.P., Kachura A.D. Liquid matrix SHS manufacturing and heat treatment of Al–Mg composites reinforced with fine titanium carbide. *Izvestiya. Non-Ferrous Metallurgy*. 2023;29(4):70–86.  
<https://doi.org/10.17073/0021-3438-2023-4-70-86>  
Луц А.Р., Шерина Ю.В., Амосов А.П., Качура А.Д. Жидкофазное получение методом СВС и термическая обработка композитов на основе алюминиево-магниевого сплава, упрочненных высокодисперсной фазой карбида титана. *Известия вузов. Цветная металлургия*. 2023;4:70–86.  
<https://doi.org/10.17073/0021-3438-2023-4-70-86>
  9. Nath H., Amosov A.P. SHS amidst other new processes for in-situ synthesis of Al-matrix composites: A review. *International Journal of Self-Propagating High-Temperature Synthesis*. 2016;(25):50–58.  
<http://doi.org/10.3103/S106138621601009X>
  10. Amosov A.P., Luts A.R., Latukhin E.I., Ermoshkin A.A. Application of SHS processes for in situ production of aluminum-matrix composite materials discretely reinforced with nanoscale titanium carbide particles: Overview. *Russian Journal of Non-Ferrous Metals*. 2016;57(2):106–112.  
<http://doi.org/10.3103/S1067821216020024>  
Амосов А.П., Луц А.Р., Латухин Е.И., Ермошкин А.А. Применение процессов СВС для получения in situ алюмоматричных композиционных материалов, дискретно армированных наноразмерными частицами карбида титана: Обзор. *Известия вузов. Цветная металлургия*. 2016;(1):39–49.  
<https://doi.org/10.17073/0021-3438-2016-1-39-49>
  11. Kurganova Yu.A., Kolmakov A.G., Yijin Chen, Kurganov S.V. Study of the mechanical properties of promising aluminum matrix composite materials reinforced with SiC and Al<sub>2</sub>O<sub>3</sub>. *Materialovedeniye*. 2021;6:34-38. (In Russ.).  
<http://doi.org/10.31044/1684-579X-2021-0-6-34-38>  
Курганова Ю.А., Колмаков А.Г., Ицзинь Чэнь, Курганов С.В. Исследование механических свойств перспективных алюмоматричных композиционных материалов, армированных SiC и Al<sub>2</sub>O<sub>3</sub>. *Материаловедение*. 2021;6:34–38.  
<http://doi.org/10.31044/1684-579X-2021-0-6-34-38>
  12. Mikheev R.S., Kobernik N.V., Kalashnikov I.E., Bolotova L.K., Kobeleva L.I. Tribological properties of anti-friction coatings based on composite materials. *Perspektivnyye materialy*. 2015;3:48–54.  
Михеев Р.С., Коберник Н.В., Калашников И.Е., Болотова Л.К., Кобелева Л.И. Триботехнические свойства антифрикционных покрытий на основе композиционных материалов. *Перспективные материалы*. 2015;3:48–54.
  13. Kurbatkina E.I., Shavnev A.A., Kosolapov D.V., Gololobov A.V. Features of thermal treatment of composite materials with aluminum matrix (Review). *Trudy*

- VIAM. 2017;11:82–97. URL: <http://viam-works.ru/ru/articles?year=2017&num=11> (accessed: 19.01.2024). (In Russ.).  
<http://dx.doi.org/10.18577/2307-6046-2017-0-11-9-9>
- Курбаткина Е.И., Шавнев А.А., Косолапов Д.В., Голлобов А.В. Особенности термической обработки композиционных материалов с алюминиевой матрицей (обзор). *Труды ВИАМ*. 2017;11:82–97. URL: <http://viam-works.ru/ru/articles?year=2017&num=11> (дата обращения: 19.01.2024).  
<http://dx.doi.org/10.18577/2307-6046-2017-0-11-9-9>
14. Prusov E.S., Panfilov A.A., Kechin V.A. Role of powder precursors in production of composite alloys using liquid-phase methods. *Russian Journal of Non-Ferrous Metals*. 2017; 58(3):308–316.  
<http://doi.org/10.3103/S1067821217030154>  
Прусов Е.С., Панфилов А.А., Кечин В.А. Роль порошковых прекурсоров при получении композиционных сплавов жидкофазными методами. *Известия вузов. Порошковая металлургия и функциональные покрытия*. 2016;2:47–58.  
<http://doi.org/10.17073/1997-308X-2016-2-47-58>
  15. Aksenov A.A. Optimization of the composition and structure of composite materials on aluminum and copper bases, obtained by liquid-phase methods and mechanical alloying: Abstract of dissertation of Dr. Sci. (Eng.). Moscow: MISIS, 2007. (In Russ.).  
Аксенов А.А. Оптимизация состава и структуры композиционных материалов на алюминиевой и медной основах, получаемых жидкофазными методами и механическим легированием: Автореф. дис. ... д.т.н. М.: МИСИС, 2007.
  16. Churyumov A.Y., Mohamed I.A. Microstructure and mechanical properties of composite materials based on the Al–Si–Mg system reinforced with sic particles and obtained by pressure crystallization. *Metal Science and Heat Treatment*. 2019; 60(9–10):571–573.  
<http://doi.org/10.1007/s11041-019-00321-5>  
Чурюмов А.Ю., Мохамед И.А. Микроструктура и механические свойства композиционных материалов на основе системы Al–Si–Mg армированных частиц SiC и полученных кристаллизацией под давлением. *Металловедение и термическая обработка металлов*. 2018;9:19–22.
  17. Joseph O.O., Afolalu A.S., Abioye A.A., Agbo S.E., Olatunde S.F., Omotehinwa O.S. Effect of TiC addition on the mechanical properties and microstructure of Al–Si alloy. *Materials Today: Proceedings*. 2021;38(2): 784–788.  
<https://doi.org/10.1016/j.matpr.2020.04.544>
  18. Honglei Xi, Wenlong Xiao, Heng Li, Yu Fu, Ge Yi, Juhong Qie, Xiaozhao Ma, Chaoli Ma. Effects of sub-micron-sized TiC particles on the microstructure modification and mechanical properties of Al–Si–Mg alloy. *Journal of Alloys and Compounds*. 2023; 968:171963.  
<https://doi.org/10.1016/j.jallcom.2023.171963>
  19. Reese C.W., Gladstein A., Fedors J.M., De Andrade V., Mishra B., Shahani A.J., Taub A.I. In situ Al–TiC composites fabricated by self-propagating high-temperature reaction: insights on reaction pathways and their microstructural signatures. *Metallurgical and materials transactions*. 2020;51A:3587–3600.  
<https://doi.org/10.1007/s11661-020-05786-1>
  20. Mengxian Zhang, Yanqiu Huo, Li Ma. In situ TiC ceramic particles locally reinforced Al–Si matrix composites prepared by SHS-casting method from the Al–Si–Ti–C system. *International Journal of Applied Ceramic Technology*. 2014;11(4):723–731.  
<https://doi.org/10.1111/ijac.12097>
  21. Rui-Fen Guo, Ya Wang, Yun-Hai Ma, Ping Shen. Role of Si in the wetting of TiC by Al. *Journal of Materials Science*. 2021;56:7791–7798.  
<https://doi.org/10.1007/s10853-020-05496-4>
  22. López V.H., Scoles A., Kennedy A.R. The thermal stability of TiC particles in an Al7wt.%Si alloy. *Materials Science and Engineering*. 2003;A356:316–325.  
[https://doi.org/10.1016/S0921-5093\(03\)00143-6](https://doi.org/10.1016/S0921-5093(03)00143-6)
  23. Xia F., Liangc M.X., Gaoc X.S., Guo Y.C., Li J.P., Yang W., Zhang Z.K. Instability of in situ TiC particles in an Al–12Si alloy. *Journal of Materials Research and Technology*. 2020;9(5):11361–11369.  
<https://doi.org/10.1016/j.jmrt.2020.07.063>
  24. Ding Hai-min, Liu Xiang-fa. Influence of Si on stability of TiC in Al melts. *Transactions of Nonferrous Metals Society of China*. 2011;21:1465–1472.  
[https://doi.org/10.1016/S1003-6326\(11\)60882-0](https://doi.org/10.1016/S1003-6326(11)60882-0)
  25. Tang P., Zhou Y., Lai J. Lin Y., Lv S., Deng S. Preparation, Microstructure and mechanical properties of in-situ TiC/Al–Si–Fe aluminum matrix composites. *Transactions of the Indian Institute of Metals*. 2023;76:1893–1903. <https://doi.org/10.1007/s12666-023-02885-6>
  26. Anilkumar V., Shankar K.V., Balachandran M., Joseph J., Nived S., Jayanandan J., Jayagopan J., Surya Balaji U.S. Impact of heat treatment analysis on the wear behaviour of Al–14.2Si–0.3Mg–TiC composite using response surface methodology. *Tribology in Industry*. 2021;43(4):590–602.  
<https://doi.org/10.24874/ti.988.10.20.04>
  27. Chen Ch.-L., Lin Ch.-H. A study on the aging behavior of Al6061 composites reinforced with Y<sub>2</sub>O<sub>3</sub> and TiC. *Metals*. 2017;7(11). <https://doi.org/10.3390/met7010011>
  28. Shuaihang Pan, Jie Yuan, Kaiyuan Jin, Narayanan Murali, Aaron Gladstein, Yuxin Zeng, Alan Taub, Xiaochun Li. Influence of Mg on reaction and properties

- of Al–Si/TiC nanocomposites. *Materials Science and Engineering*. 2022;A840:142992.  
<https://doi.org/10.1016/j.msea.2022.142992>
29. Pan S., Jin K., Wang T., Zhang Z., Zheng L., Umehara N. Metal matrix nanocomposites in tribology: Manufacturing, performance, and mechanisms. *Friction*. 2022;10:1596–1634.  
<https://doi.org/10.1007/s40544-021-0572-7>
  30. Prusov E.S., Deev V.B., Aborkin A.V., Ri E.K., Rakhuba E.M. Structural and morphological characteristics of the friction surfaces of in-situ cast aluminum matrix composites. *Journal of Surface Investigation*. 2021;15(6):1332–1337.  
<https://doi.org/10.1134/S1027451021060410>
  31. Sherina Yu.V., Luts A.R., Ibatullin I.D. Development of a composite material based on the AK10M2N alloy and study of its tribological properties. *Naukoymkiye tekhnologii v mashinostroyenii*. 2022;2(128):11–16. (In Russ.).  
<https://doi.org/10.30987/2223-4608-2022-2-11-16>  
Шерина Ю.В., Луц А.Р., Ибатуллин И.Д. Разработка композиционного материала на основе сплава АК10М2Н и исследование его триботехнических свойств. *Научные технологии в машиностроении*. 2022;2(128):11–16.  
<https://doi.org/10.30987/2223-4608-2022-2-11-16>
  32. Арзамасов Б.Н., Сидорин И.И., Косолапов Г.Ф., Макарова В.И., Мухин Г.Г., Рыжов Н.М., Силаева В.И., Ульянова В.И. *Материаловедение*. М.: Машиностроение, 1986. 384 с.  
Arzamasov B.N., Sidoren I.I., Kosolapov G.F., Makarova V.I., Mukhin G.G., Ryzhov N.M., Silaeva V.I., Ulyanova V.I. *Material science*. Moscow: Mashinostroyeniye, 1986. 384 p. (In Russ.).
  33. Muratov V.S. Directed formation of the structural state of cast billets from aluminum alloys. Part 1. The influence of crystallization cooling on the structure and properties of cast billets. *Zagotovitel'nyye proizvodstva v mashinostroyenii*. 2003;5:3–8. (In Russ.).  
Муратов В.С. Направленное формирование структурного состояния литых заготовок из алюминиевых сплавов. Часть 1. Влияние кристаллизационного охлаждения на структуру и свойства литых заготовок. *Заготовительные производства в машиностроении*. 2003;5:3–8.
  34. Man Zhu, Zengyun Jian, Gencang Yang, Yaohe Zhou. Effects of T6 heat treatment on the microstructure, tensile properties, and fracture behavior of the modified A356 alloys. *Materials and Design*. 2012;36:243–249.  
<https://doi.org/10.1016/j.matdes.2011.11.018>
  35. Nikitin K.V., Nikitin V.I., Timoshkin I.Yu. The influence of modifiers on the change in the mechanical properties of silumins. *Izvestiya. Non-Ferrous Metallurgy*. 2017;3:72–76. (In Russ.).  
<https://dx.doi.org/10.17073/0021-3438-2017-3-72-76>  
Никитин К.В., Никитин В.И., Тимошкин И.Ю. Влияние модификаторов на изменение механических свойств силуминов. *Известия вузов. Цветная металлургия*. 2017; 3:72–76.  
<https://dx.doi.org/10.17073/0021-3438-2017-3-72-76>
  36. Nikitin K.V., Nikitin V.I., Kripovalov D.S. Modification of AK10M2N piston alloy with fine-crystalline alloys and remelting. *Liteyshchik Rossii*. 2013;10:28–31. (In Russ.).  
Никитин К.В., Никитин В.И., Кривопапов Д.С. Модифицирование поршневого сплава АК10М2Н мелкокристаллическими лигатурами и переплавами. *Литейщик России*. 2013;10:28–31.
  37. Nyafkin A.N., Shavnev A.A., Kurbatkina E.I., Kosolapov D.V. Study of the influence of silicon carbide particle size on the temperature coefficient of linear expansion of a composite material based on an aluminum alloy. *Trudy VIAM*. 2020;86:41–49. (In Russ.).  
<https://dx.doi.org/10.18577/2307-6046-2020-0-2-41-49>  
Няфкин А.Н., Шавнев А.А., Курбаткина Е.И., Косолапов Д.В. Исследование влияния размера частиц карбида кремния на температурный коэффициент линейного расширения композиционного материала на основе алюминиевого сплава. *Труды ВИАМ*. 2020;86:41–49.  
<https://dx.doi.org/10.18577/2307-6046-2020-0-2-41-49>
  38. Perelygin Yu. P., Los I. S., Kireev Yu. S. Corrosion and protection of metals from corrosion. Penza: PGU, 2015. 88 p. URL: <https://elib.pnzgu.ru/files/eb/u36mWX4yGz0I.pdf> (accessed: 19.01.2024). (In Russ.).  
Перельгин Ю. П., Лось И.С., Киреев С.Ю. Коррозия и защита металлов от коррозии. Пенза: Изд-во ПГУ, 2015. 88 с. URL: <https://elib.pnzgu.ru/files/eb/u36mWX4yGz0I.pdf> (дата обращения: 19.01.2024).

## Information about the authors

**Alfiya R. Luts** – Cand. Sci. (Eng.), Assistant Prof. of the Department of Metal Science, Powder Metallurgy, Nanomaterials (MPMN), Samara State Technical University (SamSTU).  
<http://orcid.org/0000-0001-7889-9931>  
 E-mail: alya\_luts@mail.ru

**Yuliya V. Sherina** – Postgraduate Student of the Department of MPMN, SamSTU.  
<http://orcid.org/0000-0002-5451-7107>  
 E-mail: yulya.makhonina.97@inbox.ru

**Aleksandr P. Amosov** – Dr. Sci. (Phys.-Math.), Head of the Department of MPMN, SamSTU.  
<http://orcid.org/0000-0003-1994-5672>  
 E-mail: egundor@yandex.ru

**Evgeniy A. Minakov** – Leading Engineer of the Department of Foundry and High-Efficiency Technologies, SamSTU.  
<http://orcid.org/0009-0003-1690-774X>  
 E-mail: tlp@samgtu.ru

**Ildar D. Ibatullin** – Dr. Sci. (Eng.), Head of the Department of Machinery and Equipment for Oil, Gas and Chemical Production, SamSTU.  
<http://orcid.org/0000-0002-6111-0487>  
 E-mail: mahp@samgtu.ru

## Информация об авторах

**Альфия Расимовна Луц** – к.т.н., доцент кафедры «Металловедение, порошковая металлургия, наноматериалы» (МПМН), Самарский государственный технический университет (СамГТУ).  
<http://orcid.org/0000-0001-7889-9931>  
 E-mail: alya\_luts@mail.ru

**Юлия Владимировна Шерина** – аспирант кафедры МПМН, СамГТУ.  
<http://orcid.org/0000-0002-5451-7107>  
 E-mail: yulya.makhonina.97@inbox.ru

**Александр Петрович Амосов** – д.ф.-м.н., профессор, зав. кафедрой МПМН, СамГТУ.  
<http://orcid.org/0000-0003-1994-5672>  
 E-mail: egundor@yandex.ru

**Евгений Александрович Минаков** – вед. инженер кафедры «Литейные и высокоэффективные технологии», СамГТУ.  
<http://orcid.org/0009-0003-1690-774X>  
 E-mail: tlp@samgtu.ru

**Ильдар Дугласович Ибатуллин** – д.т.н., профессор, зав. кафедрой «Машины и оборудование нефтегазовых и химических производств», СамГТУ.  
<http://orcid.org/0000-0002-6111-0487>  
 E-mail: mahp@samgtu.ru

## Contribution of the authors

**A.R. Luts** – formulating the main concept, purpose and objectives of the study, analyzing the results, writing the text.

**Yu.V. Sherina** – conducting heat treatment and tests of the samples, analyzing the results, writing the text.

**A.P. Amosov** – scientific supervision, correcting the text and conclusions.

**E.A. Minakov** – conducting tests to determine the coefficient of thermal linear expansion, drawing conclusions.

**I.D. Ibatullin** – conducting tribological tests, drawing conclusions.

## Вклад авторов

**А.Р. Луц** – формирование основной концепции, постановка цели и задачи исследования, анализ результатов, подготовка текста статьи.

**Ю.В. Шерина** – проведение термической обработки и испытаний образцов, анализ результатов, подготовка текста статьи.

**А.П. Амосов** – научное руководство, корректировка текста, корректировка выводов.

**Е.А. Минаков** – проведение испытаний по определению коэффициента термического линейного расширения, формулировка выводов.

**И.Д. Ибатуллин** – проведение трибологических испытаний, формулировка выводов.

*The article was submitted 02.02.2024, revised 11.03.2024, accepted for publication 18.03.2024*

*Статья поступила в редакцию 02.02.2024, доработана 11.03.2024, подписана в печать 18.03.2024*

UDC 621.763 + 621.762.24

<https://doi.org/10.17073/0021-3438-2024-2-44-54>

Research article

Научная статья



## Synthesis and study of the properties of zirconium dioxide powders with different yttrium content

S.V. Buinachev<sup>1,2</sup>, M.A. Domashenkov<sup>1,2</sup>, M.A. Mashkovtsev<sup>2</sup>, D.O. Polivoda<sup>2</sup>, N.V. Zhirenkina<sup>1</sup>

<sup>1</sup> Ural Federal University named after the first President of Russia B.N. Yeltsin  
19 Mira Str., Yekaterinburg, Sverdlovsk region 620002, Russia

<sup>2</sup> Institute of High-Temperature Electrochemistry of the Ural Branch of the Russian Academy of Sciences  
20 Akademicheskaya Str., Yekaterinburg 620066, Russia

✉ Maksim A. Domashenkov (maks84155@gmail.com)

**Abstract:** As part of the study, the influence of yttrium content on the properties of particles during controlled precipitation and after thermal treatment was investigated. Precipitation was carried out at a constant pH of 5 from nitric acid solutions, where the concentration of zirconium was 1 mole/dm<sup>3</sup> and the yttrium content ranged from 0 to 30 % based on their oxides. The drying and calcination temperatures of the precipitates were 40 °C and 1000 °C, respectively. It was shown that with a yttrium content of up to 15 %, there was a consistent increase in the average diameter of zirconium hydroxide particles during deposition. When the yttrium concentration was increased to 30 %, the average particle size increased during the first 10 minutes of deposition, followed by a gradual decrease. The largest particle diameter was observed in the specimen with 7 % yttrium. In all cases, the formation of spherical aggregates was observed. With an increasing yttrium content, the boundaries between particles became smoother, and the degree of co-deposition of yttrium during synthesis decreased from 80 % to 60 %. Depending on the yttrium concentration, different modifications of stabilized zirconium dioxide powders were obtained: tetragonal ZrO<sub>2</sub> for 2–7 % yttrium, and cubic ZrO<sub>2</sub> for 15–30 % yttrium. Therefore, the results obtained during the study can be useful for the development of technology for the production of powdered materials for various applications.

**Key words:** stabilized zirconium dioxide, deposition, aggregation, thermal barrier coatings.

**For citation:** Buinachev S.V., Domashenkov M.A., Mashkovtsev M.A., Polivoda D.O., Zhirenkina N.V. Synthesis and study of the properties of zirconium dioxide powders with different yttrium content. *Izvestiya. Non-Ferrous Metallurgy*. 2024;30(2):44–54.

<https://doi.org/10.17073/0021-3438-2024-2-44-54>

## Синтез и исследование свойств порошков диоксида циркония с различным содержанием иттрия

С.В. Буйначев<sup>1,2</sup>, М.А. Домашенков<sup>1,2</sup>, М.А. Машковцев<sup>2</sup>, Д.О. Поливода<sup>2</sup>, Н.В. Жиренкина<sup>1</sup>

<sup>1</sup> Уральский федеральный университет имени первого Президента России Б.Н. Ельцина  
Россия, 620002, Свердловская обл., г. Екатеринбург, ул. Мира, 19

<sup>2</sup> Институт высокотемпературной электрохимии УрО РАН  
Россия, 620066, Свердловская обл., г. Екатеринбург, ул. Академическая, 20

✉ Максим Александрович Домашенков (maks84155@gmail.com)

**Аннотация:** В рамках работы проведено изучение влияния содержания иттрия на изменение свойств частиц как в ходе контролируемого осаждения, так и после термообработки. Осаждение проводили при постоянном значении pH = 5 из азотно-кис-

лых растворов, где концентрация циркония составляла 1 моль/дм<sup>3</sup>, а содержание иттрия – от 0 до 30 % в пересчете на их оксиды. Температуры сушки и обжига осадков составляли 40 и 1000 °С соответственно. Показано, что при содержании Y вплоть до 15 % происходит постоянное увеличение среднего диаметра частиц гидроксида циркония в процессе осаждения, при повышении концентрации Y до 30 % средний размер частиц возрастает в течение первых 10 мин осаждения, после чего происходит его плавное снижение. Наибольший диаметр частиц наблюдался у образца с 7 % Y. Во всех случаях отмечено формирование сферидальных агрегатов. При этом с повышением содержания Y происходят сглаживание границ между частицами и снижение степени соосаждения Y в процессе синтеза с 80 до 60 %. В зависимости от концентрации иттрия получены различные модификации порошков стабилизированного диоксида циркония: при 2–7 % Y – тетрагональный ZrO<sub>2</sub>, а при 15–30 % Y – кубический ZrO<sub>2</sub>. Таким образом, полученные в ходе исследований результаты могут быть полезны для разработки технологии производства порошковых материалов для различного применения.

**Ключевые слова:** стабилизированный диоксид циркония, осаждение, агрегация, термобарьерные покрытия.

**Для цитирования:** Буйначев С.В., Домашенков М.А., Машковцев М.А., Поливода Д.О., Жиренкина Н.В. Синтез и исследование свойств порошков диоксида циркония с различным содержанием иттрия. *Известия вузов. Цветная металлургия*. 2024;30(2):44–54. <https://doi.org/10.17073/0021-3438-2024-2-44-54>

## Introduction

Stabilized zirconium dioxide is used in many industrial fields, including the creation of thermal barrier coatings [1–3], the manufacturing of ceramic products for medical applications [4–6], and the production of solid oxide electrolytes for electrochemical devices [7–9]. It has low thermal conductivity [10], high chemical and corrosion resistance [11], good oxygen conductivity, and biological compatibility with human tissues [12].

To generate thermal barrier coatings on gas turbine engine components, the atmospheric plasma spraying (APS) method is often used, utilizing yttria-stabilized zirconia (YSZ) powders [13–15]. YSZ powder should have high bulk density, low specific surface area, spheroidal particle shape ranging from 20 to 100 μm, and high flowability [16]. Coatings obtained using APS technology reduce part erosion rates and increase adhesion and corrosion resistance during thermal cycling at high temperatures [17].

YSZ powders are also used in the production of ingots for vacuum electron beam evaporation [18]. These ingots are used to form columnar-structured thermal barrier coatings on gas turbine engine blades [19–21]. Compared to APS coatings, columnar coatings have higher adhesion resistance, lower elastic modulus, and surface roughness [22].

Common methods for obtaining stabilized zirconium dioxide in industry include direct and reverse precipitation of zirconium hydroxides [23], the sol-gel process [24], and spray pyrolysis [25]. However, all these methods do not allow for the control of the properties of precipitates and, therefore, the final powder materials. It is known that when using precipitation methods, the properties of hydroxide precipitates strongly depend on pH [26].

Direct and reverse precipitation usually result in fragmented particle shapes and wide size distribution. The sol-gel method is often used to synthesize fine-dispersed powders using organic binders and solvents, which complicates the technology and scaling process. Spray pyrolysis can produce particles with a spheroidal shape ranging from several nanometers to several micrometers. However, obtaining coarse particles with a diameter of 20 to 100 μm is practically impossible. The method is quite complex in technical implementation, requiring high temperatures and posing scaling challenges.

Authors [27] have shown that by varying the pH value during controlled precipitation, it is possible to obtain zirconium hydroxide with different properties, such as average particle diameter and shape, specific surface area, and porosity. It has also been found that the addition of yttrium during this process leads to further modification of these properties.

Thus, precipitation under controlled conditions can be a promising method for synthesizing hydroxide materials with required properties for use in various industrial fields.

In this study, the influence of yttrium content during controlled precipitation at a constant pH of 5 on the properties of zirconium and yttrium hydroxide precipitates, as well as the resulting powders after thermal treatment, was investigated. Specimens of zirconium oxide with yttrium content up to 30 % were obtained. An analysis of particle size distribution and shape was performed during precipitation and after annealing. The degree of yttrium co-precipitation and the phase composition of the powders after annealing were also studied.

## Materials and methods

The synthesis of zirconium hydroxide with varying yttrium content was carried out by the controlled precipitation method at a constant pH of 5. The initial solutions of zirconium and yttrium nitrates were prepared by dissolving zirconium carbonate and yttrium oxide in nitric acid. A 10 % ammonia solution was used as the precipitant. Before each precipitation, a solution containing 123 g of zirconium in terms of oxide and the calculated amount of yttrium to achieve concentrations of 0, 2, 4, 7, 15, and 30 % in terms of oxide in the final powder (referred to as specimens 0%Y, 2%Y, 4%Y, 7%Y, 15%Y, and 30%Y, respectively) was prepared.

The precipitation was carried out in a 3-liter glass beaker with constant stirring using an overhead stirrer. The combined solution of zirconium and yttrium nitrates was dosed into the reactor using a peristaltic pump at a rate of 5 mL/min. The precipitant solution was introduced using another peristaltic pump, which was connected to a pH meter through a relay control system to control the dosing of ammonia and maintain constant pH. The precipitation process was carried out for 200 minutes, after which yttrium was further precipitated by raising the pH to 8 for specimens with yttrium addition. The suspension was then filtered using a vacuum Buchner filter, dried at 40 °C for 24 h, and fired at 1000 °C.

The average particle diameter and their size distribution were determined using laser diffraction on an Analysette 22 instrument (“Fritch”, Germany) in the measurement range of 0.08 to 2000  $\mu\text{m}$  using green and infrared lasers. Suspension specimens were taken from the reactor at different stages during the precipitation for this purpose. The particle shape was evaluated using an optical microscope GX71 (“OLYMPUS”, Japan). The yttrium concentration in the mother solution was determined by complexometric titration using Trilon B. X-ray diffraction patterns of the specimens were obtained using an X’Pert Pro MPD diffractometer (“PANalytical B.V.”, Netherlands) with a solid-state pixel detector in  $\text{CuK}\alpha$  radiation with a  $\beta$ -filter. The phase composition and lattice parameters were determined by full-profile Rietveld analysis, and the areas of coherent scattering (ACS) were determined using the Scherrer method based on the most intense reflections at small scattering angles (shape factor  $K = 0.9$ ) using the X’Pert High Score Plus software (Netherlands).

## Results and discussion

Figure 1 shows the change in average particle diameter ( $d$ ) and size dispersion as a function of precipita-

tion duration ( $\tau$ ). It is shown that in the 0%Y specimen, the value of  $d$  increased starting from the 5<sup>th</sup> minute of the precipitation process and reached 33  $\mu\text{m}$  by the 200<sup>th</sup> minute. The addition of 2 % and 4 % yttrium led to a significant increase in this parameter throughout the precipitation process, reaching 38  $\mu\text{m}$  by the 200<sup>th</sup> minute. In the 7%Y specimen, an even greater increase in particle size was observed, reaching 40  $\mu\text{m}$  by the end of the deposition. Adding 15% Y resulted in a substantial increase in the average particle diameter to 39  $\mu\text{m}$  during the first 100 minutes of deposition, after which it remained almost unchanged. For the 30%Y specimen, a sharp increase in the value of  $d$  was recorded by the 20<sup>th</sup> minute of deposition, reaching 28  $\mu\text{m}$ , after which it gradually decreased to 23  $\mu\text{m}$  by the completion of the process.

The size dispersion parameter for the 0%Y specimen decreased throughout the precipitation process, reaching 1.08 by the 200<sup>th</sup> minute. For specimens with yttrium content ranging from 2 % to 15 %, the values of this parameter decreased by the 70<sup>th</sup> minute of deposition, after which they started to increase, ending the process in the range of 1.2 to 1.28. For the 30%Y specimen, the size dispersion value was consistently higher throughout the precipitation compared to the other specimens, reaching 1.3 by the 200<sup>th</sup> minute.

Figure 2 illustrates the mass size distribution of particles as a function of precipitation time and yttrium addition. For specimens with yttrium content ranging from 0 to 15 %, a peak in the range of  $\tau = 15\div 20 \mu\text{m}$  with an arm in the range of  $d = 1\div 5 \mu\text{m}$  formed during the first 10 minutes of deposition. As the precipitation time increases, this peak disappears, and a peak at  $d \sim 1 \mu\text{m}$  with a mass fraction of less than 1 % emerges. Simultaneously, the main peak shifts uniformly towards larger sizes, indicating an increase in the average particle diameter. The peak at  $d \sim 1 \mu\text{m}$  remains relatively unchanged in its position. For the 30%Y specimen, a peak in the range of  $d \sim 30 \mu\text{m}$  with an arm in the range of  $d = 1\div 5 \mu\text{m}$  is formed by the 10<sup>th</sup> minute of deposition. With increasing precipitation time, the main peak shifts towards smaller sizes, and the arm transforms into a separate peak with a maximum in the range of  $d = 1\div 2 \mu\text{m}$ .

It is likely that the formation of two populations of particles during precipitation leads to an increase in their average diameter due to layer-by-layer aggregation. Apparently, conducting hydrolysis at constant pH results in the formation of similarly charged primary nuclei, which aggregate upon collision to form larger particles,

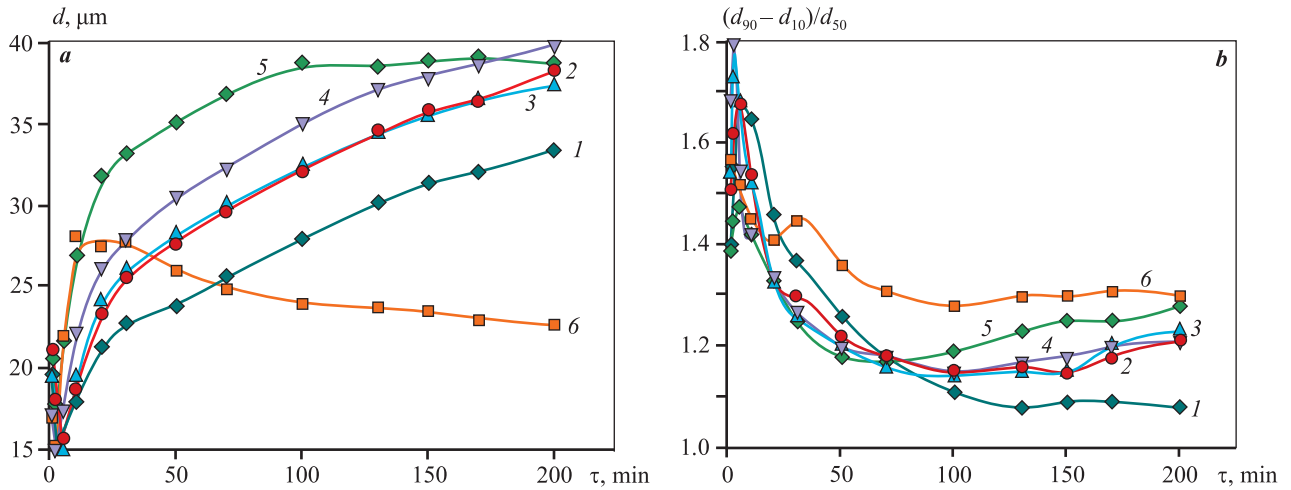


**Fig. 1.** Average particle size (a) and dispersion of sizes (b) as a function of precipitation duration

1 – sample 0%Y; 2 – 2%Y; 3 – 4%Y; 4 – 7%Y; 5 – 15%Y; 6 – 30%Y

**Рис. 1.** Изменение среднего диаметра частиц (a) и дисперсии размеров (b) в зависимости от длительности осаждения

1 – образец 0%Y; 2 – 2%Y; 3 – 4%Y; 4 – 7%Y; 5 – 15%Y; 6 – 30%Y

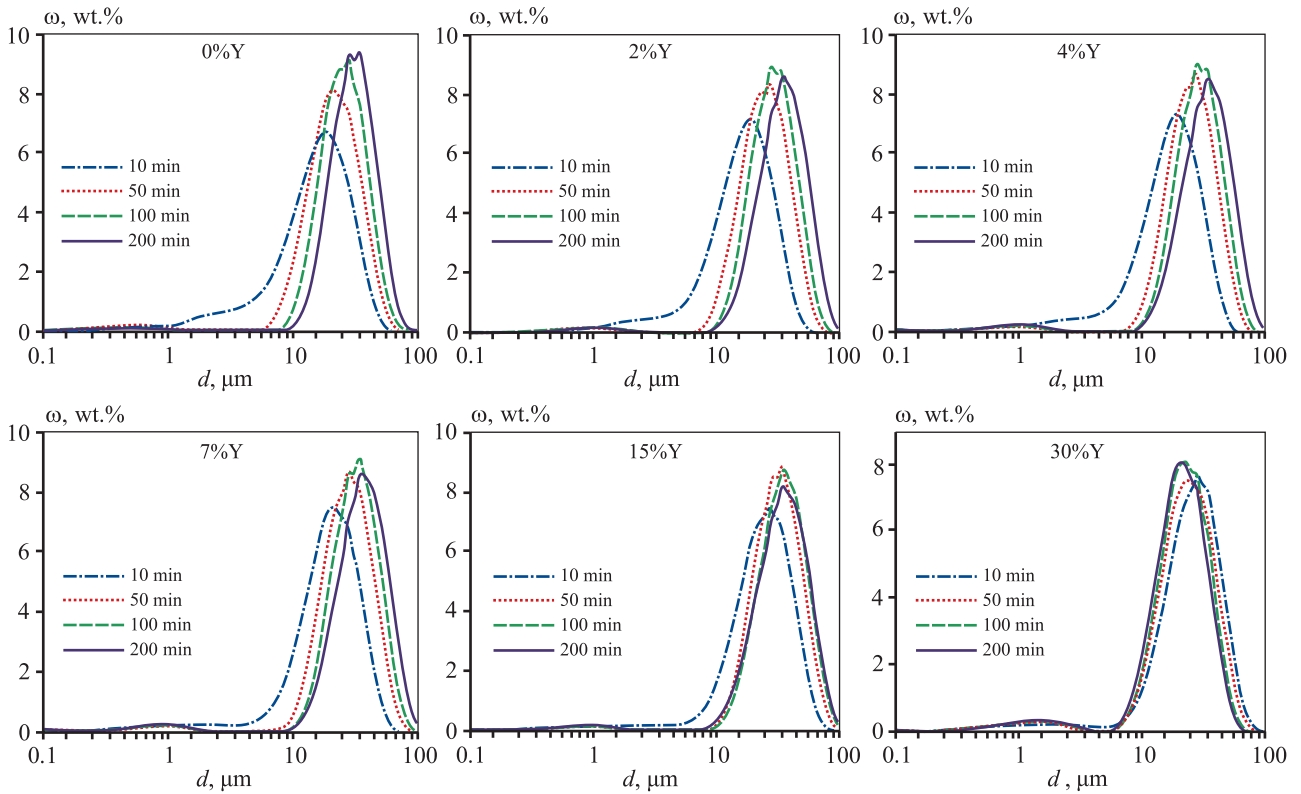


**Fig. 2.** Mass distribution of particle sizes as a function of precipitation duration

**Рис. 2.** Массовое распределение частиц по размерам в зависимости от длительности осаждения исследуемых образцов

followed by a change in charge on the surface due to olation processes.

Thus, the simultaneous occurrence of nucleation with one charge and the appearance of larger particles

with the opposite charge serve as the basis for the mechanism of aggregation processes. The addition of yttrium during precipitation appears to significantly affect the progress of olation and oxolation processes. It can

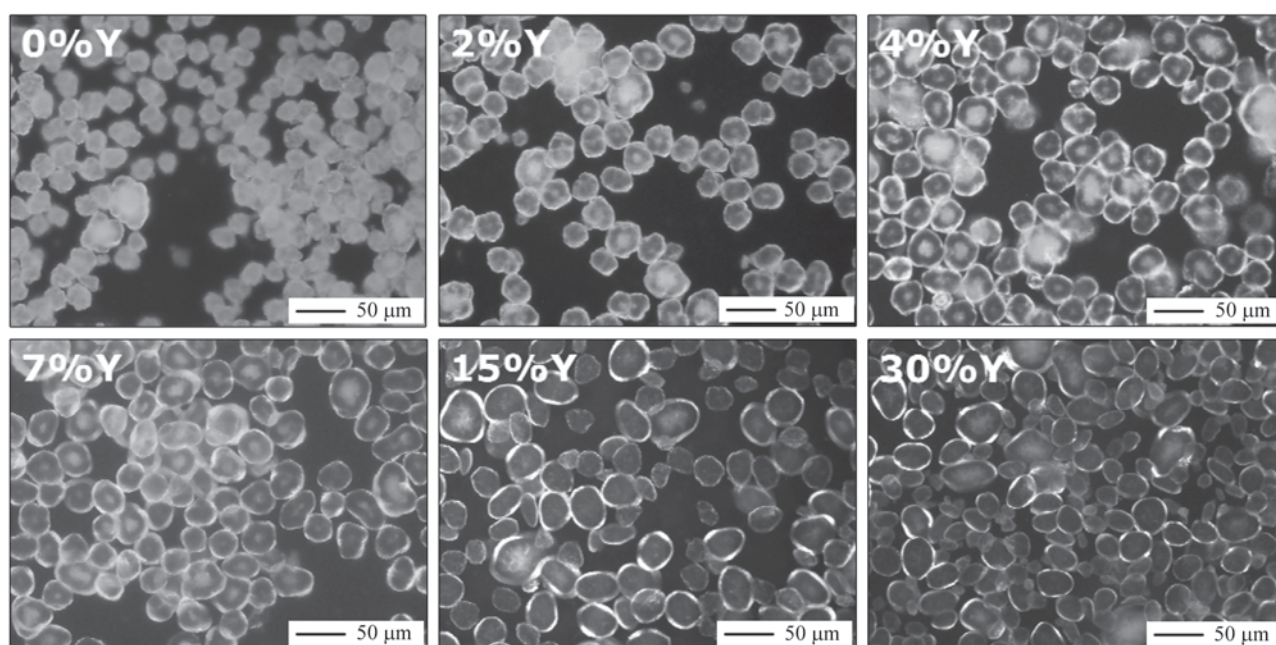
be assumed that its presence leads to an increase in the surface charge of primary particles, which hinders their aggregation with each other. These nuclei predominantly begin to accumulate on the formed large aggregates with the opposite charge, resulting in a significant increase in the average particle diameter when yttrium is added. However, at a yttrium content of 30 %, the layer-by-layer aggregation process is hindered, and the large aggregates stop increasing in size, leading to an increase in the fraction of small particles. Presumably, the high yttrium content almost completely suppresses the flocculation processes and neutralizes the charge on the surface of large aggregates, resulting in an increase in the size of particles in those aggregates where the charge has not yet been neutralized.

Figure 3 illustrates optical images of particles at the 200<sup>th</sup> minute of sedimentation for specimens with different yttrium content. It is shown that in the specimen without the addition of Y, the formation of spheroidal aggregates with well-defined but rough boundaries occurs. A gradual increase in yttrium content leads to the formation of spheroidal aggregates with smoother boundaries. It has been found that the introduction of yttrium up to 15 % results in an increase in particle and aggregate sizes, while increasing its content to 30 % leads to a decrease, which is consistent with laser diffraction results.

The influence of yttrium addition on the shape of particles can be explained by the same approach used in the analysis of particle size changes, based on the difference in their charges. As mentioned earlier, the addition of yttrium hinders aggregation of primary particles, leading primarily to increased collisions between very small primary particles and larger ones, thereby contributing to the formation of smooth boundaries on the surface.

Figure 4 shows the change in the concentration of yttrium cations ( $Y^{3+}$ ) in the suspension during precipitation and the rate of co-precipitation of yttrium with zirconium hydroxide as a function of process time. It is shown that for specimens with 2%Y, 4%Y, 7%Y, and 15%Y, there is a gradual increase in  $Y^{3+}$  concentration with increasing sedimentation time, reaching 0.3, 3.0, 5.5, and 15 g/dm<sup>3</sup>, respectively, by the end of the process. For the 30%Y specimen, there is a sharp increase in  $Y^{3+}$  content to 60 g/dm<sup>3</sup> by the 100<sup>th</sup> minute of the process, after which it remains nearly constant. At the same time, the rate of yttrium co-precipitation with zirconium hydroxide reaches 80 % by the 200<sup>th</sup> minute for the 2%Y, 4%Y, and 7%Y specimens, and 72 % and 60 % for the 15%Y and 30%Y specimens, respectively.

Thus, despite the low pH value of the sedimentation process, a significant portion of yttrium is captured by the zirconium hydroxide precipitate. This is likely due to



**Fig. 3.** Optical images of particles of the investigated specimens by the 200<sup>th</sup> minute of deposition

**Рис. 3.** Оптические изображения частиц исследуемых образцов к 200-й минуте осаждения

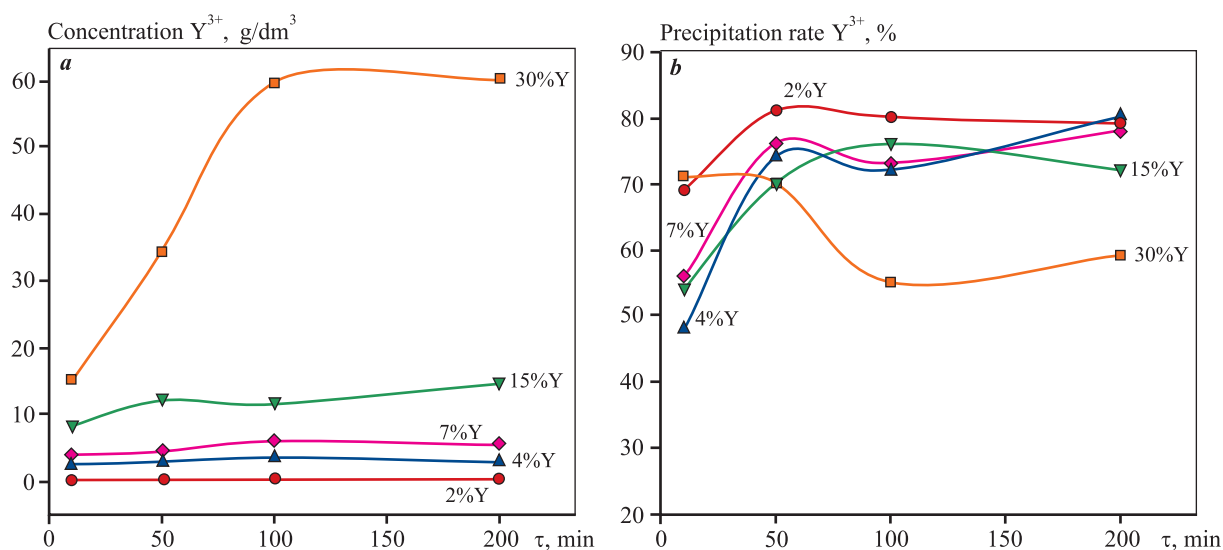


**Fig. 4.** Concentration (a) and co-deposition rate (b) of yttrium cations in slurry as a function of precipitation duration

**Рис. 4.** Изменение концентрации (a) и степени соосаждения (b) катионов иттрия в суспензии в зависимости от длительности осаждения

the high (excessive) concentration of  $OH^-$  groups on the surface of the hydroxide, which bind to the  $Zr^{4+}$  cations during the formation of zirconium hydroxide.

Figure 5 shows the change in the average particle diameter and size dispersion as a function of the synthesis stage for the specimens. It is shown that the values of  $d$  decrease stepwise after drying at  $t = 40^\circ C$  and annealing at  $1000^\circ C$ . After annealing, the average particle size for the 0%Y specimen was  $22\ \mu m$ , for the 2%Y–15%Y specimens it remained at around  $25\ \mu m$ , and for the 30%Y specimen it was  $17\ \mu m$ . The size dispersion values after annealing for specimens with yttrium content up to 15 % are practically at the same level, around 1.1, and for the 30%Y specimen they are around 1.4.

Figure 6 illustrates the particle size distribution as a function of the stage of specimen synthesis. For specimens with yttrium content up to 15 %, after annealing at  $1000^\circ C$ , a narrow, high peak is observed, which, compared to the suspension and drying stages, has significantly shifted to the left, indicating smaller particle sizes. At the same time, the shape of the peak has not changed significantly, suggesting that neither destruction nor additional aggregation occurs during heat treatment. For the specimen with 30 % yttrium, the particle size distribution after annealing looks similar, but the distribution peak is wider and lower compared to the other specimens. This may be due to the fact that even at the precipitation stage, large aggregates hardly changed in size, while a large number of new aggregates were formed.

Figure 7 shows optical images of particles after annealing at  $1000^\circ C$  for specimens with different yttrium contents. It is shown that for all of them, after annealing, the particles retain a spheroidal shape. Specimens with 0%Y, 2%Y, and 4%Y exhibit particles with uneven boundaries, while specimens with 7%Y, 15%Y, and 30%Y display particles with smoother boundaries.

It is known that zirconium dioxide can exist in three different crystalline modifications depending on temperature: monoclinic at room temperature, tetragonal at  $t > 1170^\circ C$ , and cubic at  $t > 2370^\circ C$ . To increase its thermal stability, stabilizing components are introduced, with yttrium oxide being the most common. The similarity of the ionic radii of Zr and Y, as well as the isomorphism of their structures, allows for the formation of a solid solution when Y is introduced into the crystal lattice of  $ZrO_2$ . Stabilization of zirconium dioxide with low-valent cations can lead to the stabilization of the tetragonal or cubic phase at lower temperatures, even at room temperature. This is due to the generation of oxygen vacancies in the lattice, which in turn reduces the stress caused by the energetically unfavorable 8-coordinated configuration [28].

Depending on the yttrium content, three structural modifications of zirconia oxide were obtained after annealing at  $1000^\circ C$ . The data from X-ray phase analysis are presented in Table 1. Zirconium oxide without yttrium addition has a monoclinic structural modification, with a crystallite size of  $48\ nm$ . Specimens with 2 %,

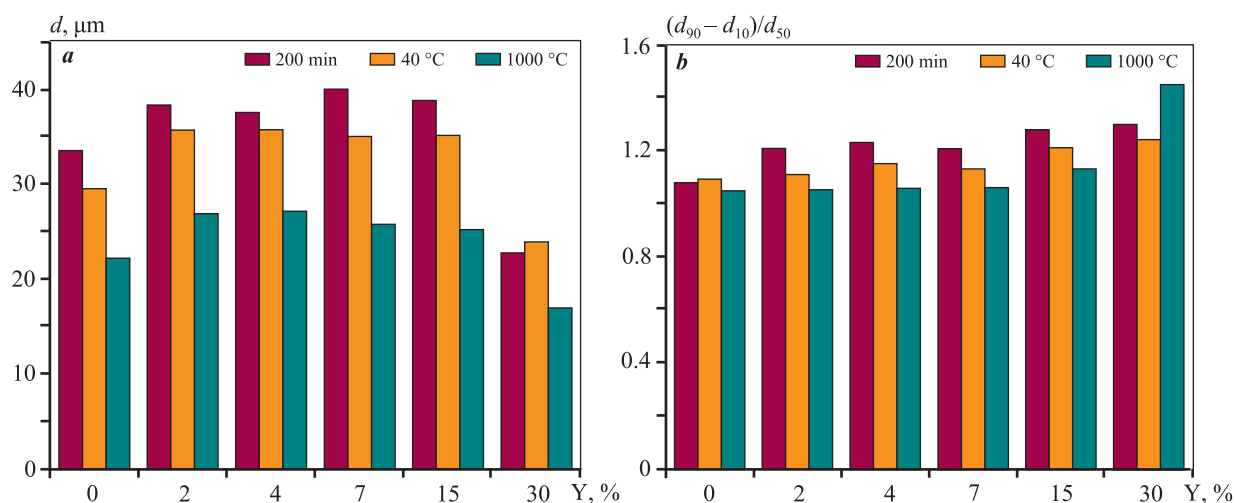


Fig. 5. Average particle size (a) and dispersion of sizes (b) at various stages of synthesis of the considered specimens

Рис. 5. Значения среднего диаметра частиц (a) и дисперсии размеров (b) на разных этапах синтеза исследуемых образцов

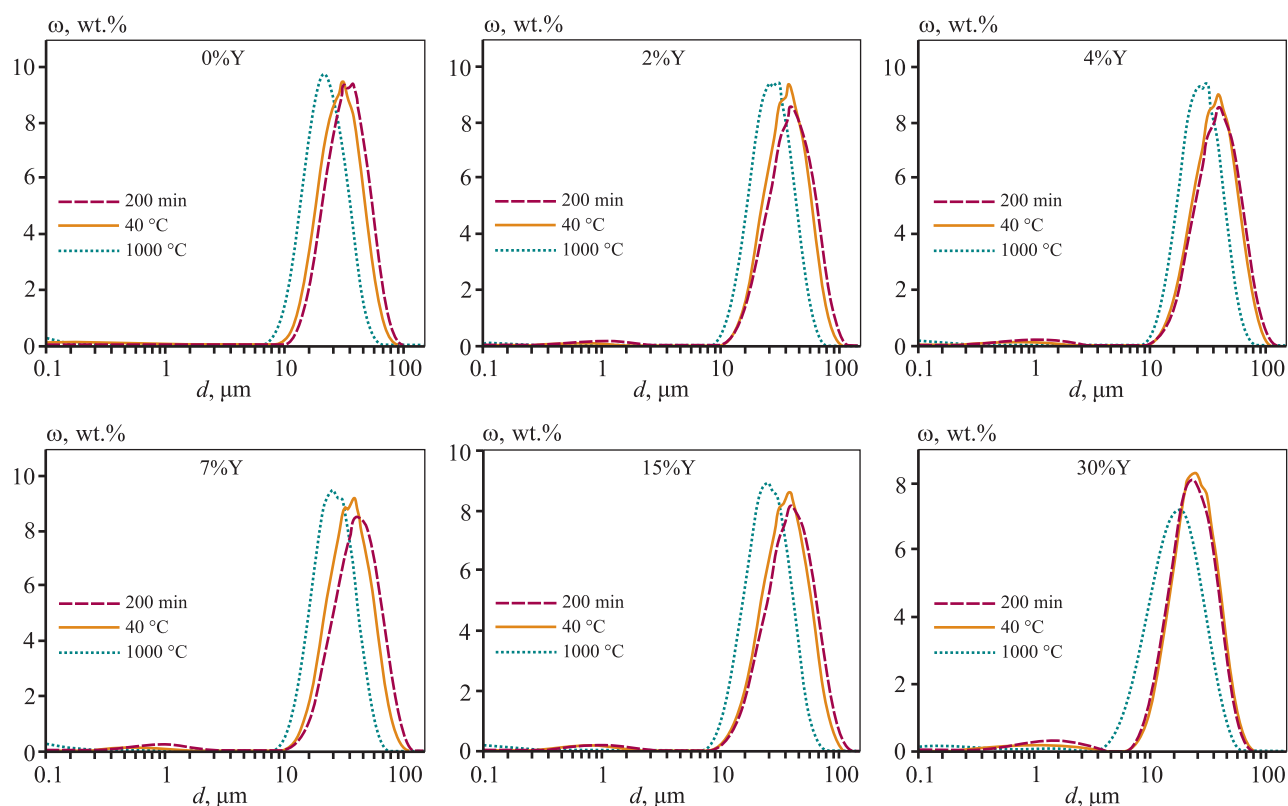


Fig. 6. Particle size distribution at various stages of synthesis of the considered specimens

Рис. 6. Распределение частиц по размерам на разных этапах синтеза исследуемых образцов

4 %, and 7 % Y content are characterized by a tetragonal modification. This is confirmed by the smaller values of edge lengths compared to the monoclinic modification. The crystallite size decreases with increasing yttrium content, which is consistent with literature data [29], and ranges from 40 to 60 nm. At the same

time, zirconium dioxide with 15 % and 30 % Y additions undergoes the formation of a cubic modification, as evidenced by the similar edge length parameters. The crystallite sizes are 28 and 42 nm, respectively. The X-ray diffraction patterns of all yttrium-modified specimens do not show peaks corresponding to pure

**X-ray phase analysis of zirconium dioxide with various content of yttrium**

Результаты рентгенофазового анализа образцов диоксида циркония с различным содержанием иттрия

Specimen	Crystallite size, nm	Modification type	Lattice constants, Å		
			<i>a</i>	<i>b</i>	<i>c</i>
0%Y	48	Monoclinic	5.147	5.202	5.312
2%Y	60	Tetragonal	3.595	3.595	5.175
4%Y	51	Tetragonal	3.603	3.603	5.170
7%Y	42	Tetragonal	3.614	3.614	5.153
15%Y	28	Cubic	5.127	5.127	5.127
30%Y	42	Cubic	5.142	5.142	5.142

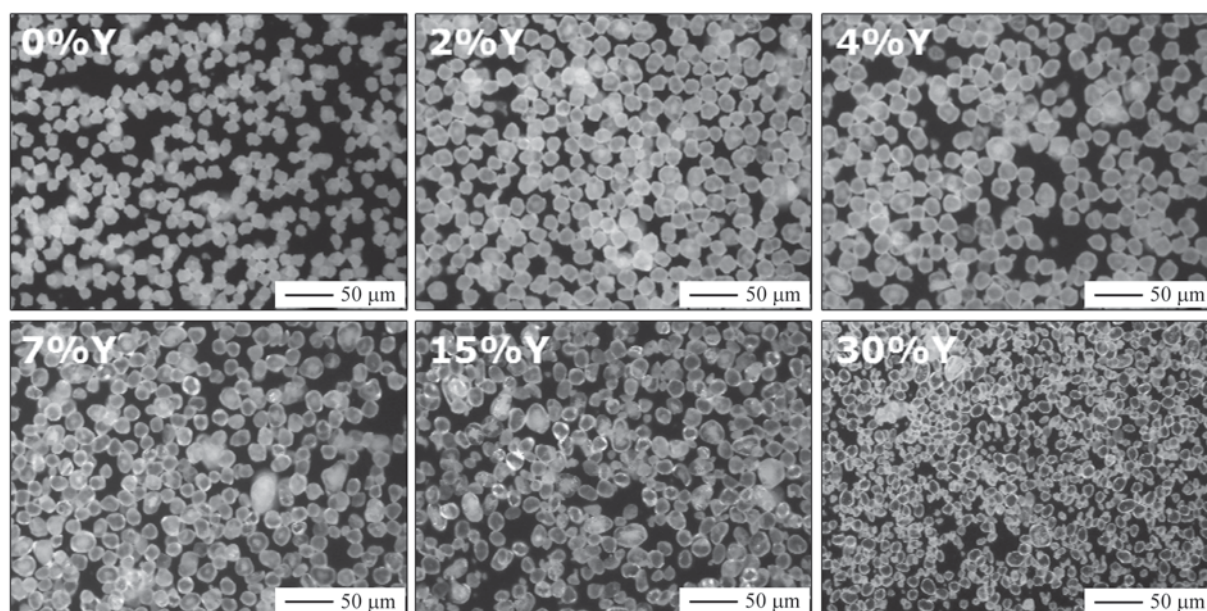


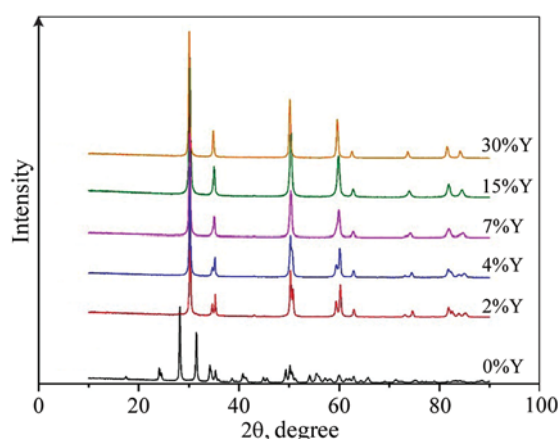
Fig. 7. Optical images of particles after annealing at 1000 °C

Рис. 7. Оптические изображения частиц после обжига при 1000 °C исследуемых образцов

yttrium oxide, indicating that it is uniformly distributed in zirconium dioxide, forming a solid substitution solution.

**Conclusions**

The specimens of zirconium dioxide with varying yttrium content were produced in this study through controlled precipitation at constant pH. The influence of yttrium addition on the average particle diameter, size dispersion, particle size distribution, shape, degree of yttrium deposition, and phase composition of the final powders was investigated. A mechanism for the aggregation of zirconium hydroxide during precipitation at a constant pH value was proposed, and the influence of yttrium addition on this process was examined.

Fig. 8. X-ray patterns of the considered specimens after annealing at  $t = 1000$  °CРис. 8. Рентгенограммы исследуемых образцов после обжига при  $t = 1000$  °C

It was found that the yttrium content significantly influenced the particle size during deposition: in specimens without yttrium, the average particle diameter was 33  $\mu\text{m}$ , while with 7 % yttrium addition, it increased to 40  $\mu\text{m}$ . It was also observed that yttrium co-deposited with zirconium hydroxide at a pH of 5 during the precipitation process, with the degree of yttrium precipitation ranging from 60 % to 80 % depending on its content.

After thermal treatment, there was no destruction or additional aggregation of particles, and the spherical shape of the particles was preserved, with low size dispersion observed in all specimens. Different modifications of zirconium dioxide were obtained depending on the yttrium content: monoclinic for specimens without yttrium, tetragonal for 2–7 % yttrium addition, and cubic for over 15 % yttrium addition.

Therefore, the obtained results can be useful in the development of powder production technology for various industrial applications, particularly for the formation of thermal barrier coatings using atmospheric plasma spraying.

## References

1. Qiaomu L., Shunzhou H., Aijie H. Composite ceramics thermal barrier coatings of yttria stabilized zirconia for aero-engines. *Journal of Materials Science & Technology*. 2019;35(12):2814–2823. <https://doi.org/10.1016/j.jmst.2019.08.003>
2. Liu G., Shen Z., He L., Mu R., Huang G. LaYZrO/YSZ double ceramic layer thermal barrier coatings by EB-PVD: Thermal performance, morphology and failure behavior. *Materialia*. 2023;27:101661. <https://doi.org/10.1016/j.mtla.2022.101661>
3. Erdoğlan N.N., Başıyğit A.B. Investigating thermal shock and corrosion resistance of Inconel 601 super alloy after thermal barrier coating with 8 % YSZ powder. *Materials Today Communications*. 2023;36:106516. <https://doi.org/10.1016/j.mtcomm.2023.106516>
4. Moayedee Y., Nikzad L., Habibzadeh S. Mechanical, electrochemical, and biological properties of YSZ-Mo: A new class of bio-composites. *Materialia*. 2022;24:101515. <https://doi.org/10.1016/j.mtla.2022.101515>
5. Piconi C., Maccauro G. Zirconia as a ceramic biomaterial. *Biomaterials*. 1999;20(1):1–25. [https://doi.org/10.1016/S0142-9612\(98\)00010-6](https://doi.org/10.1016/S0142-9612(98)00010-6)
6. Xiuping Z., Xin W., Jing S. Additive manufacturing of zirconia ceramics: a state-of-the-art review. *Journal of Materials Research and Technology*. 2020;9(4):9029–9048. <https://doi.org/10.1016/j.jmrt.2020.05.131>
7. Xiuan X., Hiroya A., Kazuo K., Ryo H., Anze S., Makio N. Novel Co-precipitation method to synthesize NiO–YSZ nanocomposite powder for solid oxide fuel cell. *Advanced Powder Technology*. 2014;25(2):490–494. <https://doi.org/10.1016/j.apt.2013.08.001>
8. Shao Z., Zhou W., Zhu Z. Advanced synthesis of materials for intermediate-temperature solid oxide fuel cells. *Progress in Materials Science*. 2012;57(4):804–874. <https://doi.org/10.1016/j.pmatsci.2011.08.002>
9. Monaco F., Effori E., Hubert M., Siebert E., Geneste G., Morel B., Djurado E., Montinaro D., Laurencin J. Electrode kinetics of porous Ni–3YSZ cermet operated in fuel cell and electrolysis modes for solid oxide cell application. *Electrochimica Acta*. 2021;389(1):138765. <https://doi.org/10.1016/j.electacta.2021.138765>
10. Jungwan C., Joonsuk P., Jihwan A. Low thermal conductivity of atomic layer deposition yttria-stabilized zirconia (YSZ) thin films for thermal insulation applications. *Journal of the European Ceramic Society*. 2017;37(9):3131–3136. <https://doi.org/10.1016/j.jeurceramsoc.2017.03.045>
11. Raheleh A.-P., Reza S.-R., Reza M., Hossein J. Improving the hot corrosion resistance of plasma sprayed ceria–yttria stabilized zirconia thermal barrier coatings by laser surface treatment. *Materials & Design*. 2014;57:336–341. <https://doi.org/10.1016/j.matdes.2013.12.075>
12. Nikhil A. P., Balasubramanian K. Biological and mechanical enhancement of zirconium dioxide for medical applications. *Ceramics International*. 2020;46(4):4041–4057. <https://doi.org/10.1016/j.ceramint.2019.10.220>
13. Chaoxi S., Jinshuang W., Xianjun L., Tingyang C., Mingyi X., Guang D., Yuancheng R., Zhongwei L., ZhixigD., Yifeng X., Guoqiang L., Yixing Z., Fuhe Y., Xueqiang C. Investigation of corrosion resistance of YSZ coating with sacrificial aluminum oxide protective layer against CMAS and composite corrosives. *Journal of the European Ceramic Society*. 2024;44(4):2537–2579. <https://doi.org/10.1016/j.jeurceramsoc.2023.11.030>
14. Clarke D.R., Phillpot S.R. Thermal barrier coating materials. *Materials Today*. 2005;8(6):22–29. [https://doi.org/10.1016/S1369-7021\(05\)70934-2](https://doi.org/10.1016/S1369-7021(05)70934-2)
15. Padture N.P., Gell M., Jordan E.H. Thermal barrier coatings for gas-turbine engine applications. *Science*. 2002;296(5566):280–284. <https://www.science.org/doi/10.1126/science.1068609>
16. Buinachev S., Mashkovtsev M.A., Zhirenkina N., Aleshin D., Dankova A. A new approach for the synthesis of monodisperse zirconia powders with controlled particle size. *International Journal of Hydrogen Energy*. 2021;46(32):16878–16887. <https://doi.org/10.1016/j.ijhydene.2021.01.134>
17. Yuzhuo L., Zhen Z., Xin W., Rende M., Limin H., Zhenhua X. Thermo-physical properties, morphology and thermal shock behavior of EB-PVD thermal barrier coat-

- ing with DLC YbGdZrO/YSZ system. *Materials Today Communications*. 2023;35:106265.  
<https://doi.org/10.1016/j.mtcomm.2023.106265>
18. He W., Mauer G., Sohn Y.J., Schwedt A., Guillon O., Vaßen R. Investigation on growth mechanisms of columnar structured YSZ coatings in plasma spray-physical vapor deposition (PS-PVD). *Journal of the European Ceramic Society*. 2019;39(10):3129–3138.  
<https://doi.org/10.1016/j.jeurceramsoc.2019.04.003>
  19. Gao L., Guo H., Wei L., Li C., Xu H. Microstructure, thermal conductivity and thermal cycling behavior of thermal barrier coatings prepared by plasma spray physical vapor deposition. *Surface and Coatings Technology*. 2015;276:424–430.  
<https://doi.org/10.1016/j.surfcoat.2015.06.033>
  20. Jude S.A.A., Winowlin Jappes J.T., Adamkhan M. Thermal barrier coatings for high-temperature application on superalloy substrates: A review. *Materials Today: Proceedings*. 2022;60(3):1670–1675.  
<https://doi.org/10.1016/j.matpr.2021.12.223>
  21. Vaßen R., Jarligo M.O., Steinke T., Mack D. E., Stöver D. Overview on advanced thermal barrier coatings. *Surface and Coatings Technology*. 2010;205(4):938–942.  
<https://doi.org/10.1016/j.surfcoat.2010.08.151>
  22. Shan Y., Gao L. Synthesis and characterization of phase controllable ZrO<sub>2</sub>-carbon nanotube nanocomposites. *Nanotechnology*. 2005;16(6):625–630.  
<https://doi.org/10.1088/0957-4484/16/6/001>
  23. Fenech J., Dalbin M., Barnabe A., Bonino J.P., Ansart F. Sol-gel processing and characterization of (RE-Y)-zirconia powders for thermal barrier coatings. *Powder Technology*. 2011;208(2):480–487.  
<https://doi.org/10.1016/j.powtec.2010.08.046>
  24. Chen C.Y., Tseng T.K., Tsai S.C., Lin C.K., Lin H.M. Effect of precursor characteristics on zirconia and ceria particle morphology in spray pyrolysis. *Ceramics International*. 2008;34(2):409–416.  
<https://doi.org/10.1016/j.ceramint.2006.10.013>
  25. Zhang H., Lu H., Zhu Y., Fan L., Duan R., Zhang M., Wang X. Preparations and characterizations of new mesoporous ZrO<sub>2</sub> and Y<sub>2</sub>O<sub>3</sub>-stabilized ZrO<sub>2</sub> spherical powders. *Powder Technology*. 2012;227:9–16.  
<https://doi.org/10.1016/j.powtec.2012.02.007>
  26. Buinachev S., Mashkovtsev M., Dankova A., Zhirenkina N., Kharisova K. Synthesis of YSZ powders with controlled properties by the CDJP method. *Powder Technology*. 2022;399:117201.  
<https://doi.org/10.1016/j.powtec.2022.117201>
  27. Carter G.A., Ogden M.I., Buckley C.E., Maitland C., Paskevicius M. Ammonia-induced precipitation of zirconyl chloride and zirconyl-yttrium chloride solutions under industrially relevant conditions. *Powder Technology*. 2009;188:222–228.  
<https://doi.org/10.1016/j.powtec.2008.04.087>
  28. Trovarelli A., Leitenburg C., Boaro M., Dolcet G. The utilization of ceria in industrial catalysis. *Catalysis Today*. 1999;50: 353–367.  
[https://doi.org/10.1016/S0920-5861\(98\)00515-X](https://doi.org/10.1016/S0920-5861(98)00515-X)
  29. Agarkova E.A., Borik M.A., Bublik V.T., Volkova T.V., Kulebyakin A.V., Kuritsyna I.E., Larina N.A., Lomonova E.E., Milovich F.O., Myzina V.A., Ryabochkina P.A., Tabachkova N.Yu. Effect of the phase composition and local crystal structure on the transport properties of the ZrO<sub>2</sub>-Y<sub>2</sub>O<sub>3</sub> and ZrO<sub>2</sub>-Gd<sub>2</sub>O<sub>3</sub> solid solutions. *Russian Microelectronics*. 2019;48:8:523–530.  
<https://doi.org/10.17073/1609-3577-2018-3-156-165>

## Information about the authors

**Sergei V. Buinachev** – Laboratory Assistant-researcher of the Department of Rare Metals and Nanomaterials, Ural Federal University named after the first President of Russia B.N. Yeltsin (UrFU); Junior Researcher of the Laboratory of Ceramics, Institute of High Temperature Electrochemistry of Ural Branch of the Russian Academy of Sciences (IHTE UB RAS).

<https://orcid.org/0000-0001-7722-9055>

E-mail: s.v.buinachev@urfu.ru

**Maksim A. Domashenkov** – Laboratory Assistant-researcher of the Department of Rare Metals and Nanomaterials, UrFU; Junior Researcher of the Laboratory of Ceramics, IHTE UB RAS.

<https://orcid.org/0009-0003-8882-9373>

E-mail: maks84155@gmail.com

## Информация об авторах

**Сергей Владимирович Буйначев** – лаборант-исследователь кафедры редких металлов и наноматериалов, Уральский федеральный университет имени первого Президента России Б.Н. Ельцина (УрФУ); мл. науч. сотрудник лаборатории керамики, Институт высокотемпературной электрохимии (ИВТЭ) УрО РАН.

<https://orcid.org/0000-0001-7722-9055>

E-mail: s.v.buinachev@urfu.ru

**Максим Александрович Домашенков** – лаборант-исследователь кафедры редких металлов и наноматериалов, УрФУ; мл. науч. сотрудник лаборатории керамики, ИВТЭ УрО РАН.

<https://orcid.org/0009-0003-8882-9373>

E-mail: maks84155@gmail.com

**Maksim A. Mashkovtsev** – Cand. Sci. (Chem.), Researcher of the Laboratory of Electrochemical Devices and Fuel Cells, IHTe UB RAS.

<https://orcid.org/0000-0002-4914-262X>

E-mail: maxftf@yandex.ru

**Dmitry O. Polivoda** – Junior Researcher of the Laboratory of Electrochemical Devices and Fuel Cells, IHTe UB RAS.

<https://orcid.org/0000-0002-3514-9919>

E-mail: sbbthblack@gmail.com

**Nina V. Zhirenkina** – Cand. Sci. (Eng.), Senior Researcher of the Laboratory of Advanced Functional Materials, UrFU.

<https://orcid.org/0000-0002-5823-9554>

E-mail: nina\_zhirenkina@mail.ru

**Максим Алексеевич Машковцев** – к.х.н., науч. сотрудник лаборатории электрохимических устройств и топливных элементов, ИВТЭ УрО РАН.

<https://orcid.org/0000-0002-4914-262X>

E-mail: maxftf@yandex.ru

**Дмитрий Олегович Поливода** – мл. науч. сотрудник лаборатории электрохимических устройств и топливных элементов, ИВТЭ УрО РАН.

<https://orcid.org/0000-0002-3514-9919>

E-mail: sbbthblack@gmail.com

**Нина Валерьевна Жиренкина** – к.т.н., ст. науч. сотрудник лаборатории перспективных функциональных материалов, УрФУ.

<https://orcid.org/0000-0002-5823-9554>

E-mail: nina\_zhirenkina@mail.ru

---

## Contribution of the authors

**S.V. Buinachev** – processed experimental data, wrote the manuscript, participated in the discussion of the results.

**M.A. Domashenkov** – conducted experiments, wrote the manuscript, processed documents for submitting the manuscript, participated in the discussion of the results.

**M.A. Mashkovtsev** – designed the experiment plan, revised the manuscript.

**D.O. Polivoda** – processed experimental data, graphical visualization of data.

**N.V. Zhirenkina** – graphical visualization of data, conducted experiments.

## Вклад авторов

**С.В. Буйначев** – обработка экспериментальных данных, написание текста статьи, участие в обсуждении результатов.

**М.А. Домашенков** – проведение экспериментов, написание текста статьи, участие в обсуждении результатов.

**М.А. Машковцев** – составление плана экспериментов, редактирование текста статьи.

**Д.О. Поливода** – обработка экспериментальных данных, графическая визуализация результатов исследований.

**Н.В. Жиренкина** – графическая визуализация данных, проведение экспериментов.

---

*The article was submitted 05.12.2023, revised 08.02.2024, accepted for publication 15.02.2024*

*Статья поступила в редакцию 05.12.2023, доработана 08.02.2024, подписана в печать 15.02.2024*

UDC 621.9.048

<https://doi.org/10.17073/0021-3438-2024-2-55-69>

Research article

Научная статья



## Fabrication of high speed steel electrodes with $\text{MoSi}_2$ – $\text{MoB}$ – $\text{HfB}_2$ ceramic additives for electrospark deposition on die steel

A. Akhmetov<sup>1</sup>, Zh.V. Eremeeva<sup>1</sup>, A.E. Kudryashov<sup>1</sup>, P.A. Loginov<sup>1</sup>, S.D. Shlyapin<sup>2,1</sup>, M.E. Samoshina<sup>1</sup>, E.A. Levashov<sup>1</sup>

<sup>1</sup> National University of Science and Technology “MISIS”

4 Bld 1 Leninskiy Prosp., Moscow 119049, Russia

<sup>2</sup> Moscow Aviation Institute (National Research University)

4 Volokolamskoe shosse, Moscow 125993, Russia

✉ Amankeldy Akhmetov (amanlaotero@gmail.com)

**Abstract:** The electrodes for electrospark deposition (ESD) were fabricated from hot-pressed blanks composed of a mechanically alloyed powder mixture of R6M5K5 high speed steel. This mixture was enriched with a 40 % addition of heat-resistant  $\text{MoSi}_2$ – $\text{MoB}$ – $\text{HfB}_2$  ceramics, produced through the self-propagating high-temperature synthesis method (resulting in the R6M5K5-K electrode), as well as variant without any ceramic addition (resulting in the R6M5K5 electrode). We examined both the composition and structure of the electrode materials and the coatings derived from them, identifying the characteristics of mass transfer from hot-pressed electrodes to substrates of 5KhNM die steel under various frequencies and energy conditions during processing. The R6M5K5 electrode consists of an  $\alpha$ -Fe-based matrix incorporating dissolved alloying elements and contains discrete particles of ferrovanadium, tungsten carbide, and molybdenum. The R6M5K5-K electrode, in addition to the  $\alpha$ -Fe-based matrix, includes borides and carbides, as well as hafnium oxide. The use of the R6M5K5 electrode resulted in a consistent weight increase in the cathode throughout the entire 10-minute processing period. In contrast, the application of the ceramic-enhanced electrode led to weight gain only during the initial 3 min of processing. Subsequently, ESD produced coatings of 22 and 50  $\mu\text{m}$  thickness on the surface of 5KhNM steel using R6M5K5 and R6M5K5-K electrodes, respectively. The introduction of SHS ceramics escalated the roughness ( $R_a$ ) of the surface layers from 6 to 13  $\mu\text{m}$  and the hardness from 9.1 to 15.8 GPa. The coating from the R6M5K5 electrode was composed of austenite ( $\gamma$ -Fe) and exhibited high uniformity. Conversely, the coating from the R6M5K5-K electrode consisted of a diverse matrix with both crystalline and amorphous iron, an amorphous phase rooted in the Fe–B alloy, and scattered phases of  $\text{HfO}_2$ ,  $\text{HfSiO}_4$ ,  $\text{Fe}_3\text{Si}$ , and  $\text{Fe}_3\text{B}$ . High-temperature tribological testing at 500 °C in an air atmosphere showed that the coatings possess a friction coefficient of 0.55–0.57 when coupled with a counterbody of AISI 440C steel. The integration of heat-resistant ceramics notably enhanced the coating's wear resistance, increasing it by a factor of 13.5.

**Keywords:** electrospark deposition, powder high speed steel, tool steel, ceramics, silicides, borides, oxides, self-propagating high-temperature synthesis, wear resistance.

**Acknowledgments:** The study was supported by the Russian Science Foundation grant No. 23-49-00141: <https://rscf.ru/project/23-49-00141/>

**For citation:** Akhmetov A., Eremeeva Zh.V., Kudryashov A.E., Loginov P.A., Shlyapin S.D., Samoshina M.E., Levashov E.A. Fabrication of high speed steel electrodes with  $\text{MoSi}_2$ – $\text{MoB}$ – $\text{HfB}_2$  ceramic additives for electrospark deposition on die steel. *Izvestiya. Non-Ferrous Metallurgy*. 2024;30(2):55–69. <https://doi.org/10.17073/0021-3438-2024-2-55-69>

# Получение электрода из быстрорежущей стали с керамической добавкой MoSi<sub>2</sub>–MoB–HfB<sub>2</sub> для электроискровой обработки штамповой стали

А. Ахметов<sup>1</sup>, Ж.В. Еремеева<sup>1</sup>, А.Е. Кудряшов<sup>1</sup>, П.А. Логинов<sup>1</sup>, С.Д. Шляпин<sup>2,1</sup>, М.Е. Самошина<sup>1</sup>, Е.А. Левашов<sup>1</sup>

<sup>1</sup> Национальный исследовательский технологический университет «МИСИС»  
Россия, 119049, г. Москва, Ленинский пр-т, 4, стр. 1

<sup>2</sup> Московский авиационный институт (национальный исследовательский университет)  
Россия, 125993, г. Москва, Волоколамское шоссе, 4

✉ Аманкельды Ахметов (amanlaotero@gmail.com)

**Аннотация:** Получены электроды для электроискровой обработки (ЭИО) из горячепрессованных заготовок механически легированной порошковой смеси быстрорежущей стали марки P6M5K5 с 40 %-ной добавкой жаростойкой керамики MoSi<sub>2</sub>–MoB–HfB<sub>2</sub>, полученной методом самораспространяющегося высокотемпературного синтеза (электрод марки P6M5K5-K), и без добавки (электрод P6M5K5). Изучены состав и структура электродных материалов и сформированных из них покрытий. Определены особенности массопереноса горячепрессованных электродов на подложках из штамповой стали 5XHM при варьировании частотно-энергетических режимов обработки. Электрод P6M5K5 состоит из матрицы на основе  $\alpha$ -Fe, в которой растворены легирующие элементы, и нерастворенных частиц феррованадия, карбида вольфрама и молибдена. Электрод P6M5K5-K содержит матрицу на основе  $\alpha$ -Fe, бориды и карбид, а также оксид гафния. При использовании электрода P6M5K5 наблюдался устойчивый привес на катоде за все 10 мин обработки. В случае электрода с добавкой керамики привес отмечался в первые 3 мин легирования. В результате ЭИО на поверхности стали 5XHM были сформированы покрытия толщиной до 22 и 50 мкм для P6M5K5 и P6M5K5-K соответственно. Введение СВС-керамики способствовало росту шероховатости ( $R_a$ ) поверхностных слоев с 6 до 13 мкм и твердости с 9,1 до 15,8 ГПа. Покрытие из электрода P6M5K5 состояло из аустенита ( $\gamma$ -Fe) и характеризовалось высокой однородностью. Покрытие из электрода P6M5K5-K представляло собой гетерогенную матрицу на основе кристаллического и аморфного железа, аморфной фазы на основе сплава Fe–В и дисперсных фаз HfO<sub>2</sub>, HfSiO<sub>4</sub>, Fe<sub>3</sub>Si и Fe<sub>3</sub>B. Высокотемпературными трибологическими испытаниями при температуре 500 °С на воздухе выявлено, что покрытия обладают коэффициентом трения 0,55–0,57 в паре с контртелом из стали AISI 440C, а введение добавки жаростойкой керамики способствовало увеличению износостойкости покрытия в 13,5 раза.

**Ключевые слова:** электроискровая обработка, легирование, порошковая быстрорежущая сталь, инструментальная сталь, керамика, силициды, бориды, оксиды, самораспространяющийся высокотемпературный синтез, износостойкость.

**Благодарности:** Исследование выполнено за счет гранта Российского научного фонда № 23-49-00141, <https://rscf.ru/project/23-49-00141/>

**Для цитирования:** Ахметов А., Еремеева Ж.В., Кудряшов А.Е., Логинов П.А., Шляпин С.Д., Самошина М.Е., Левашов Е.А. Получение электрода из быстрорежущей стали с керамической добавкой MoSi<sub>2</sub>–MoB–HfB<sub>2</sub> для электроискровой обработки штамповой стали. *Известия вузов. Цветная металлургия*. 2024;30(2):55–69. <https://doi.org/10.17073/0021-3438-2024-2-55-69>

## Introduction

During operation, die tools subjected to high temperatures face rapid wear and crack propagation due to thermal effects, friction, adhesion, and micro-cracks, among other causes [1–4]. Consequently, tools require frequent replacement, leading to workflow disruptions and significant economic costs.

Electrospark deposition (ESD) of wear-resistant coatings using various electrode materials has proven to be an effective method to restrain rapid wear and ex-

tend the service life of die tools [5; 6]. These materials include graphite [7; 8], metals [9; 10], alloys [11; 12], ceramics [13; 14], and hard alloys [15; 16]. The broad spectrum of electrode materials available allows for the selection of an appropriate composition to tailor the coating for a specific functional requirement. Furthermore, the application of high-energy modes expands the capabilities of the method, facilitating the restoration of worn tool surfaces [17]. The production of elec-

trodes by consolidating powdered components enables the incorporation of the aforementioned materials, which are often runoff products, thereby significantly improving the prospects for industrial application [18–21].

Wear-resistant and heat-resistant electrode materials are essential for hardening the surfaces of dies operating at elevated temperatures. In this context, heterophase ceramic composite  $\text{MoSi}_2\text{—MoB—HfB}_2$ , derived from self-propagating high-temperature synthesis (SHS), merits particular attention due to its highly homogeneous component distribution within the mixture [22; 23]. Although electrospark coatings produced from this ceramic are extremely hard and heat-resistant—an important attribute for hardening high-temperature tools—they are also characterized by a low deposition rate and inadequate wear resistance in high-temperature tribological tests [23]. To improve mass transfer in the discharge arc and to bolster the wear resistance of the coatings, cermet electrodes, comprising a metallic binder and a refractory component, are employed. High speed steel (HSS), known for its red-hardness (the ability to maintain hardness at elevated temperatures) and high wear resistance, is a suitable choice for the binder [24; 25]. Additionally, the use of HSS not only enhances wear resistance at high temperatures but also reduces costs and streamlines the electrode production process by lowering the sintering temperature.

The aim of this study was to fabricate electrodes from hot-pressed blanks of mechanically alloyed powder mixture of R6M5K5 high speed steel with  $\text{MoSi}_2\text{—MoB—HfB}_2$  ceramics, and to investigate the characteristics of electrospark coating formation on 5KhNM die steel.

## Materials and methods

The widely used R6M5K5 steel was selected as the binder. It was fabricated in the Activator-4M planetary

ball mill (PBM) (CJSC “Activator”, Novosibirsk) from elemental powders by mixing Fe, W, Mo, Co, Cr, C, and ferrovanadium FVd50U0.5 (FVd) with the following ratio, wt.%: 6.0 W; 5.0 Mo; 5.0 Co; 4.0 Cr; 0.9 C; 4.0 FVd (2.0 V); with the remainder being Fe. The characteristics of the powders are presented in Table 1.

The components were mixed for 30 minutes with the drums rotating at a rate of 800 rpm. The main fraction of finished HSS mixture exhibited a grain size of 3–20  $\mu\text{m}$ , with an average particle size of 10  $\mu\text{m}$ .

Heterophase ceramics with a composition of 60 % (90% $\text{MoSi}_2\text{—}10\%\text{MoB}$ ) plus 40 %  $\text{HfB}_2$  were synthesized using the method outlined in [22]. The SHS sintered material was pulverized in a rotary ball mill to produce a powder with a particle size of less than 40  $\mu\text{m}$ . This powder, constituting 40 % of the mix, was combined with the HSS powder in a PBM Pulverisette 5/2 (“Fritsch”, Germany) for 60 minutes, with the drums rotating at a speed of 300 rpm.

The final composition of the powder mixture was as follows, wt.%: 3.6 W; 3.0 Mo; 3.0 Co; 2.4 Cr; 0.54 C; 1.2 V; 21.6  $\text{MoSi}_2$ ; 2.4 MoB; 16.0  $\text{HfB}_2$ ; the remainder being Fe.

Blanks made of R6M5K5 steel (R6M5K5 electrode) and the HSS mixture with heterophase ceramics (R6M5K5-K electrode) were produced by hot pressing (HP) at a temperature of 1000 °C, under a pressure of 50 MPa, with a holding time of 3 minutes using the DSP-515 SA press (“Dr. Fritsch Sondermaschinen GmbH”, Germany) in a graphite mold of 50 mm diameter. Electrodes measuring 20–50 mm in length and having a cross-section of 5×5 mm were fashioned by wire electrical discharge machining of the hot-pressed blanks on the ARTA 200-2 EDM machine (JSC “Scientific Industrial Corporation Delta-Test”, Fryazino).

The ESD process was performed using Alier-Metal 30 and Alier-Metal G53 setups (SPA “Metal” LLC —

Table 1. Characteristics of powders used in the preparation of the R6M5K5 powder mixture

Таблица 1. Характеристики порошков, использованных для получения порошковой смеси Р6М5К5

Powder brand	Element	GOST/TS	Particle size, $\mu\text{m}$	Purity, %
PZhRV 2.200.26	Fe	TS 14-5365-98	<120	99.24
PVCh	W	TS 48-19-57-91	1–5	99.99
PMCh	Mo	TS 14-22-160-2002	40–60	99.90
PK-1	Co	GOST 9721-79	<50	99.95
ERKh-1	Cr	GOST 5905-2004	<50	99.99
FVd50U0.5	V	GOST 27130-94	<50	99.00
P-803	C	GOST 7885-86	<20	99.90

Table 2. ESD process parameters

Таблица 2. Параметры процесса ЭИО

Mode	Setup	Pulsed discharge current rate, A	Recurrence rate, Hz	Pulse duration, μs	Single-pulse energy, J	Total energy ΣE, kJ·min
1	Alier-Metal 30	170	1500	25	0.1	7.65
2	Alier-Metal 30	170	3000	25	0.1	15.30
3	Alier Metal G53*	200	400	100	0.4	9.60

\* Auxiliary generator.

SCINTI S.R.L., Russia — Moldova) under varying frequency and energy treatment conditions, the specifics of which are detailed in Table 2.

The deposition of the coating was achieved through the alternating localized impact of pulsed discharge on all areas of the processing surface of 5KhNM steel samples. This was done by having the anode repeatedly pass over the same cathode area in an argon environment.

The kinetics of mass transfer — specifically, the anode erosion ( $\Delta A_i$ ) and the cathode's specific weight gain ( $\Delta K_i$ ) — for the R6M5K5 and R6M5K5-K electrodes was determined using a gravimetric method on a KERN 770 analytical balance (KERN, Germany) with an accuracy of  $10^{-5}$  g. The electrodes were weighed after treating an area of  $1 \text{ cm}^2$  for 1 minute, with the treatment continuing for a total of 10 minutes. The total cathode weight gain,  $\Sigma \Delta K_i$ , was calculated using the formula [26]:

$$\Sigma \Delta K_i = \Delta K_1 + \Delta K_2 + \dots + \Delta K_{10}, \quad (1)$$

where  $\Delta K_i$  is the cathode weight gain for the  $i$ -th minute of alloying, g;  $i = 1, 2, \dots, 10$ .

The total anode erosion  $\Sigma \Delta A_i$  was calculated similarly.

The microstructure of the fabricated electrodes and coatings was examined using a S-3400N scanning electron microscope (SEM) ("Hitachi High-Technologies Corporation", Japan), equipped with a NORAN System 7 energy-dispersive spectrometer for X-ray microanalysis ("Thermo Scientific", USA).

X-ray diffractometric (XRD) phase analysis of the electrodes was conducted using a DRON-4 diffractometer (Research and Production Enterprise "Bourestnik", St. Petersburg) with  $\text{CoK}_\alpha$  radiation. For the XRD analysis of electrospark coatings, a D2 PHASER diffractometer ("Bruker AXS GmbH", Germany) with monochromatic  $\text{CoK}_\alpha$  radiation was utilized.

The surface topography of the coatings and the profiles of the wear tracks were analyzed using a WYKO NT 1100 optical profilometer (VEECO, USA).

Hardness measurements on cross-sections were performed using the method of instrumented indentation with a NanoHardness Tester ("CSM Instruments", Switzerland), in accordance with GOST R 8.748-2011 (ISO 14577).

Tribological testing of the coatings was carried out in accordance with the ASTM G 99 standard, employing a pin-on-disk configuration on a High-Temperature Tribometer ("CSM Instruments", Switzerland). A 6 mm diameter ball made of AISI 440C steel (equivalent to 95X18) served as the counterbody. The test conditions were as follows: temperature at  $500^\circ\text{C}$ , load at 5N, linear velocity at 10 cm/s, counterbody path length at 500 m, and track length at 3.76 cm.

Wear resistance ( $W$ ) was calculated using the formula:

$$W = SL/(HI), \quad (2)$$

where  $S$  is the cross-sectional area of the groove wear,  $\text{mm}^2$ ;  $L$  is the track length, mm;  $H$  is the load, N; and  $I$  is the friction path, m.

The microstructure of the lamella from the coating deposited by the R6M5K5-K electrode was examined using a JEM-2100 microscope ("Jeol", Japan) employing high-resolution transmission electron microscopy (HR TEM). The lamella samples were prepared using a focused ion beam tool (Quanta 200 3D FIB Instrument, FEI Company, USA). *In situ* observations were also conducted within the transmission electron microscope column at a temperature of  $500^\circ\text{C}$ .

## Results and discussion

### Characteristics of electrodes

The outcomes of the XRD analysis for the R6M5K5-K electrode are detailed in Table 3. Analysis reveals that the electrode comprises an  $\alpha$ -Fe-based matrix, borides including  $(\text{Mo,W})_2\text{FeB}_2$ ,  $\text{Mo}_3\text{CoB}_3$ , and HfB,  $\text{Mo}_6\text{Fe}_6\text{C}$  carbide, and hafnium oxide. A notable decrease in the lattice constant of the  $\alpha$ -Fe phase was

observed, indicative of silicon dissolution. This dissolution is likely to significantly reduce the  $\alpha$ -Fe lattice constant [27], a finding that aligns with the elemental distribution maps shown in Fig. 1.

According to the SEM and EDS data (Table 4) for the R6M5K5-K electrode, the identified structural components include HfB hafnium monoboride; an iron-based phase ( $\alpha$ -Fe) containing dissolved alloying elements from the HSS itself as well as silicon from the heterophase ceramics; and a complex carbide of iron and molybdenum,  $\text{Mo}_6\text{Fe}_6\text{C}$ .

Figure 2 displays the SEM image showing the microstructure of the electrode composed of HSS R6M5K5, alongside the element distribution map. The image reveals that the Fe-based matrix is made up of grains ranging from 1 to 2  $\mu\text{m}$ , within which alloying elements (Co and Cr) are uniformly dissolved. The matrix contains particles of different colors; based on the EDS data and

Table 3. Phase composition of R6M5K5-K electrode

Таблица 3. Фазовый состав электрода Р6М5К5-К

Phase	Content		Lattice constant, nm
	vol.%	wt.%	
$\alpha$ -Fe	48.4	44.8	$a = 0.2844$
$(\text{Mo,W})_2\text{FeB}_2$	23.9	23.9	$a = 0.55731$ $c = 0.3136$
$\text{Mo}_6\text{Fe}_6\text{C}$	17.2	18.3	$a = 1.1022$
$\text{Mo}_3\text{CoB}_3$	2.6	2.7	–
$\text{HfO}_2$	5.2	6.1	–
HfB	2.2	3.3	$a = 0.4568$

the element distribution map, it's determined that the lighter particles are tungsten carbide (WC), produced through mechanical alloying, whereas the darker par-

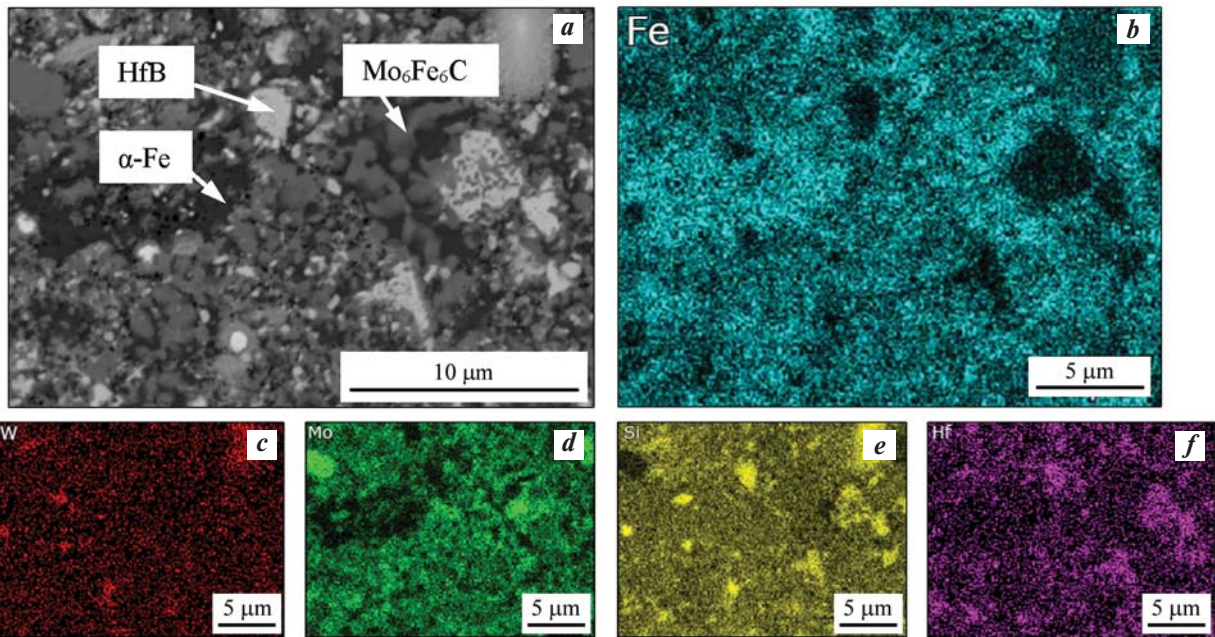


Fig. 1. SEM image of the microstructure of R6M5K5-K electrode (a) and the element distribution map: Fe (b), W (c), Mo (d), Si (e), and Hf (f)

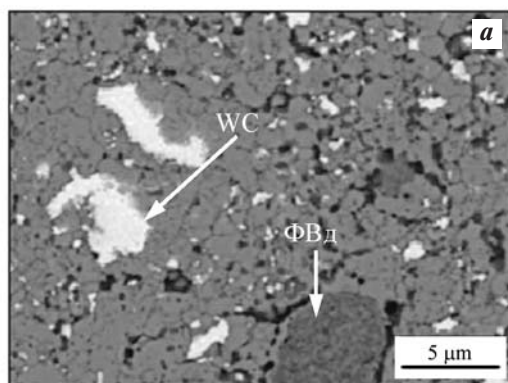
Рис. 1. РЭМ-изображение микроструктуры электрода Р6М5К5-К (a) и карта распределения элементов: Fe (b), W (c), Mo (d), Si (e) и Hf (f)

Table 4. Chemical composition (at.%) of structural components in the R6M5K5-K electrode

Таблица 4. Химический состав (ат.%) структурных составляющих электрода Р6М5К5-К

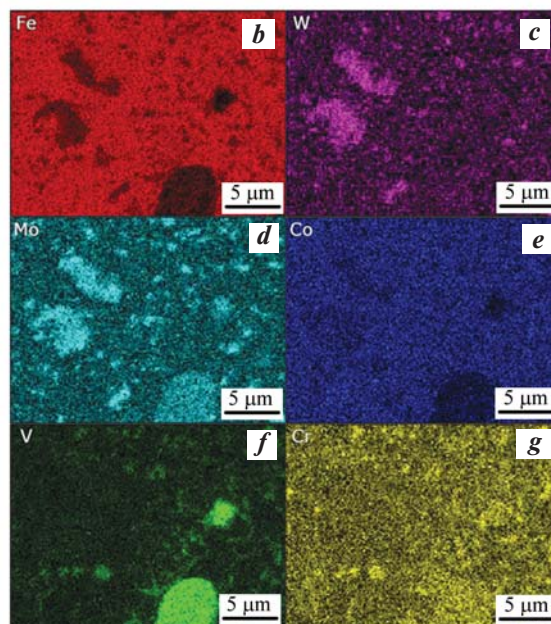
Phase	C	O	Si	V	Cr	Co	Fe	Mo	Hf	W
HfB*	–	–	0.4	3.3	0.5	–	11.4	15.4	69.0	–
$\alpha$ -Fe	–	6.2	20.9	1.6	1.3	3.3	62.5	3.6	–	0.6
$\text{Mo}_6\text{Fe}_6\text{C}$	47.9	–	9.4	1.5	1.7	1.7	22.1	15.2	–	0.2

\*The phase was determined based on the XRF results.



**Fig. 2.** SEM image of the microstructure of R6M5K5 electrode (a) and the element distribution map: Fe (b), W (c), Mo (d), Co (e), V (f) and Cr (g)

**Рис. 2.** РЭМ-изображение микроstructures электрода Р6М5К5 (а) и карта распределения элементов: Fe (b), W (c), Мо (d), Со (e), V (f) и Cr (g)



ticles are identified as ferrovanadium (FVd). Both WC particles and the undissolved FVd include molybdenum, which is known to form a continuous range of solid solutions with tungsten (W) and vanadium, suggesting a complex interplay of these elements within the electrode's microstructure [28; 29].

### Preparation and properties of electrospark coatings

Figure 3 illustrates the effect of the ESD duration using R6M5K5 and R6M5K5-K electrodes on both cathode weight gain and anode erosion. The use of the R6M5K5 electrode leads to a consistent increase in cathode weight alongside similar rates of electrode erosion. A significant correlation was found between the increase in total pulse energy and the weight gain of the substrate, making mode 2 ( $\Sigma E = 15.30 \text{ kJ} \cdot \text{min}$ ) the preferred option for the R6M5K5 electrode due to it resulting in the greatest weight gain over a 10-minute deposition period.

Conversely, for the R6M5K5-K electrode, all tested modes yield nearly identical cathode weight gains, which plateau after the first 3 minutes of deposition. The limitation in coating thickness can be attributed to the buildup of internal stresses, a decrease in the thermal resistance of the coating, and the development of an ultra-dispersed structure within it [26].

For the purpose of visually examining the surface topography, the surface roughness ( $R_a$ ) of the coatings deposited over 3 minutes for each of the three modes was measured. Figure 4 presents 3D images of these surfaces along with their  $R_a$  values. It is ev-

ident that the use of the R6M5K5 electrode results in a slightly lower surface roughness compared to the R6M5K5-K electrode. The analysis of mass transfer and roughness kinetics indicates that mode 2 is the most favorable. This mode achieves the lowest roughness while ensuring high mass transfer for the R6M5K5 electrode and moderate mass transfer for the R6M5K5-K electrode.

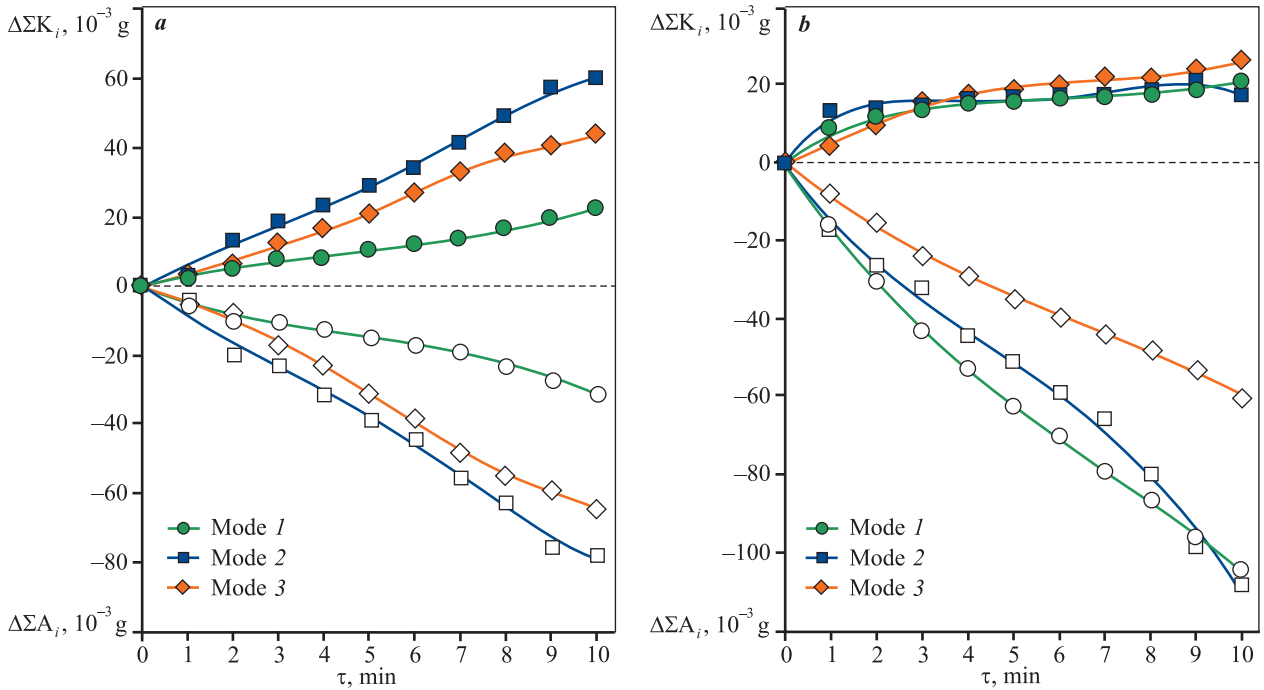
The coatings applied using mode 2 were examined via scanning electron microscopy (SEM). Figures 5 and 6 illustrate the surface topography and the cross-sectional structure of the coating-substrate interface, respectively.

Figure 5 demonstrates that the coating deposited from R6M5K5 electrode without ceramics represents overlaying of spreading drips of melt formed in the pulsed discharge arc. There are almost no cracks in the coating and micropores are detected in the surface layer. The coating is 20–22  $\mu\text{m}$  thick and the transition layer is 5–6  $\mu\text{m}$ . According to the XRD data, along with EDS (Table 5), the coating deposited from R6M5K5 electrode consists of  $\gamma$ -Fe. Austenite ( $\gamma$ -Fe) is formed due to high rates of melt crystallization from the electrode material, which is practically a hardening operation [17]. Ni, Si and Mn are present in the transition layer and form part of the substrate.

Based on the XRD data, the coating deposited from the R6M5K5-K electrode is composed of various phases:  $\alpha$ -Fe, HfO<sub>2</sub>, HfSiO<sub>4</sub>, Fe<sub>3</sub>Si, and Fe<sub>3</sub>B. It is suggested that hafnium silicate HfSiO<sub>4</sub> forms in the discharge arc, a result of the reaction between hafnium oxide (present in the electrode) and silicon

oxide  $\text{SiO}_2$ . The silicon oxide likely forms from the oxidation of silicon by impurity oxygen present in the environment.

The use of the R6M5K5-K metal-ceramic electrode leads to increased surface roughness and heterogeneity in the coating's structure. According to the results



**Fig. 3.** Dependence of the mass gain of the cathode ( $\Delta\Sigma K_i$ ) and the erosion of the anode ( $\Delta\Sigma A_i$ ) on the duration of ESD of 5KhNM steel with R6M5K5 (a) and R6M5K5-K (b) electrodes

**Рис. 3.** Зависимости привеса массы катода ( $\Delta\Sigma K_i$ ) и эрозии анода ( $\Delta\Sigma A_i$ ) от длительности электроискровой обработки стали 5ХНМ электродами Р6М5К5 (a) и Р6М5К5-К (b)

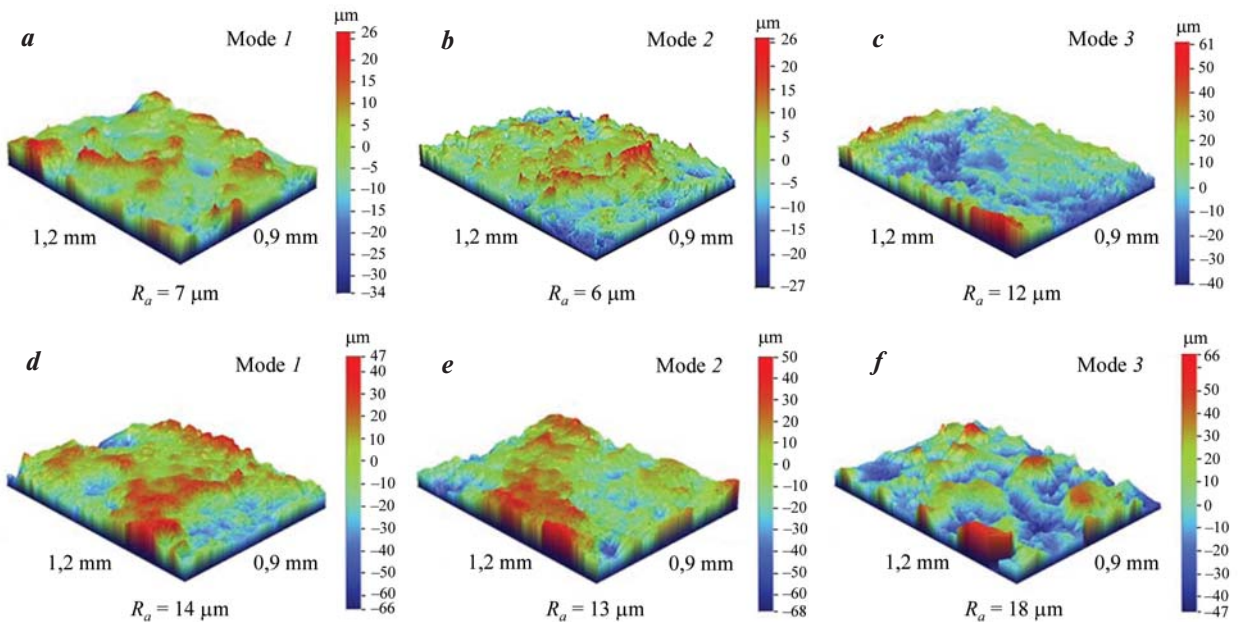


**Fig. 4.** Surface topography and roughness of coatings deposited from R6M5K5 (a–c) and R6M5K5-K (d–f) electrodes in ESD modes 1 (a, d), 2 (b, e), and 3 (c, f)

**Рис. 4.** Топография поверхности и шероховатость покрытий из электродов Р6М5К5 (a–c) и Р6М5К5-К (d–f) на ЭИО-режимах 1 (a, d), 2 (b, e), 3 (c, f)

of EDS analysis presented in Table 6, which analyzed different areas of the coating as marked in Fig. 6, *b*, the thickness of the coating varies between 20 and 30 μm, with some areas reaching up to 50 μm. Under high magnification, a fine-grained microstructure is visible, with grain sizes ranging from 0.3 to 0.6 μm. Additionally, a dendritic structure, reminiscent of eutectics, is also observed alongside dispersed inclusions smaller than 0.1 μm. The iron-based matrix incorporates dissolved alloying elements from both the steel and the ceramic additive.

The submicron and nanosized structural components of the coating were analyzed using the transmission electron microscopy method (TEM). Figure 7 showcases SEM images of the lamella before (Fig. 7, *a*) and after (Fig. 7, *c*) heating to 500 °C. Additionally, diffraction patterns of sections of the α-Fe-based ma-

trix (Fig. 7, *b*) and the Fe–B-based amorphous phase (Fig. 7, *d*) are displayed. The specific area from which the lamella was extracted is indicated in Fig. 6, *b*.

Using SEM (Fig. 7) and EDS analysis (Table 7) we characterized the composition of an α-Fe-based crystalline matrix interspersed with amorphous inclusions of a similar composition. These amorphous inclusions arose both from the rapid cooling associated with the ESD process and the presence of amorphizing elements such as boron and silicon [30; 31]. Furthermore, we identified an Fe–B amorphous phase containing inclusions of Fe<sub>3</sub>B iron boride nanoparticles. These nanoparticles are released upon heating as the amorphous matrix segregates into Fe<sub>3</sub>B and α-Fe [32]. Distributed throughout the matrix volume are nanoparticles of HfO<sub>2</sub>, measuring 30–50 nm, and iron silicide Fe<sub>3</sub>Si, which are 15–20 nm in size.

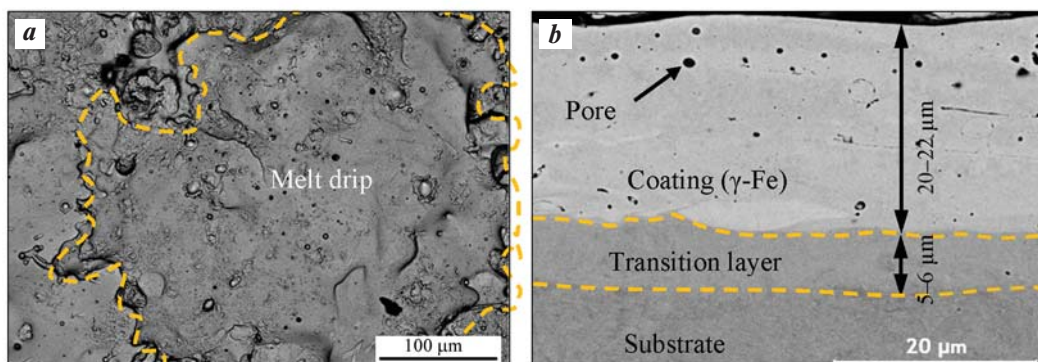


Fig. 5. SEM images of the topography (*a*) and structure (*b*) of the coating (mode 2) deposited from R6M5K5 electrode

Рис. 5. РЭМ-изображения топографии (*a*) и структуры (*b*) покрытия (режим 2) из электрода Р6М5К5

Table 5. Chemical composition (at.%) of various areas within the coating deposited from R6M5K5 electrode

Таблица 5. Химический состав (ат.%) областей покрытия, полученного электродом Р6М5К5

Area of analysis	C	Si	V	Cr	Mn	Fe	Co	Ni	Mo	W
Coating	15.0	–	2.2	2.0	–	74.5	3.0	–	1.8	1.4
Transition layer	9.4	0.6	–	0.7	1.0	86.8	0.0	1.6	–	0.1
Substrate	10.3	0.6	–	0.8	0.7	86.1	0.0	1.4	–	–

Table 6. Chemical composition (at.%) of the coating areas marked in Fig. 6, *b*

Таблица 6. Химический состав (ат.%) областей покрытия, отмеченных на рис. 6, *b*

Area	C	O	Si	V	Cr	Mn	Fe	Ni	Mo	Hf
1	–	66.3	–	–	–	–	1.9	–	–	31.8
2	16.2	–	13.9	1.4	1.5	–	59.0	–	6.4	1.5
3	23.8	34.1	5.5	1.2	1.4	–	25.8	–	6.8	1.4
4	24.4	40.8	4.5	0.7	–	0.4	25.7	–	3.3	0.2
5	11.6	–	0.8	–	0.5	0.8	84.7	1.5	–	–

Table 7. Chemical composition (at.%) of the areas marked in Fig. 7, a

Таблица 7. Химический состав (ат.%) областей, отмеченных на рис. 7, a

Area	Component	Fe	W	Mo	Hf	Si	Cr	V	Co	O
1	Crystal matrix	84.7	1.2	4.0	–	4.8	1.4	0.5	2.0	–
2	Amorphous matrix	87.5	1.0	4.0	–	4.2	1.4	0.5	1.4	–
3	Particle based on HfO <sub>2</sub>	4.6	–	–	31.0	–	–	–	–	64.4
4	Fe–B amorphous phase*	21.7	–	–	–	–	–	–	–	78.3

\* The phase was determined based on the diffraction pattern.

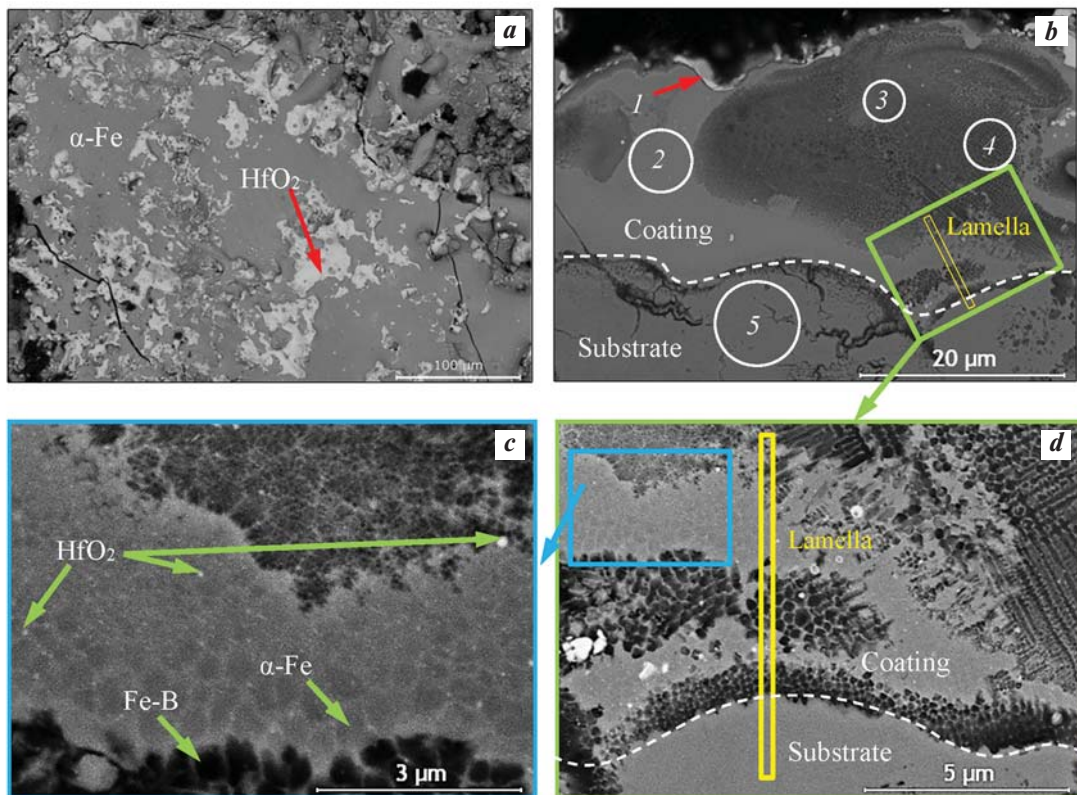


Fig. 6. SEM images of the surface topography (a) and the microstructure (b–d) of the coating deposited from R6M5K5-K electrode

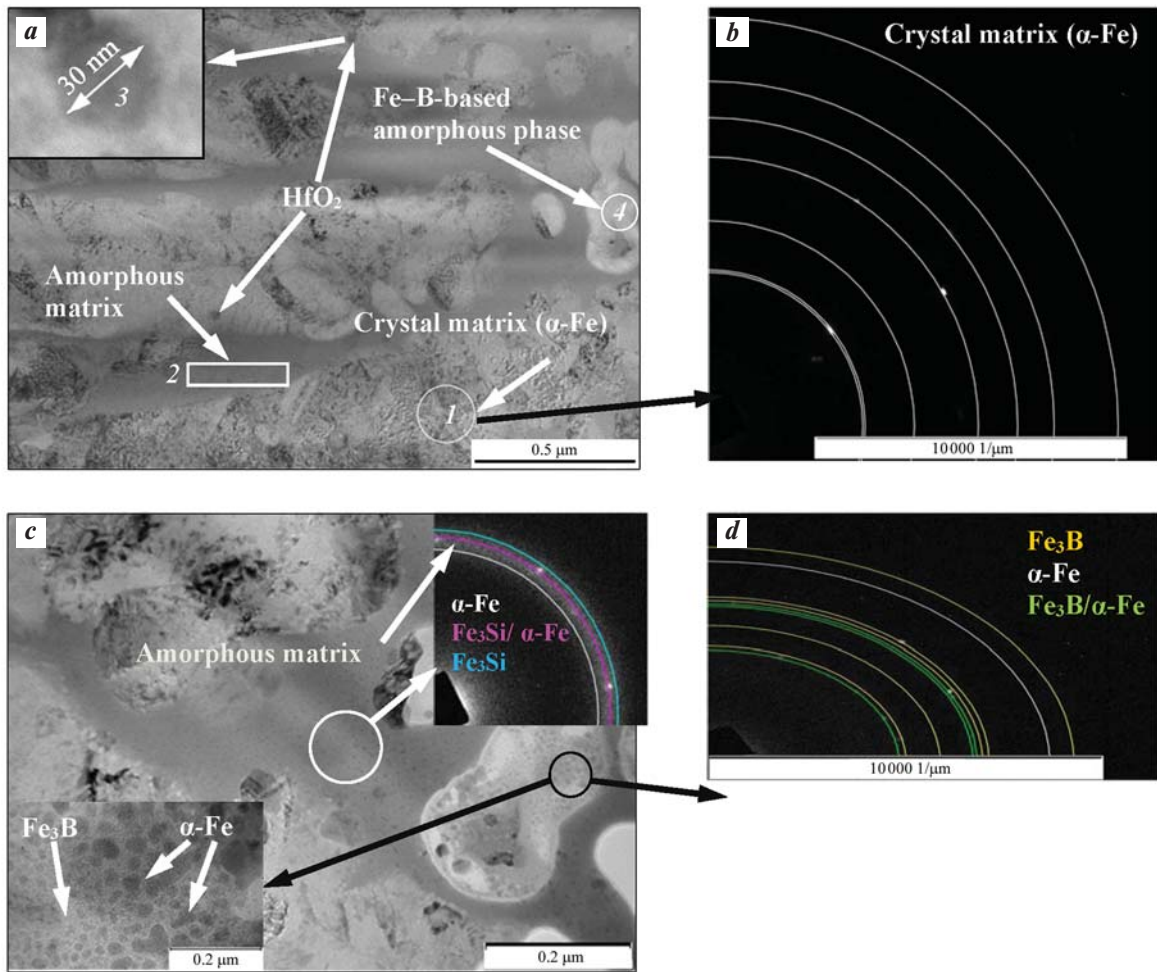
Рис. 6. РЭМ-изображения топографии поверхности (a) и микроструктуры (b–d) покрытия, полученного из электрода Р6М5К5-К

The results from nanoindentation measurements of electrospark coatings deposited from R6M5K5 and R6M5K5-K electrodes were analyzed, and hardness distributions across the coating thickness are illustrated in Fig. 8. It is noticeable that the hardness of the coating deposited from the R6M5K5-K electrode is  $15.8 \pm 0.4$  GPa, which is significantly higher than the  $9.1 \pm 0.4$  GPa hardness of the coating deposited from the R6M5K5 electrode. This increase in hardness is attributed to the inclusion of hardening phases such as HfO<sub>2</sub>, HfSiO<sub>4</sub>, Fe<sub>3</sub>B, Fe<sub>3</sub>Si within the coating.

### High-temperature tribological tests

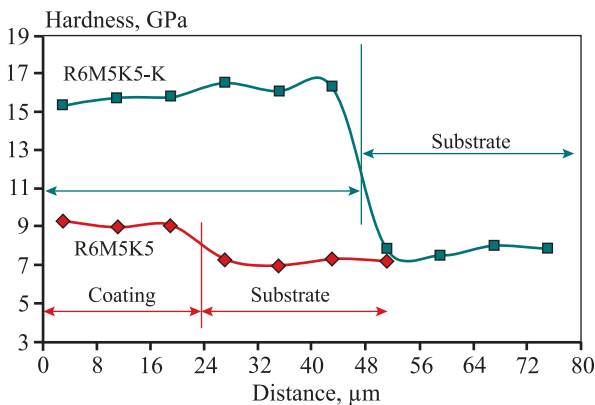
A critical attribute for tools used in isothermal forging is their wear resistance under conditions of high-temperature friction. While tribological tests conducted according to standard methodologies may not perfectly replicate the actual operating conditions of dies, the results are nevertheless indicative of the impact of the coatings on wear resistance.

Figure 9 illustrates the relationship between the friction coefficient of 5KhNM steel samples with



**Fig. 7.** TEM images of the coating deposited from R6M5K5-K electrode before (a) and after (c) heating the lamella to 500 °C, diffraction pattern of  $\alpha$ -Fe-based matrix (b) and Fe–B-based amorphous phase after heating (d)

**Рис. 7.** ПЭМ- изображения покрытия из электрода Р6М5К5-К до (а) и после (с) нагрева ламели до 500 °С, а также дифракционная картина матрицы на основе  $\alpha$ -Fe (b) и аморфной фазы Fe–В после нагрева (d)



**Fig. 8.** Hardness distribution over the thickness of electrospark coatings deposited with R6M5K5 and R6M5K5-K electrodes

**Рис. 8.** Распределение твердости по толщине электроискровых покрытий из электродов Р6М5К5 и Р6М5К5-К

coatings and the counterbody path length at a temperature of 500 °C, along with 2D images of wear track profiles.

Although the friction coefficients for both coatings are similar, ranging from 0.55 to 0.57, the values of reduced wear show significant differences:  $38.24 \cdot 10^{-5} \text{ mm}^3/\text{N/m}$  for the coating from R6M5K5 electrode and  $2.82 \cdot 10^{-5} \text{ mm}^3/\text{N/m}$  for the coating from R6M5K5-K electrode. This disparity signifies a substantial increase in wear resistance by 13.5 times for the coating containing hardening phases HfO<sub>2</sub>, HfSiO<sub>4</sub>, Fe<sub>3</sub>B, and Fe<sub>3</sub>Si.

However, a minor fluctuation in the initial path section (20–150 m) for coatings deposited from the R6M5K5-K electrode can be attributed to the counterbody wearing in and the removal of protruding areas of the rough surface ( $R_a = 13 \mu\text{m}$ ). Additionally,

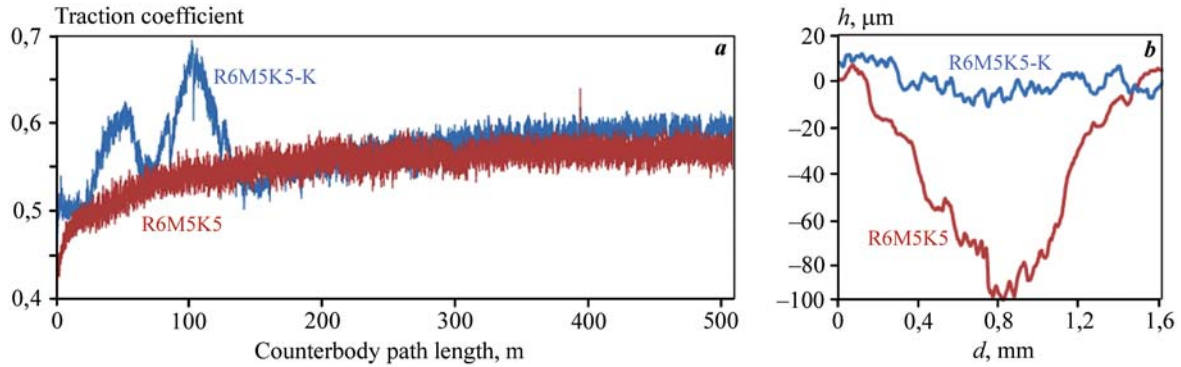


**Fig. 9.** Dependence of the friction coefficient of electrospark coatings deposited from R6M5K5 and R6M5K5-K electrodes on the sliding distance of the counterbody at 500 °C (a) and 2D profiles of wear tracks (b)

**Рис. 9.** Зависимость коэффициента трения электроискровых покрытий из электродов Р6М5К5 и Р6М5К5-К от длины пробега контртела при температуре 500 °С (a) и 2D-профили дорожек износа (b)

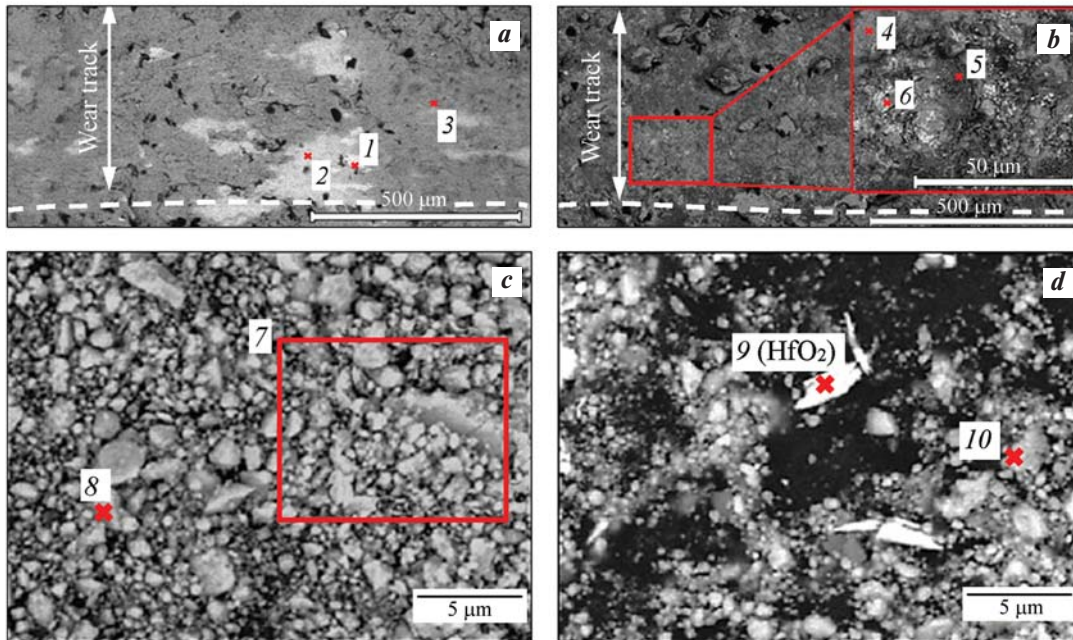


**Fig. 10.** SEM images of tracks (a, b) and wear products (c, d) during the tests of electrospark coatings deposited from R6M5K5 (a, c) and R6M5K5-K (b, d) electrodes

**Рис. 10.** РЭМ-изображения дорожек (a, b) и продуктов износа (c, d) при испытаниях электроискровых покрытий, полученных из электродов Р6М5К5 (a, c) и Р6М5К5-К (b, d)

the chipping of  $\text{HfO}_2$  particles during the tests, as confirmed by their presence in the wear products (illustrated in Fig. 10 and Table 8), contributes to this fluctuation.

Oxidation of the components is observed in both coating formulations. As the coating deposited from the R6M5K5 electrode wears off, layers of the coating that are less oxidized become exposed and emerge on the surface. In contrast, the coating deposited from the R6M5K5-K electrode remains quite homogeneous, exhibiting less pronounced wear traces.

## Conclusions

1. Electrode materials suitable for the electrospark deposition on die steel were sourced from a powdered mixture of R6M5K5 high speed steel and a powdered mixture of R6M5K5 high speed steel with 40 % boride-silicide ceramics ( $\text{MoSi}_2\text{—MoB—HfB}_2$ ). Through the examination of mass transfer and roughness kinetics, the optimal processing mode for 5KhNM die steel was identified, which ensures the lowest surface roughness while maintaining acceptable mass transfer rates.

Table 8. Chemical composition (at.%) of areas in Fig. 10

Таблица 8. Химический состав (ат.%) областей на рис. 10

Area	O	Si	V	Cr	Fe	Co	Mo	W	Hf
Wear tracks (Fig. 10, a, b)									
1	27.2	–	2.1	2.2	61.3	3.5	2.1	1.5	–
2	41.3	–	1.6	2.0	48.9	3.3	1.7	1.3	–
3	55.4	–	0.3	0.5	42.7	0.9	–	–	–
4	27.2	13.7	1.6	2.0	41.0	2.9	7.9	0.8	2.9
5	55.4	3.8	0.3	5.9	31.5	0.6	1.4	–	1.1
6	59.6	–	0.7	0.8	15.2	0.6	2.8	–	20.2
Wear products (Fig. 10, c, d)									
7	54.0	0.8	–	3.6	41.0	–	0.6	–	–
8	42.7	–	1.5	1.5	50.8	–	1.9	1.6	–
9	45.2	5.4	0.7	3.5	28.7	–	2.1	–	14.4
10	47.1	9.7	0.7	1.5	32.4	1.0	3.3	–	4.3

2. The coating applied from R6M5K5 electrode, consisting of austenite, measures 20–22 μm in thickness and is noted for its high uniformity, with a hardness of approximately 9.1±0.4 GPa. On the other hand, the coating from the R6M5K5-K electrode, which incorporates ceramics, features a uniform distribution of hardening phases such as HfO<sub>2</sub>, HfSiO<sub>4</sub>, Fe<sub>3</sub>Si, and Fe<sub>3</sub>B, and varies in thickness from 20 to 30 μm, achieving a hardness of 15.8±0.4 GPa. The dispersed HfO<sub>2</sub> particles are sized between 30–50 nm, while Fe<sub>3</sub>Si particles range from 15–20 nm.

3. High-temperature tribological testing revealed that the coating from the R6M5K5-K electrode exhibits significantly enhanced wear resistance, being 13.5 times greater than that of the coating from the R6M5K5 electrode. The reduced wear rate for the ceramic-enhanced coating was measured at 2.82·10<sup>-5</sup> mm<sup>3</sup>/N/m, attributed to the presence of hardening phases within the coating's structure, compared to 38,24·10<sup>-5</sup> mm<sup>3</sup>/N/m for the austenite-based coating.

## References

1. Straffellini G., Bizzotto G., Zanon V. Improving the wear resistance of tools for stamping. *Wear*. 2010;269(9–10): 693–697. <https://doi.org/10.1016/j.wear.2010.07.004>
2. Ivanov V.I., Burumkulov F.Kh. Strengthening and increasing the service life of objects using the electrospark deposition method: classification, features of the technology. *Elektronnaya obrabotka materialov*. 2010;5:27–36. (In Russ.).
3. Ivanov V.I. Increasing the service life of separation dies by strengthening and restoring them by electric spark alloying; Diss. Cand Sci. (Eng.). Saransk: VNIITUVID “Remdetal”, 2000. (In Russ.).  
Иванов В.И. Повышение ресурса разделительных штампов путем упрочнения и восстановления их электроискровым легированием: Дис. ... канд. техн. наук. Саранск: ВНИИТУВИД «Ремдеталь», 2000.
4. Gadalov V.N., Gvozdev A.E., Starikov N.E., Romanenko D.N., Kalinin A.A., Filatov E.A., Makarova I.A., Vornacheva I.V. Increase of reliability of tooling and instrument of the stamping equipment. *Izvestiya Tul'skogo gosudarstvennogo universiteta. Tekhnicheskie nauki*. 2017;11(2):114–124. (In Russ.).  
Гадалов В.Н., Гвоздев А.Е., Стариков Н.Е., Романенко Д.Н., Калинин А.А., Филатов Е.А., Макарова И.А., Ворначева И.В. Повышение надежности оснастки и инструмента штампового оборудования. *Известия Тульского государственного университета. Технические науки*. 2017;11(2):114–124.
5. Kudryashov A.E., Levashov E.A., Aksenov L.B., Petrov V.M. Use of electric spark alloying technology and promising nanostructured electrode materials for improving the life of punching equipment. *Metallurgist*. 2010;54(7):514–522.  
Кудряшов А.Е., Левашов Е.А., Аксенов Л.Б., Петров В.М. Применение технологии электроискро-

- вого легирования и перспективных наноструктурированных электродных материалов для повышения стойкости штамповой оснастки. *Металлург.* 2010;8:44–50.
6. Tušek J., Kosec L., Lešnjak A., Muhič T. Electrospark deposition for die repair. *Metallurgiya.* 2012;51:17–20.
  7. Kuptsov K.A., Sheveyko A.N., Sidorenko D.A., Shtansky D.V. Electro-spark deposition in vacuum using graphite electrode at different electrode polarities: Peculiarities of microstructure, electrochemical and tribological properties. *Applied Surface Science.* 2021;566:150722. <https://doi.org/10.1016/j.apsusc.2021.150722>
  8. Kuptsov K.A., Antonyuk M.N., Sheveyko A.N., Shtansky D.V. Hydrophobic, anti-ice, wear- and corrosion-resistant C—(Ti)—PTFE coatings on Ti obtained by electrospark deposition using PTFE-impregnated graphite electrode. *Surface and Coatings Technology.* 2023;465:129621. <https://doi.org/10.1016/j.surfcoat.2023.129621>
  9. Kudryashov A.E., Kiryukhantsev-Korneev P.V., Mukanov S.K., Petrzhik M.I., Levashov E.A. The effect of electrospark deposition using zirconium electrodes on structure and properties of nickel-containing alloy obtained selective laser melting. *Powder Metallurgy and Functional Coatings.* 2022;3:63–77. (In Russ.). <https://doi.org/10.17073/1997-308X-2022-3-63-77>  
Кудряшов А.Е., Кируханцев-Корнеев Ф.В., Муканов С.К., Петржик М.И., Левашов Е.А. Влияние электроискровой обработки электродами из циркония на структуру и свойства никельсодержащего сплава, полученного селективным лазерным сплавлением. *Известия вузов. Порошковая металлургия и функциональные покрытия.* 2022;3:63–77. <https://doi.org/10.17073/1997-308X-2022-3-63-77>
  10. Tarel'nyk V.B., Paustovskii A.V., Tkachenko Y.G., Konoplianchenko E.V., Martsynkovskiy V.S., Antoszewski B. Electrode materials for composite and multilayer electrospark-deposited coatings from Ni—Cr and WC—Co alloys and metals. *Powder Metallurgy and Metal Ceramics.* 2017;55:585–595. <https://doi.org/10.1007/s11106-017-9843-2>
  11. Mukanov S.K., Baskov F.A., Petrzhik M.I., Levashov E.A. Electro-spark treatment with low-melting Al—Si and Al—Ca electrodes in order to improve wear and oxidation resistance of EP741NP alloy prepared by selective laser melting. *Metallurgist.* 2022;66:317–326. <https://doi.org/10.1007/s11015-022-01331-0>
  12. Renna G., Leo P., Casalino G., Cerri E. Repairing 2024 aluminum alloy via electrospark deposition process: A feasibility study. *Advances in Materials Science and Engineering.* 2018:8563054. <https://doi.org/10.1155/2018/8563054>
  13. Kandeva M., Kostadinov G., Penyashki T., Kamburov V., Petrzhik M., Elenov B., Nikolov A., Dimitrova R., Valkanov S. Abrasive wear resistance of electrospark coatings on titanium alloys. *Tribology in Industry.* 2022; 44:132–142. <https://doi.org/10.24874/ti.1143.06.21.09>
  14. Kostadinov G., Danailov P., Dimitrova R., Kandeva M., Penyashki T., Kamburov V., Nikolov A., Elenov B. Surface topography and roughness parameters of electrospark coatings on titanium and nickel alloys. *Applied Engineering Letters Journal of Engineering and Applied Sciences.* 2021;6:89–98. <https://doi.org/10.18485/aeletters.2021.6.3.1>
  15. Burkov A., Pyachin S. Investigation of WC—Co electrospark coatings with various carbon contents. *Journal of Materials Engineering and Performance.* 2014;23: 2034–2042. <https://doi.org/10.1007/s11665-014-0974-z>
  16. Burkov A., Pyachin S. Formation of WC—Co coating by a novel technique of electrospark granules deposition. *Materials & Design.* 2015;80:109–115. <https://doi.org/10.1016/j.matdes.2015.05.008>
  17. Barile C., Casavola C., Pappalettera G., Renna G. Advancements in electrospark deposition (ESD) technique: A short review. *Coatings.* 2022;12:1536. <https://doi.org/10.3390/coatings12101536>
  18. Kuz'min M.P., Chu P.K., Qasim A.M., Larionov L.M., Kuz'mina M.Yu., Kuz'min P.B. Obtaining of Al—Si foundry alloys using amorphous microsilica — Crystalline silicon production waste. *Journal of Alloys and Compounds.* 2019;806:806–813. <https://doi.org/10.1016/j.jallcom.2019.07.312>
  19. Kuz'min M.P., Kuz'mina M.Yu., Kuz'min P.B. Possibilities and prospects for producing silumins with different silicon contents using amorphous microsilica. *Transactions of Nonferrous Metals Society of China.* 2020;30(5):1406–1418. [https://doi.org/10.1016/S1003-6326\(20\)65306-7](https://doi.org/10.1016/S1003-6326(20)65306-7)
  20. Chengyong W., Xie Y., Zheng L., Qin Z., Tang D., Song Y. Research on the chip formation mechanism during the high-speed milling of hardened steel. *International Journal of Machine Tools and Manufacture.* 2014;79:31–48. <https://doi.org/10.1016/j.ijmachtools.2014.01.002>
  21. Dvornik M.I., Mikhailenko E.A. Production of WC—15Co ultrafine-grained hard alloy from powder obtained by VK15 alloy waste spark erosion in water. *Powder Metallurgy and Functional Coatings.* 2020;(3):4–16. (In Russ.). <https://doi.org/10.17073/1997-308X-2020-3-4-16>  
Дворник М.И., Михайленко Е.А. Создание ультрамелкозернистого твердого сплава WC—15Co из порошка, полученного электроэрозионным диспергированием отходов сплава VK15 в воде. *Известия*

- вузов. Порошковая металлургия и функциональные покрытия. 2020;(3):4–16.  
<https://doi.org/10.17073/1997-308X-2020-3-4-16>
22. Potanin A.Yu., Vorotilo S., Pogozhev Yu.S., Rupasov S.I., Lobova T.A., Levashov E.A. Influence of mechanical activation of reactive mixtures on the microstructure and properties of SHS-ceramics MoSi<sub>2</sub>–HfB<sub>2</sub>–MoB. *Ceramics International*. 2019;45(16):20354–20361.  
<https://doi.org/10.1016/j.ceramint.2019.07.009>
  23. Zamulaeva E.I., Sheveyko A.N., Kaplanskii Y.Y., Levashov E.A. Structure formation and tribological properties of Mo–Si–B–Hf electrospark coatings based on Mo<sub>2</sub>Ni<sub>3</sub>Si laves phase. *Materials*. 2022;15(16):5613.  
<https://doi.org/10.3390/ma15165613>
  24. Gitlevich A.E., Mikhailov V.V., Parkanskii N.Ya., Revutskii V.M. Electrospark deposition of metal surfaces. Kishinev: Shtiintsa, 1985. 196 p. (In Russ.).  
Гитлевич А.Е., Михайлов В.В., Парканский Н.Я., Ревуцкий В.М. Электроискровое легирование металлических поверхностей. Кишинев: Штиинца, 1985. 196 с.
  25. Nan Chen, Ren Luo, Huiwen Xiong, Zhiyou Li. Dense M2 high speed steel containing core-shell MC carbonitrides using high-energy ball milled M2/VN composite powders. *Materials Science and Engineering: A*. 2020;771(138628).  
<https://doi.org/10.1016/j.msea.2019.138628>
  26. Verkhoturou A.D., Podchernyaeva I.A., Pryadko L.F., Egorov F.F. Electrode materials for electrospark deposition. Moscow: Nauka, 1988. 200 p. (In Russ.).  
Верхотуров А.Д., Подчерняева И.А., Прядко Л.Ф., Егоров Ф.Ф. Электродные материалы для электроискрового легирования. М.: Наука, 1988. 200 с.
  27. Huyan F., Larker R., Rubin P. Effect of solute silicon on the lattice parameter of ferrite in ductile irons. *ISIJ International*. 2014;54:248–250.  
<https://doi.org/10.2355/isijinternational.54.248>
  28. Phase equilibrium diagrams of binary metal systems: Directory. Vol. 2. Ed. N.P. Lyakishev. Moscow: Mashinostroenie, 1997. 1024 p. (In Russ.).  
Диаграммы состояния двойных металлических систем: Справочник. В 3 т. Т. 2. Под общ. ред. Н.П. Лякишева. М.: Машиностроение, 1997. 1024 с.
  29. Phase equilibrium diagrams of binary metal systems: Directory. Vol. 3. Book 1. Ed. N.P. Lyakishev. Moscow: Mashinostroenie, 2001. 872 p. (In Russ.).  
Диаграммы состояния двойных металлических систем: Справочник. В 3 т. Т. 3. Кн. 1. Под общ. ред. Н.П. Лякишева. М.: Машиностроение, 2001. 872 с.
  30. Ozden M.G., Morley N.A. Laser additive manufacturing of Fe-based magnetic amorphous alloys. *Magnetochemistry*. 2021;7:20.  
<https://doi.org/10.3390/magnetochemistry7020020>
  31. Fakoori Hasanabadi M., Malek Ghaini F., Ebrahimnia M., Shahverdi H.R. Production of amorphous and nanocrystalline iron based coatings by electro-spark deposition process. *Surface and Coatings Technology*. 2015;270:95–101.  
<https://doi.org/10.1016/j.surfcoat.2015.03.016>
  32. Hamaguchi T., Nakamura R., Asano K., Wada T., Suzuki T. Diffusion of boron in an amorphous iron-boron alloy. *Journal of Non-Crystalline Solids*. 2023; 601:122070.  
<https://doi.org/10.1016/j.jnoncrysol.2022.122070>

## Information about the authors

**Amankeldy Akhmetov** – Engineer of Scientific Project of the Department of Powder Metallurgy and Functional Coatings (PM&FC), National University of Science and Technology “MISIS” (NUST MISIS).

<https://orcid.org/0000-0002-1606-838X>

E-mail: amanlaotero@gmail.com

**Zhanna V. Ereemeeva** – Dr. Sci. (Eng.), Professor of the Department of PM&FC, NUST MISIS.

<https://orcid.org/0000-0002-1790-5004>

E-mail: eremeeva-shanna@yandex.ru

**Alexander E. Kudryashov** – Cand. Sci. (Eng.), Leading Researcher at the Laboratory “In Situ Diagnostics of Structural Transformations” of Scientific-Educational Center of SHS (SHS-Center) of MISIS–ISMAN.

<https://orcid.org/0000-0001-6222-4497>

E-mail: aekudr@yandex.ru

## Информация об авторах

**Аманкельды Ахметов** – инженер научного проекта кафедры порошковой металлургии и функциональных покрытий (ПМиФП) Национального исследовательского технологического университета «МИСИС» (НИТУ МИСИС).

<https://orcid.org/0000-0002-1606-838X>

E-mail: amanlaotero@gmail.com

**Жанна Владимировна Еремеева** – д.т.н., профессор кафедры ПМиФП, НИТУ МИСИС.

<https://orcid.org/0000-0002-1790-5004>

E-mail: eremeeva-shanna@yandex.ru

**Александр Евгеньевич Кудряшов** – к.т.н., вед. науч. сотрудник лаборатории «In situ диагностика структурных превращений» Научно-учебного центра (НУЦ) СВС МИСИС–ИСМАН.

<https://orcid.org/0000-0001-6222-4497>

E-mail: aekudr@yandex.ru

**Pavel A. Loginov** – Cand. Sci. (Eng.), Senior Lecturer of the Department of PM&FC of NUST MISIS; Senior Research Scientist of the Laboratory “In situ Diagnostics of Structural Transformations” of SHS-Center of MISIS–ISMAN.  
<https://orcid.org/0000-0003-2505-2918>  
 E-mail: pavel.loginov.misis@list.ru

**Sergey D. Shlyapin** – Dr. Sci. (Eng.), Professor of the Department of Materials Science and Materials Processing Technology, Moscow Aviation Institute (National Research University); Lead Project Expert of NUST MISIS.  
<https://orcid.org/0000-0002-1323-2623>  
 E-mail: sshliapin@yandex.ru

**Marina E. Samoshina** – Cand. Sci. (Eng.), Head of the Division of Academic Degrees, Academic Secretary of NUST MISIS Dissertation Board.  
<https://orcid.org/0009-0000-2773-3122>  
 E-mail: samoshina@list.ru

**Evgeny A. Levashov** – Dr. Sci. (Eng.), Prof., Academic of the Russian Academy of Natural Science, Head of the Department of PM&FC of NUST MISIS, Head of SHS-Center of MISIS–ISMAN.  
<https://orcid.org/0000-0002-0623-0013>  
 E-mail: levashov@shs.misis.ru

**Павел Александрович Логинов** – к.т.н., ст. преподаватель кафедры ПМиФП НИТУ МИСИС; ст. науч. сотрудник лаборатории «In situ диагностика структурных превращений» НУЦ СВС МИСИС–ИСМАН.  
<https://orcid.org/0000-0003-2505-2918>  
 E-mail: pavel.loginov.misis@list.ru

**Сергей Дмитриевич Шляпин** – д.т.н., профессор кафедры «Материаловедение и технология обработки материалов» Московского авиационного института (национального исследовательского университета); ведущий эксперт по проектам НИТУ МИСИС.  
<https://orcid.org/0000-0002-1323-2623>  
 E-mail: sshliapin@yandex.ru

**Марина Евгеньевна Самошина** – к.т.н., начальник отдела ученых степеней, ученый секретарь диссертационного совета НИТУ МИСИС.  
<https://orcid.org/0009-0000-2773-3122>  
 E-mail: samoshina@list.ru

**Евгений Александрович Левашов** – д.т.н., акад. РАЕН, профессор, зав. кафедрой ПМиФП НИТУ МИСИС; директор НУЦ СВС МИСИС–ИСМАН.  
<https://orcid.org/0000-0002-0623-0013>  
 E-mail: levashov@shs.misis.ru

## Contribution of the authors

**A. Akhmetov** – conducting experiments, manuscript writing.

**Zh.V. Eremeeva** – investigating consolidation features of powder mixtures, analyzing the microstructure of electrode materials, participating in result discussions.

**A.E. Kudryashov** – exploring electrospray deposition characteristics using the specified electrodes and analyzing the microstructure of the resulting coatings; participating in result discussions.

**P.A. Loginov** – conducting research using transmission electron microscopy.

**S.D. Shlyapin** – drafting and editing the manuscript, participating in the discussion of the results.

**M.E. Samoshina** – editing the manuscript, participating in result discussions.

**E.A. Levashov** – conceptualizing the research, contributed to the drafting and editing of the manuscript, and participated in the discussion of the findings.

## Вклад авторов

**А. Ахметов** – проведение экспериментов, подготовка текста статьи.

**Ж.В. Еремеева** – исследование особенностей консолидации порошковых смесей, анализ микроструктуры электродных материалов, участие в обсуждении результатов.

**А.Е. Кудряшов** – исследование особенностей процесса электроисковой обработки рассматриваемыми электродами, анализ микроструктуры сформированных покрытий, участие в обсуждении результатов.

**П.А. Логинов** – исследование методом просвечивающей электронной микроскопии.

**С.Д. Шляпин** – составление и редактирование текста статьи, участие в обсуждении результатов.

**М.Е. Самошина** – редактирование текста статьи, участие в обсуждении результатов.

**Е.А. Левашов** – концептуализация проводимых исследований, составление и редактирование текста статьи, участие в обсуждении результатов.

*The article was submitted 01.12.2023, revised 22.01.2024, accepted for publication 24.01.2024*

*Статья поступила в редакцию 01.12.2023, доработана 22.01.2024, подписана в печать 24.01.2024*

UDC 669.717: 669.718: 621.9.048

<https://doi.org/10.17073/0021-3438-2024-2-70-84>

Research article

Научная статья



## Influence of manganese alloying on the structure and properties of electrospark coatings of EP741NP heat-resistant nickel LPBF alloy

S.K. Mukanov, M.I. Petrzhih, P.A. Loginov, E.A. Levashov

National University of Science and Technology “MISIS”

4 Bld. 1 Leninskiy Prosp., Moscow 119049, Russia

✉ Samat K. Mukanov (smukanov@misis.ru)

**Abstract:** The paper investigates the impact of Mn content (Mn = 0; 0.5; 0.6; 1; 1.5 at.%) in the composition of the electrodes of the Al–Ca–Mn system on the structure and properties of electrospark coatings formed on LPBF substrates made of EP741NP alloy. It was found that the highest weight gain of the substrate ( $5.8 \cdot 10^{-4}$  g) was recorded when the Al–7%Ca–1%Mn electrode with a low degree of supercooling of the melt ( $\Delta t = 5$  °C) was subject to electrospark treatment (EST). EST with this electrode with a fine eutectic structure enables the formation of coatings with minimal surface roughness ( $R_a = 3.51 \pm 0.14$  μm). The nanocrystalline structure of the coatings was confirmed by transmission electron microscopy, including HRTEM. Comparative tribological tests revealed that the coating with maximum hardness ( $10.7 \pm 0.8$  GPa) formed during EST with an electrode containing 1.5 at.% Mn had the minimal wear rate ( $1.86 \cdot 10^{-5}$  mm<sup>3</sup>/(N·m)). We proved that EST with Al–Ca–Mn electrodes enables to reduce the specific weight gain of the LPBF EP741NP alloy during isothermal ( $t = 1000$  °C) curing in air due to *in situ* formation of a complex thermal barrier layer consisting of oxides ( $\alpha$ -Al<sub>2</sub>O<sub>3</sub>, CaMoO<sub>4</sub>) and intermetallics ( $\gamma'$ -Ni<sub>3</sub>Al and  $\beta$ -NiAl). We determined the concentration limit of Mn (1.0 at.%) in the electrode, at which the barrier layer retains its integrity and functionality.

**Keywords:** heat-resistant nickel alloy, laser powder bed fusion (LPBF), electrospark treatment, wear resistance, oxidation resistance, thermal barrier layer.

**Acknowledgments:** This work was funded by the Ministry of Science and Higher Education of the Russian Federation under state research assignment (project No. 0718-2020-0034).

**For citation:** Mukanov S.K., Petrzhih M.I., Loginov P.A., Levashov E.A. Influence of manganese alloying on the structure and properties of electrospark coatings of EP741NP heat-resistant nickel LPBF alloy. *Izvestiya. Non-Ferrous Metallurgy*. 2024;30(2):70–84. <https://doi.org/10.17073/0021-3438-2024-2-70-84>

## Влияние легирования марганцем на структуру и свойства электроискровых покрытий на никелевом жаропрочном СЛС-сплаве ЭП741НП

С.К. Муканов, М.И. Петржик, П.А. Логинов, Е.А. Левашов

Национальный исследовательский технологический университет «МИСИС»

Россия, 119049, г. Москва, Ленинский пр-т, 4, стр. 1

✉ Самат Куандыкович Муканов (smukanov@misis.ru)

**Аннотация:** Исследовано влияние содержания марганца (Mn = 0; 0,5; 0,6; 1; 1,5 ат.%) в составе электродов системы Al–Ca–Mn на структуру и свойства электроискровых покрытий, сформированных на СЛС-подложках из сплава ЭП741НП. Обнаруже-

но, что наибольший привес массы подложки ( $5,8 \cdot 10^{-4}$  г) зафиксирован при электроискровой обработке (ЭИО) электродом Al–7%Ca–1%Mn, имеющим низкую степень переохлаждения расплава ( $\Delta t = 5$  °C). Процесс ЭИО данным электродом с тонкой эвтектической структурой позволяет формировать покрытия с минимальной шероховатостью поверхности ( $R_a = 3,51 \pm 0,14$  мкм). Нанокристаллическая структура покрытий была подтверждена методами просвечивающей электронной микроскопии, в том числе с высоким разрешением. По результатам сравнительных трибологических испытаний обнаружено, что наилучшей износостойкостью ( $1,86 \cdot 10^{-5}$  мм<sup>3</sup>/(Н·м)) обладает покрытие с максимальной твердостью (10,7±0,8 ГПа), сформированное в процессе ЭИО электродом с содержанием 1,5 ат.% Mn. Показано, что ЭИО электродами Al–Ca–Mn позволяет снизить удельный привес СЛС-сплава ЭП741НП при изотермической ( $t = 1000$  °C) выдержке на воздухе благодаря *in situ* формированию комплексного термобарьерного слоя, состоящего из оксидов ( $\alpha$ -Al<sub>2</sub>O<sub>3</sub>, CaMoO<sub>4</sub>) и интерметаллидов ( $\gamma'$ -Ni<sub>3</sub>Al,  $\beta$ -NiAl). Установлен предел концентрации Mn (1,0 ат.%) в электроде, при которой барьерный слой сохраняет свои целостность и функциональность.

**Ключевые слова:** жаропрочный никелевый сплав, селективное лазерное сплавление, электроискровая обработка, износостойкость, стойкость к окислению, термобарьерный слой.

**Благодарности:** Работа выполнена при финансовой поддержке Министерства науки и высшего образования РФ в рамках государственного задания (проект 0718-2020-0034).

**Для цитирования:** Муканов С.К., Петржик М.И., Логинов П.А., Левашов Е.А. Влияние легирования марганцем на структуру и свойства электроискровых покрытий на никелевом жаропрочном СЛС-сплаве ЭП741НП. *Известия вузов. Цветная металлургия*. 2024;30(2):70–84. <https://doi.org/10.17073/0021-3438-2024-2-70-84>

## Introduction

Gas turbine components play a key role in the operation of power generators [1; 2]. Nowadays, steam pressure is increased to 35 MPa and temperature — to 750 °C [3] (there are plans to raise it to 1000 °C in the future) to enhance efficiency and environmental protection in the working zone of power plants. For this reason, gas turbine blades [3] are made of nickel-based heat-resistant alloys (Inconel, GTD, MGA, etc.) that can function under severe conditions of high temperatures and centrifugal loads. The structure of classical nickel superalloys includes the face-centered cubic (FCC) matrix and strengthening  $\gamma'$ -phases [5]. Reasonable alloying of such a structure ensures excellent mechanical properties and creep resistance at elevated temperatures up to 1150 °C [6; 7].

However, temperature and vibration gradients, as well as the ingress of various kinds of abrasive into the working zone can lead to critical wear and premature turbine failure [8–10]. Therefore, improving the wear resistance of nickel superalloy parts is crucial for ensuring the reliability and durability of gas turbine blades. Various methods of deposition of coatings and/or modification of surfaces of item are used to achieve this objective. Deposition/synthesis of refractory phases (NiAl intermetallics, NiB borides [11], and Al<sub>2</sub>O<sub>3</sub>, Y<sub>2</sub>O<sub>3</sub>, ZrO<sub>2</sub> oxides [6; 12]) responsible for wear and oxidation resistance of coatings in various gas environments at elevated temperatures are used to prevent premature wear. One traditional method of surface hardening is plasma spraying of Tribaloy T-800 coatings [13] coatings onto the contact surface of casings. These coatings are based on a Co–Cr–Mo alloy system and structurally reinforced with Laves phases. However, such coatings are unstable due to difference in thermal expansion

coefficients of the microstructural constituents, which leads to cracks generation.

In addition, there is an issue of mutual diffusion of alloying elements at the interface between the coating and superalloy at high temperatures. It is solved by using thermal barrier coatings with increased oxidation resistance. They typically consist of an outer ceramic layer containing a basic oxide (ZrO<sub>2</sub> or Al<sub>2</sub>O<sub>3</sub>) stabilized with yttrium (6–9 wt.% Y<sub>2</sub>O<sub>3</sub>) so called YSZ [14] and are characterized with a porosity of 10–25 % and a low thermal conductivity ( $1.5–3.0$  W·m<sup>-1</sup>·K<sup>-1</sup>) [15]. Modern thermal barrier coatings [16] have a gradient microstructure in which each layer is obtained using different techniques.

The technique of electron-beam deposition of thermal barrier coatings is used to extend the service life of parts and assemblies made of superalloys. It also has its disadvantages due to low adhesion of the coating to the substrate [17].

The surface also can be protected from wear and oxidation by means of electrospark treatment (EST) with fusible Al-based electrodes. It is due to in-situ reaction finished by synthesis of intermetallics. This was found in [18] when Al–Si, Al–Ca–Si, Al–Ca–Mn electrodes were used for EST of EP741NP alloy obtained by laser powder bed fusion (LPBF). It was shown that during EST with these electrodes NiAl, Ni<sub>3</sub>Al, NiAl<sub>3</sub> hard intermetallics have been formed, increasing the wear resistance of EP741NP alloy by 4.5 times. In addition, the coating formed by the Al–Ca–Mn electrode showed excellent resistance to oxidation in air at  $t = 870$  °C, as dense and homogeneous CaAl<sub>2</sub>O<sub>4</sub> barrier layer was formed and the proportion of  $\beta$ -NiAl increased. When the annealing

temperature reached 1000 °C for 30 h, the investigated coating was found to change the oxidation kinetics from a linear law which is typical for SLM superalloy to a parabolic law. This effect is caused by the formation of a two-layer  $\text{Al}_2\text{O}_3/\text{CaMoO}_4$  protective barrier on the surface, which reduces the oxidation rate by 16 times.

When manganese has been added to aluminum alloys it leads to a positive impact on their mechanical properties and heat resistance. However, as its content exceeds 1.5 wt.%, coarse inclusions of the  $\text{Al}_x\text{Mn}$  phase in microstructure are released, significantly deteriorating casting properties [19; 20]. Therefore, it is extremely important to investigate the influence of Mn in composition of the electrode on the properties of electrospark coatings.

The purpose of the work was to study how Mn content within the Al–Ca–Mn electrode affects the structure and properties of coatings formed by electrospark treatment of SLM substrates made of EP741NP alloy.

## Materials and methods

As substrates we used parallelepiped-shaped samples with the size of  $4 \times 5 \times 15$  mm obtained by laser powder bed fusion from EP741NP alloy of the following composition, at.%:

Ni.....	55.38	Nb.....	1.62
Co.....	15.49	C.....	0.19
Al.....	10.84	Hf.....	0.08
Cr.....	10.03	B.....	0.08
Mo.....	2.29	Mg.....	0.05
Ti.....	2.18	Cr.....	0.017
W.....	1.75	Ce.....	0.003

Electrospark treatment of the nickel alloy additive surfaces was performed at the rotary motion of the electrode according to the scheme “electrode — cathode, substrate — anode” in the argon medium (99.998 %) at constant values of frequency, duration and pulse energy: 1920 Hz, 25  $\mu\text{s}$  and 48 mJ, respectively.

The composition of near-eutectic electrodes was chosen based on the analysis of the Al–Ca–Mn phase diagram [20]. The charge was melted in an electric furnace GF1100N2D (Graficarbo, Italy) using high purity materials (A99; Ca 99.99) and addition alloy Al–20 wt.% Mn. Core electrodes with a diameter of 3–4 mm, the composition of which is presented in Table 1, were prepared by sucking the melt into a quartz tube.

The kinetics of mass transfer during EST was investigated by the gravimetric method on a KERN 770 pre-

cision balance (Germany) with an accuracy of  $10^{-5}$  g. Differential scanning calorimetry (DSC) at a rate of 20 °K/min in a protective argon atmosphere was performed according to the scheme 25–700–25 (°C) on a DSC 404 C Pegasus calorimeter (“Netzsch”, Germany).

The microstructure and composition were studied on a S-3400N scanning electron microscope (“Hitachi”, Japan) equipped with a NORAN System 7 X-ray Microanalysis System spectrometer (“Thermo Scientific”, USA). The fine structure was analyzed using a JEM-2100 transmission electron microscope (TEM) (Jeol, Japan). The samples (lamellae) for TEM were cut by the focused ion beam (FIB) method on a Quanta 200 3D FIB instrument (“FEI Company”, USA). The X-ray diffraction (XRD) phase analysis was performed based on the spectra obtained on an automated DRON-4 diffractometer (“Burevestnik”, Russia) using monochromatic  $\text{CoK}\alpha$ -radiation in the range of angles  $2\theta$  from 10° to 130°.

Comparative tribological tests were performed using a reciprocating movement according to the “rod—plate” scheme on an automated Tribometer friction machine (“CSM Instruments”, Switzerland) in compliance with ASTM G 99-17 at room temperature. The ball with a diameter of 3 mm made of 100Cr6 steel (analog of ShKh15) was used as a counterbody. The following test conditions were met: the track length was 4 mm, the applied load was 2 N, and maximum speed was 5 cm/s. Surface roughness and wear track profiles were studied on a WYKO NT1100 optical profilometer (“Veeco”, USA). Mechanical properties (hardness and elastic modulus) were investigated on a Nano—HardnessTester (“CSM Instruments”, Switzerland) at a maximum load of 10 mN.

The resistance to high-temperature oxidation of electrospark coatings was evaluated by the sample weight gain after isothermal annealing at 1000 °C for

Table 1. **Composition of rod electrodes of the Al–Ca–Mn system**

Таблица 1. Состав стержневых электродов системы Al–Ca–Mn

Designation	Concentration of elements, at. %		
	Al	Ca	Mn
Al–5Ca	94.82	5.18	–
Al–7.5Ca–0.5Mn	92.00	7.5	0.50
Al–5.7Ca–0.6Mn	93.68	5.71	0.61
Al–7Ca–1Mn	92.00	7.00	1.00
Al–6.5Ca–1.5Mn	92.00	6.50	1.50

30 h in air. Oxidation annealing of the samples was conducted in a SNOL 7.2/1200 muffle electric furnace. After annealing with a duration of 0.25, 0.5, 0.75, 1, 2, 3, 4, 5 and then every 5 h samples were weighed at room temperature on ALC-210d4 Acculab analytical scales (USA) with an accuracy of  $10^{-5}$  g. Specific weight gain was calculated according to the formula

$$K = \Delta m / S_0, \quad (1)$$

where  $\Delta m$  is the difference between the masses of the sample before the test and after oxidation, mg;  $S_0$  is the total surface area of the sample before the test,  $\text{cm}^2$ .

## Results and discussion

The rod electrodes were studied using the DSC method (Fig. 1) to determine the temperatures of melting ( $t_M$ ) and solidification ( $t_S$ ). Melting proceeds in a single endothermic peak for all compositions, and when alloys containing more than 6.5 at.% Ca solidify, small exothermic effects associated with the precipitation of  $\text{Al}_{10}\text{CaMn}_2$  primary crystals from the melt are noticeable at temperatures higher than the main solidification exopeak.

The microstructure of quenched electrodes is highly dependent on the material composition. Fig. 1 and Table 2 demonstrate that Mn addition to the Al–Ca base electrode correlates with the formation of primary  $\text{Al}_4\text{Ca}$  crystals (Fig. 2). Solidification of the Al–5%Ca electrode starts with the formation of Al dendrites, 20–30  $\mu\text{m}$  in size, around which a double

eutectic with a composition of  $\text{Al}_{94}\text{Ca}_6$  crystallizes. Other electrode (Al–5.7%Ca–0.6%Mn) alloyed with manganese, solidifies with the formation of primary  $\text{Al}_4\text{Ca}$  crystals in the form of plates of the same size, as well as the  $\text{Al}_{10}\text{CaMn}_2$  phase and triple eutectics  $\text{Al}_{94.1}\text{Ca}_{5.3}\text{Mn}_{0.6}$ .

The microstructure of the Al–7.5Ca–0.5Mn electrode with the increased calcium content also contains primary  $\text{Al}_4\text{Ca}$  crystals in the form of plates, but their portion is higher, while the composition of the ternary eutectic is the same —  $\text{Al}_{94.2}\text{Ca}_{5.2}\text{Mn}_{0.6}$ . Comparing the compositions of electrodes and eutectics, we can conclude that manganese is not found in the primary crystals of the Al–7.5Ca–0.5Mn electrode and is part of eutectic. The microstructure of the Al–7Ca–1Mn electrode contains plates of primary  $\text{Al}_4\text{Ca}$  crystals,  $\text{Al}_{10}\text{CaMn}_2$  particles, and eutectic with a composition of  $\text{Al}_{94.3}\text{Ca}_{5.3}\text{Mn}_{0.4}$ . The Al–6.5Ca–1.5Mn electrode has the same microstructure, only with a higher volume

Table 2. Composition and DSC results of Al–Ca–Mn electrodes

Таблица 2. Состав и результаты ДСК электродов Al–Ca–Mn

Electrode	$t_M$ , °C	$t_S$ , °C	$\Delta t = t_M - t_S$ , °C
Al–5Ca	622	609	13
Al–5.7Ca–0.6Mn	620	607	13
Al–7.5Ca–0.5Mn	619	612	7
Al–7Ca–1Mn	616	611	5
Al–6.5Ca–1.5Mn	617	606	11

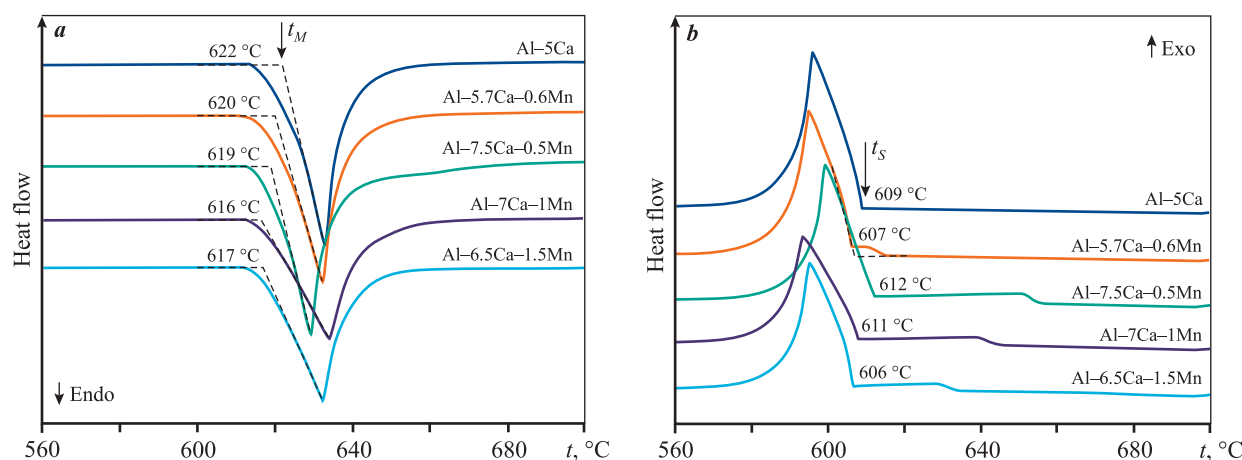
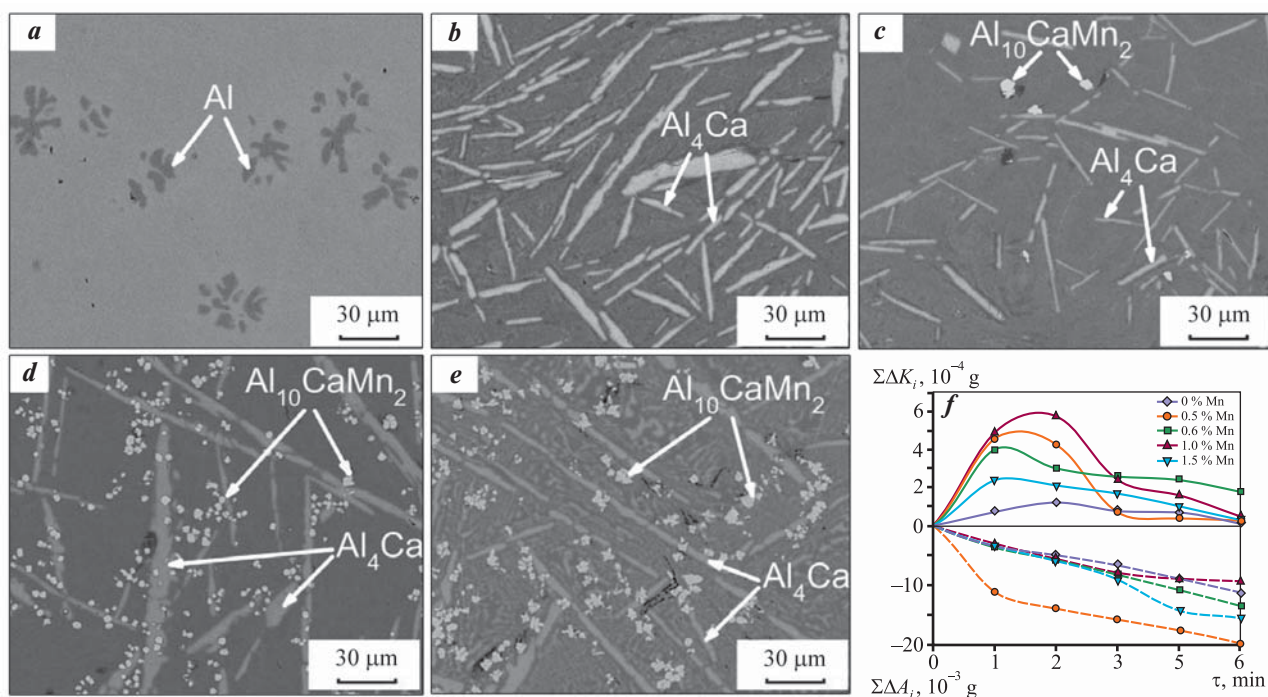


Fig. 1. Thermograms of Al–Ca–Mn rod electrodes  
a – melting curves, b – solidification curves

Рис. 1. Термограммы стержневых электродов Al–Ca–Mn  
a – кривые плавления, b – кривые затвердевания



**Fig. 2.** SEM images of the electrode structure Al–5Ca (*a*), Al–7.5Ca–0.5Mn (*b*), Al–5.7Ca–0.6Mn (*c*), Al–7Ca–1Mn (*d*), Al–6.5Ca–1.5Mn (*e*) and kinetic curves of electrode mass transfer on Ni substrate (*f*)

**Рис. 2.** РЭМ-изображения структуры электродов Al–5Ca (*a*), Al–7,5Ca–0,5Mn (*b*), Al–5,7Ca–0,6Mn (*c*), Al–7Ca–1Mn (*d*), Al–6,5Ca–1,5Mn (*e*), кинетические кривые массопереноса электродов на Ni-подложку (*f*)

fraction of  $\text{Al}_{10}\text{CaMn}_2$  particles and coarser ternary eutectic.

The kinetic curves of mass transfer during EST of EP741NP alloy with electrodes with different Mn content are presented in Fig. 2, *f*. All of them are of an extreme nature. The highest substrate weight gain ( $\Delta K = 5.8 \cdot 10^{-4}$  g) was recorded after 2 minutes of treatment using the near-eutectic Al–7Ca–1Mn electrode that contains small  $\text{Al}_{10}\text{CaMn}_2$  particles in its microstructure (see Fig. 2, *d*) and has a low degree of supercooling ( $\Delta t = 5$  °C) (see Table 2). The electrode erosion ( $\Delta A$ ) is slightly higher (Fig. 2, *f*) than the cathode weight gain ( $\Delta K$ ). There is no clear correlation between these parameters, which indicates a significant dispersion of erosion products (molten metal) in the interelectrode gap.

Figure 3 presents images of the microstructure of electrospark coatings on cross sections. The coatings formed during EST with electrodes, their Mn content (at.%) amounting to 0, 0.5, and 0.6, consist of submicron spherical particles. Near the coating surface, their size is less than 1  $\mu\text{m}$  and it increases towards the substrate (Fig. 3, *a–c*). The submicron structure of the electrospark layers indicates that after local melting when exposed to electric discharges, the melt cooling rate reaches  $10^5$ – $10^6$  K/s [21].

The thickness of the investigated electrospark coatings depends on the electrode composition and varies from 11 to 22  $\mu\text{m}$ . After treatment with an electrode containing 1.5 at.% Mn (Fig. 3, *d*), the coating has a layered structure. The near-surface layer of this sample, as well as other ones (Fig. 3, *a–c*), consists of well-connected particles smaller than 1  $\mu\text{m}$ . The bottom layer, however, is formed of columnar crystals oriented along the direction of heat removal. The ratio of Ni to Al in the electrospark coating varies with depth: closer to the surface, Al content is higher and as the substrate nears, the amount of Ni increases. According to the EDS data, the highest Mn concentrations (0.9–1.0 at.%) along with Ca (3.4–3.9 at.%) were found in the dark coating areas, whereas the light areas correspond to  $\beta$ -NiAl.

Figure 4 shows the structural constituents of the coating formed during EST with the Al–7%Ca–1%Mn fusible electrode. Its thickness, as well as that of the coating formed with the Al–7.5Ca–0.5Mn electrode (Fig. 3, *c*), is within  $\sim 15$   $\mu\text{m}$ , and the microstructure includes the regions (Fig. 4, *a*, zone *I*) formed as a result of concentration stratification of the melt. This structure feature is characteristic of the coatings formed by the electrodes with low degree of supercooling – Al–7.5Ca–0.5Mn (7 °C) and Al–7Ca–1Mn (5 °C).

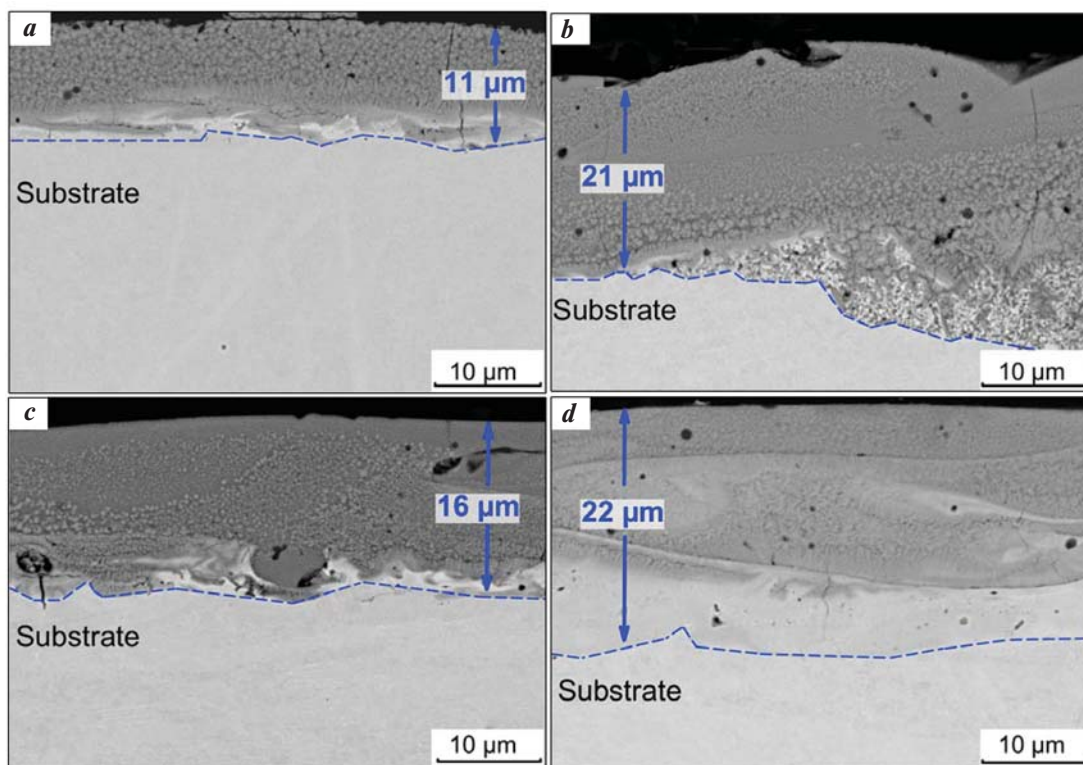


**Fig. 3.** SEM images of the microstructure of electrospark coatings obtained during EST with electrodes Al–5Ca (*a*), Al–5.7Ca–0.6Mn (*b*), Al–7.5Ca–0.5Mn (*c*) and Al–6.5Ca–1.5Mn (*d*)

**Рис. 3.** РЭМ-изображения микроструктуры электроискровых покрытий, полученных при ЭИО электродами Al–5Ca (*a*), Al–5,7Ca–0,6Mn (*b*), Al–7,5Ca–0,5Mn (*c*) и Al–6,5Ca–1,5Mn (*d*)

Figure 4, *b* shows that the electrode made of Al–7Ca–1Mn alloy is used to form a coating with a layered structure, which can be divided into two characteristic zones. Zone *I* consists of crystallites with a transverse grain size of 1.0–1.5 μm. Fig. 4, *c* demonstrates that the grains contain spherical nanoscale particles distributed in interlayers (indicated by white arrows). The average thickness of interlayers (strips) in which nanoparticles are found is less than 10 nm. According to the EDS data, their elemental composition does not differ from that of the matrix and they possibly represent shear strips. These interlayers are mostly oriented along the direction of heat removal (perpendicular to the substrate). The HRTEM image (inset *A*) shows that the particles have a diameter of about ~20 nm. The Fourier transform of the particles' images along the zone axis [011] (Fig. 4, inset *B*) revealed that the particles are isostructural to calcium oxide CaO.

In zone *II*, the grains are ~3.5 μm long and have an elongated shape. The direction of the columnar crystallite growth coincides with that of heat removal. Increased concentrations of Al (53.2 at.%), Ca (1.4 at.%) and Mn (0.5 at.%) are observed in this region, but Ni content shrinks (28.3 at.%). According to the TEM

diffraction pattern in region II (insert *C*), the values of interplane distances (1.99 nm and 2.82 nm) correspond to Ni<sub>2</sub>Al<sub>3</sub> trigonal syngony with the  $P\bar{3}m1$  space group.

According to the linear EDS analysis data obtained in the mode of scanning transmission electron microscope, the particles are enriched with calcium (Fig. 5), while the concentrations of all other elements (Al, Ni, Co, Cr) sharply drop. The Ca content reaches 30 at.% and that of oxygen — 19.4 at.%. This is consistent with the HRTEM findings (Fig. 4, inset *B*) indicating that the particles are a complex oxide of the (CaMe)O type. The formation of these particles during EST may be attributed to the reduction of metal oxides by calcium, which has a high affinity for oxygen [22].

Figure 6 shows that manganese alloying also leads to an increase in hardness (from 7.6±0.5 to 10.7±0.8 GPa) and elastic modulus (from 152±41 to 181±16 GPa).

The results of comparative tribological tests presented in Fig. 6, *b, c* and Table 3 prove that Mn introduction into the electrode significantly enhances the wear resistance of electrospark coatings, but hardly affects the coefficient of friction, the average value of

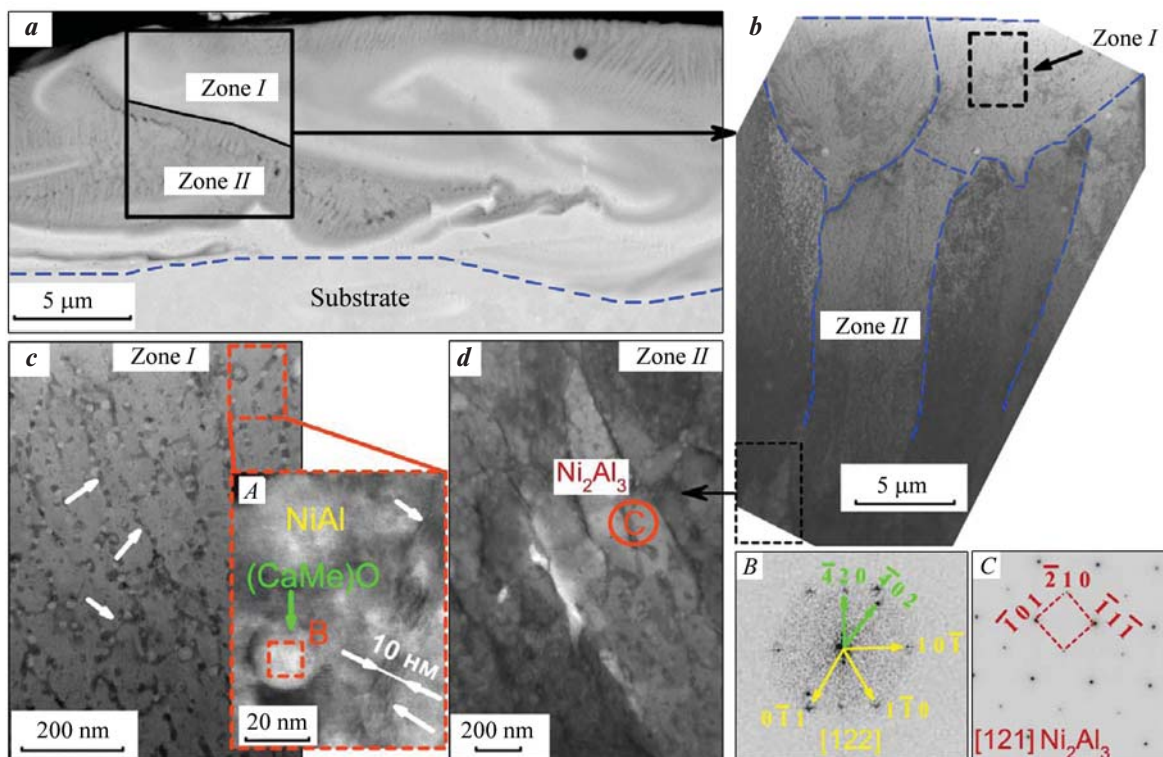


**Fig. 4.** Microstructure (a); TEM image of the lamella (b) and enlarged images of the corresponding coating zones (c, d) formed by the Al–7Ca–1Mn electrode

A – HRTEM of (CaMe)O nanoparticles in the NiAl matrix; B and C – TEM diffraction patterns of the corresponding regions

**Рис. 4.** Микроструктура (a), ПЭМ-изображение ламели (b) и увеличенные изображения соответствующих зон покрытия (c, d), сформированного электродом Al–7Ca–1Mn

A – ПЭМ ВР наночастиц (CaMe)O в NiAl-матрице; B и C – дифракционные картины ПЭМ соответствующих областей

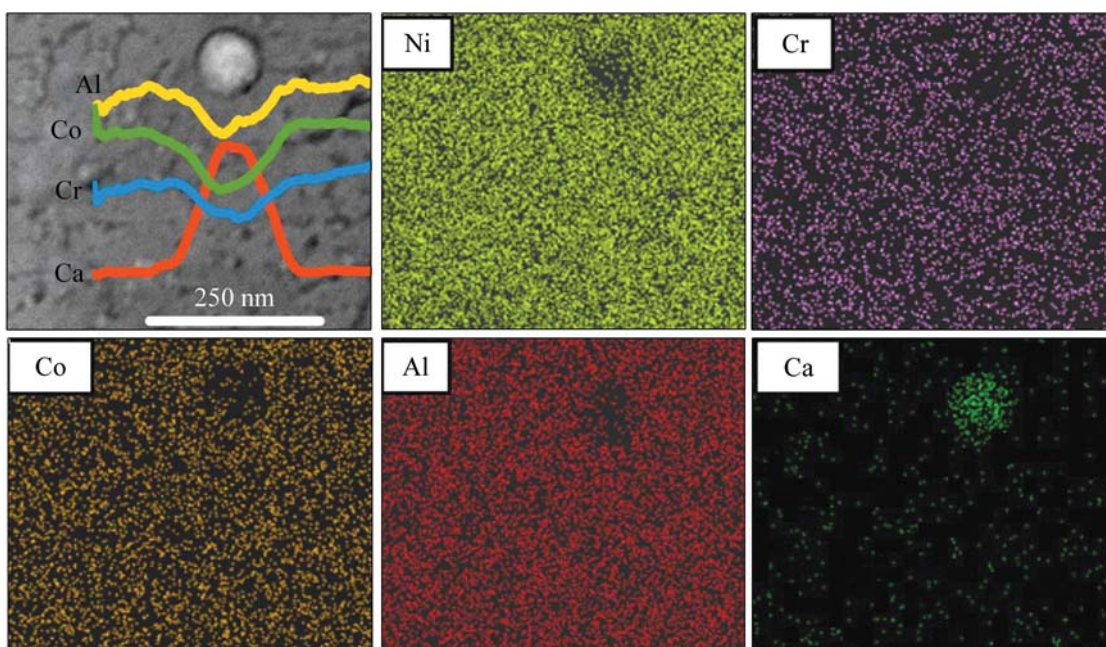


**Fig. 5.** TEM EDS spectra and the map of elemental distribution of (CaMe)O nanoparticle in the NiAl matrix

**Рис. 5.** ПЭМ ЭДС-спектры и карта распределения элементов наночастицы (CaMe)O в NiAl-матрице

which correlates with the surface roughness. Its value was the lowest (0.27) when the electrospark coating was tested with minimal surface roughness ( $R_a = 3.51 \pm 0.14 \mu\text{m}$ ), which was formed during EST with the Al–7Ca–1Mn electrode with a thin eutectic structure (see Fig. 2, d).

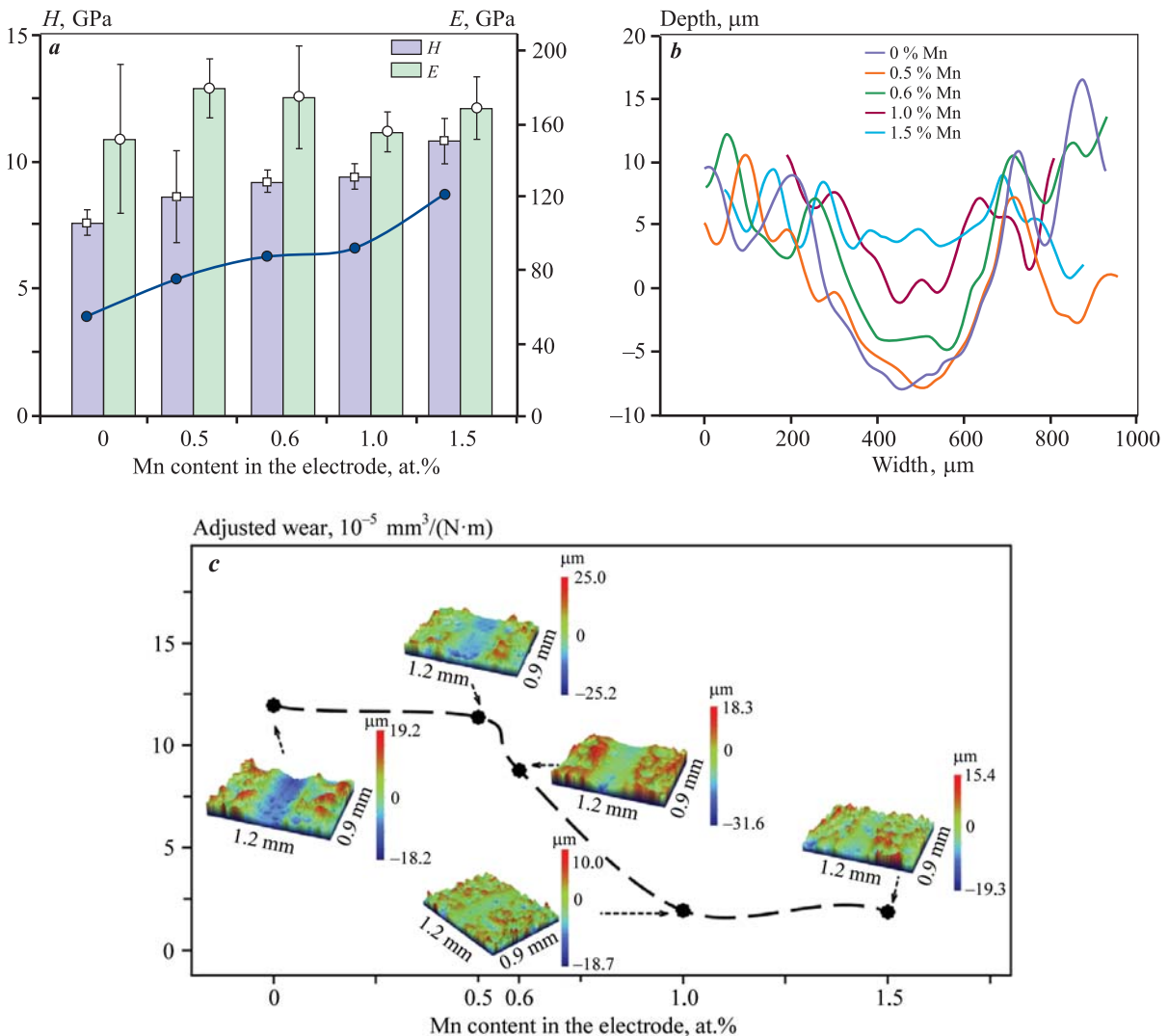
Figure 6, b, c shows that wear resistance of samples subjected to EST significantly improves with an increase in the Mn content in the electrode from 0.5 to 1 at.% Mn. However, the increase in Mn concentration by more than 1 at.% does not result in a considerable surge of this indicator.

Figure 7 demonstrates the oxidation kinetic curves of the samples with electrospark coatings. We can see that EST enables to reduce the specific weight gain of

EP741NP SLM alloy, which indicates a decreased oxidation rate. The kinetic curves of oxidation of the sample with 1.5 at.% Mn show a sharp increase in the mass after 10 h of isothermal curing. This is attributed to the violation of the oxidized coating integrity and unimpeded diffusion of oxygen into the substrate. The kinetic curves of oxidation of electrospark surfaces obtained during EST with Al–Ca–Mn electrodes, the Mn content amounting to 0, 0.5 and 1.0 at.%, present parabolic dependence [23; 24]:

$$(\Delta m/S)^n = kt, \quad (2)$$

where  $\Delta m/S$  is the mass gain per unit area,  $\text{mg}/\text{cm}^2$ ;  $k$  is the oxidation reaction rate constant;  $n$  is the oxidation reaction index;  $t$  is the oxidation time, h.



**Fig. 6.** Influence of the Mn content in the Al–Ca–Mn electrode composition on mechanical (a) and tribological (b, c) properties of electrospark coatings

**Рис. 6.** Влияние содержания Mn в составе Al–Ca–Mn-электрода на механические (a) и трибологические (b, c) свойства электроискровых покрытий

**Table 3. Tribological characteristics and surface roughness of samples with coatings obtained during EST with Al–Ca–Mn electrodes**

Таблица 3. Трибологические характеристики и шероховатость поверхности образцов с покрытиями, полученными при ЭИО электродами Al–Ca–Mn

Mn content in the electrode, at.%	Adjusted wear, $10^{-5} \text{ mm}^3/(\text{N} \cdot \text{m})$	Friction coefficient				$R_a, \mu\text{m}$
		Init.	Max.	Av.	Final	
0	11.95	0.27	0.45	0.29	0.28	$4.38 \pm 0.57$
0.5	11.37	0.15	0.46	0.30	0.27	$4.33 \pm 0.17$
0.6	8.78	0.07	0.52	0.31	0.31	$4.87 \pm 0.87$
1.0	1.93	0.09	0.40	0.27	0.28	$3.51 \pm 0.14$
1.5	1.86	0.37	0.47	0.29	0.28	$4.04 \pm 0.15$

To confirm the validity of the parabolic law of oxidation and to find the constants of equation (2), we used the approximation of oxidation curves, the results of which are presented in Table 4. The regression analysis of kinetic curves showed that treatment with electrodes, the Mn content ranging from 0 to 1.0 at.%, changes the oxidation mechanism from linear to parabolic. The analysis validity is confirmed by the values of the approximation coefficient which are close to unity: 0.9604–0.9846.

X-ray phase analysis was only performed on the samples which oxide layer was not destroyed during oxidation annealing (Table 5). Electrospark coatings subjected to isothermal oxidation annealing include the same phases. As the Mn content in the electrode increases, so does the proportion of calcium molybdate  $\text{CaMoO}_4$  in them. However, the predominant phase in the surface layers of samples treated with electrodes without Mn and with 0.5 % Mn is  $\text{Ni}_3\text{Al}$ , whereas the oxidized layer of the coating obtained using an electrode with 1 % Mn is characterized by a large proportion of  $\alpha\text{-Al}_2\text{O}_3$  and  $\text{CaMoO}_4$ . This can be attributed to the smaller thickness of the oxide layers of the first two samples, which resulted in an increased relative intensity of the X-ray reflections from the substrate.

The surface layers of the above coatings also contain  $\text{NiAl}_2\text{O}_4$  phases and insignificant amounts of NiO. The formation of  $\text{NiAl}_2\text{O}_4$  spinel and the reduced share of  $\alpha\text{-Al}_2\text{O}_3$  on the surface of these samples can be put down to the interaction of aluminum oxide and nickel following the chemical reaction

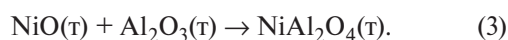


Figure 8 shows the microstructures of cross sections of coatings oxidized at  $t = 1000 \text{ }^\circ\text{C}$  during isothermal annealing for 30 h. The surface of all samples had a thin layer of variable thickness of 2.0–3.5  $\mu\text{m}$  of tetragonal  $\text{CaMoO}_4$  phase grains, the layer thickness not depend-

ing on the Mn content. Below is a layer of  $\alpha\text{-Al}_2\text{O}_3$ , the thickness varying from 12.5 to 15.0  $\mu\text{m}$ , in which  $\text{CaMoO}_4$  regions are distributed, and light gray inclusions are found that have the following components, at. %: O – 71.1, Al – 8.0, Ti – 10.6, Nb – 4.6, Cr – 3.1, Ni – 1.4 and Co – 1.1.

Under the  $\alpha\text{-Al}_2\text{O}_3$  layer, in the heat affected zone of the substrate, an oxygen-free region consisting of  $\gamma\text{-Ni}_3\text{Al}$  and  $\beta\text{-NiAl}$  is located, which is consistent with the XRD results. Beneath it, a band of white elongated precipitations is visible at a distance of 30–50  $\mu\text{m}$  from the surface. EDS-analysis of fragments of this band showed an increased content of refractory elements, at. %: Co – 16.4, Cr – 14.9, Mo – 12.9 and W – 11.1. Such structures are characteristic of oxidized nickel alloys [25] and are called “topologically close packed” (TCP) phases.

It was not possible to correctly estimate the thickness of the oxide layer of the sample treated with an electrode with 1.5 % Mn due to its delamination (see inset *B* in Fig. 7). As a result of delamination, the thickness decreased (Fig. 8, *d*) and the integrity of the protective layer was violated causing unimpeded diffusion of oxygen deep into the nickel substrate, which is confirmed by the linear nature of oxidation (see Fig. 7). A distinctive feature of the initial electrospark coating (Fig. 8, *d*) formed with the electrode with 1.5 % Mn is a layered structure. As a result of the preferential grain boundary oxygen diffusion during annealing, fracture is registered at the interface boundaries between layers. The longitudinal crack along which the oxide layer delaminated is highlighted by blue arrows. According to the EDS data, delamination is most frequent in the regions with low aluminum content. This can probably be attributed to the low cohesion of the formed electrospark coating (see Fig. 3, *d*) due to its structural defects. Its distinctive feature is the increased the Mn content (up to 1.0 at. %), while in other samples it did not exceed 0.5 at. %.

Table 4. Parameters of the equation of kinetic oxidation curves regression at 1000 °C temperature of the coatings formed by Al–Ca–Mn electrodes

Таблица 4. Параметры уравнения регрессии кинетических кривых окисления при температуре 1000 °C покрытий, сформированных электродами Al–Ca–Mn

Mn content in the electrode, at. %	Time interval, h	Regression equation	Confidence coefficient of approximation	Oxidation rate, 10 <sup>-4</sup> mg/(cm <sup>2</sup> ·s)
Substrate (EP741NP)	0 < τ < 5	$\Delta m/S = 0.278\tau^{0.5}$	0.9814	3.2
Substrate (EP741NP)	5 ≤ τ ≤ 30	$\Delta m/S = 1.2176\tau - 1.8144$	0.9970	3.2
0	0 ≤ τ ≤ 30	$\Delta m/S = 0.5022\tau^{0.5}$	0.9846	0.3
0.5	0 ≤ τ ≤ 30	$\Delta m/S = 0.3803\tau^{0.5}$	0.9604	0.2
0.6	0 ≤ τ ≤ 30	$\Delta m/S = 0.3863\tau^{0.5}$	0.9875	0.2
1.0	0 < τ ≤ 30	$\Delta m/S = 0.5621\tau^{0.5}$	0.9805	0.3
1.5	0 < τ < 5	$\Delta m/S = 0.4535\tau^{0.5}$	0.9506	3.1
1.5	15 ≤ τ ≤ 30	$\Delta m/S = 0.278\tau^{0.5}$	0.9635	3.1

Table 5. Phase composition of oxide layers of the coatings formed after 30 h of isothermal curing at t = 1000 °C in air

Таблица 5. Фазовый состав оксидных слоев покрытий, сформированных после 30 ч изотермической выдержки при t = 1000 °C на воздухе

Mn content in the electrode, at. %	Phase	Structural type	Content, wt. %	Lattice period, nm	
				a	c
0	Ni <sub>3</sub> Al	cF4/1	39.4	0.3582	–
	α-Al <sub>2</sub> O <sub>3</sub>	hR10/1	21.6	0.4779	1.3005
	NiAl <sub>2</sub> O <sub>4</sub>	cF56/2	18.9	0.8130	–
	CaMoO <sub>4</sub>	tI24/16	15.3	0.5232	1.1427
	NiO	cF8/2	4.8	0.4184	–
0.5	Ni <sub>3</sub> Al	cF4/1	34.8	0.3582	–
	α-Al <sub>2</sub> O <sub>3</sub>	hR10/1	20.9	0.4777	1.3019
	CaMoO <sub>4</sub>	tI24/16	20.2	0.5230	1.1426
	NiAl <sub>2</sub> O <sub>4</sub>	cF56/2	18.3	0.8122	–
	NiO	cF8/2	5.8	0.4191	–
1.0	α-Al <sub>2</sub> O <sub>3</sub>	hR10/1	44.9	0.4752	1.2937
	CaMoO <sub>4</sub>	tI24/16	43.3	0.5203	1.1382
	Ni <sub>3</sub> Al	cF4/1	9.6	0.3585	–
	NiAl	cP2/1	2.2	0.2860	–

To thoroughly study the structure of oxide layers by the focused ion beam method, a lamella was cut from the cross section of the sample treated with the 1 % Mn electrode. Fig. 9 shows that the coating consisting of γ'- and β-phase grains with inclusions of spherical nanoparticles of (CaMe)O type was preserved under the oxide layer. In addition, at the grain boundaries there are conglomerates of particles, which, according to TEM data, are enriched with refractory ele-

ments, their composition corresponding to the formula Ni<sub>23.4</sub>Co<sub>21.7</sub>Cr<sub>17</sub>W<sub>16.2</sub>Mo<sub>12.4</sub>Al<sub>9.3</sub>.

The outer layer of the oxidized surface consists of large grains with interplanar distances ( $d_{101} = 0.48$  nm;  $d_{224} = 0.15$  nm), which corresponds to the scheelite-type CaMoO<sub>4</sub> phase with tetragonal crystal lattice  $I4_1/a$  (Fig. 9, e). According to the works [26; 27], this structure exhibits excellent thermal stability and ultra-low thermal conductivity (0.6–1.2 W·m<sup>-1</sup>·K<sup>-1</sup>) at

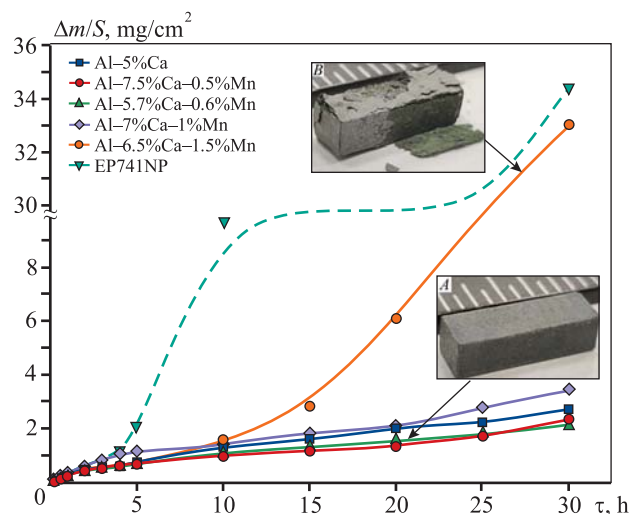


**Fig. 7.** Oxidation kinetic curves of the samples with coatings. The insets show the appearance of the samples obtained during EST with electrodes with 0.6 % Mn (A) and 1.5 % Mn (B)

**Рис. 7.** Кинетические кривые окисления образцов с покрытиями

На вставках показан внешний вид образцов, полученных при ЭИО электродами с 0,6 % Mn (A) и 1,5 % Mn (B)

$T = 400 \div 1000$  K, which is lower than that of thermal insulating layers for thermal barrier coatings such as YSZ ( $1.5 - 3 \text{ W} \cdot \text{m}^{-1} \cdot \text{K}^{-1}$ ).

The inner oxide layer in the sample subjected to EST with an electrode with 1 at.% Mn consists of equiaxed  $\alpha\text{-Al}_2\text{O}_3$  grains, about 400 nm in size. Nanoparticles up to 60 nm in size were found inside and at the periphery of the grains (Fig. 9, b, d). Based on the analysis of the HRTEM images, it can be assumed that they are nanoparticles of the  $\text{Mn}_2\text{AlO}_4$  phase. The inset to Fig. 9, d shows the image of particles after Fourier transform. It can be seen that these particles with the  $R\bar{3}m$  space group are coherent to the matrix of the  $\alpha\text{-Al}_2\text{O}_3$  ( $R\bar{3}C$ ) oxide layer.

The delamination of the oxide layer of the sample treated with an electrode with 1.5 at.% Mn can be attributed either to the formation of particles in the matrix, in which the Mn content is higher than in the  $\text{Mn}_2\text{AlO}_4$  phase, or to the supersaturation of this phase with manganese. The paper [28] confirms the first assumption. It shows that the presence of 1 at.% Mn in the electrode adversely affects the oxidation resistance of Ni–22Cr–14W–2Mo alloy as MnO particles form and reduce the strength of adhesion

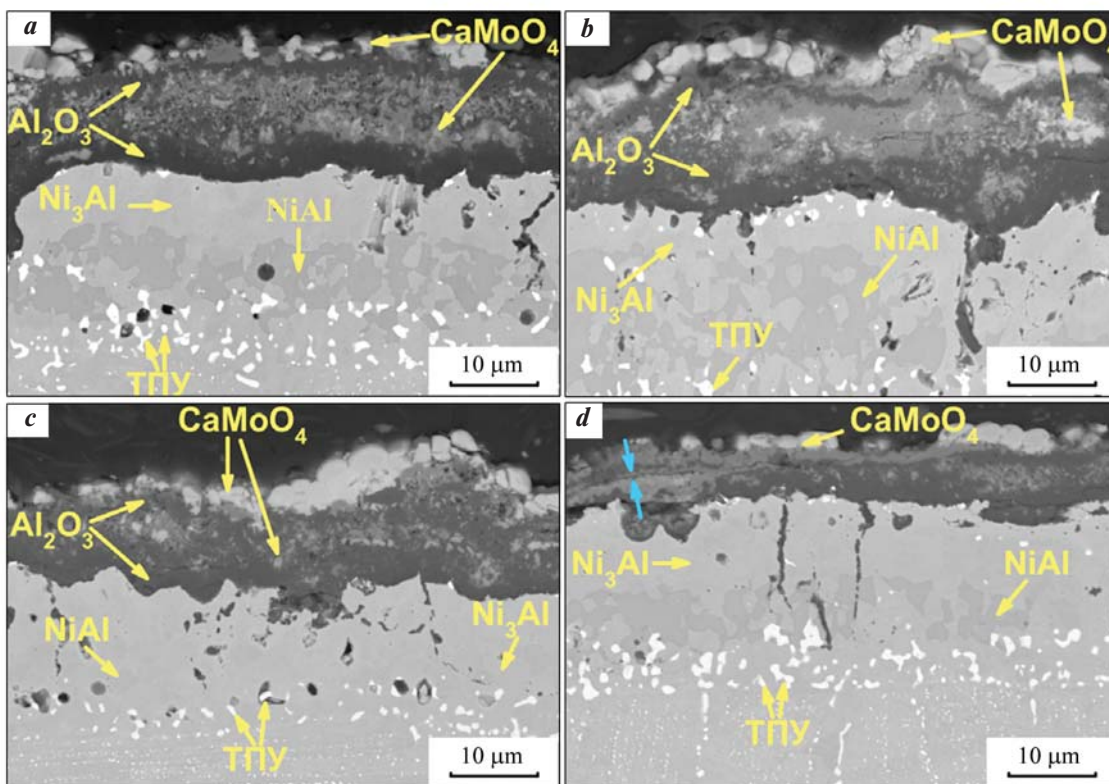


**Fig. 8.** SEM images of cross-sections of the samples with coatings obtained during EST with electrodes without Mn (a), and with the ones containing 0.5% Mn (b), 0.6% Mn (c), and 1.5% Mn (d), after 30 h of isothermal curing at  $t = 1000$  °C

**Рис. 8.** РЭМ-изображения поперечных шлифов образцов с покрытиями, полученными при ЭИО электродами без Mn (a) и содержащими 0,5 % Mn (b), 0,6 % Mn (c) и 1,5 % Mn (d), после 30 ч изотермической выдержки при  $t = 1000$  °C

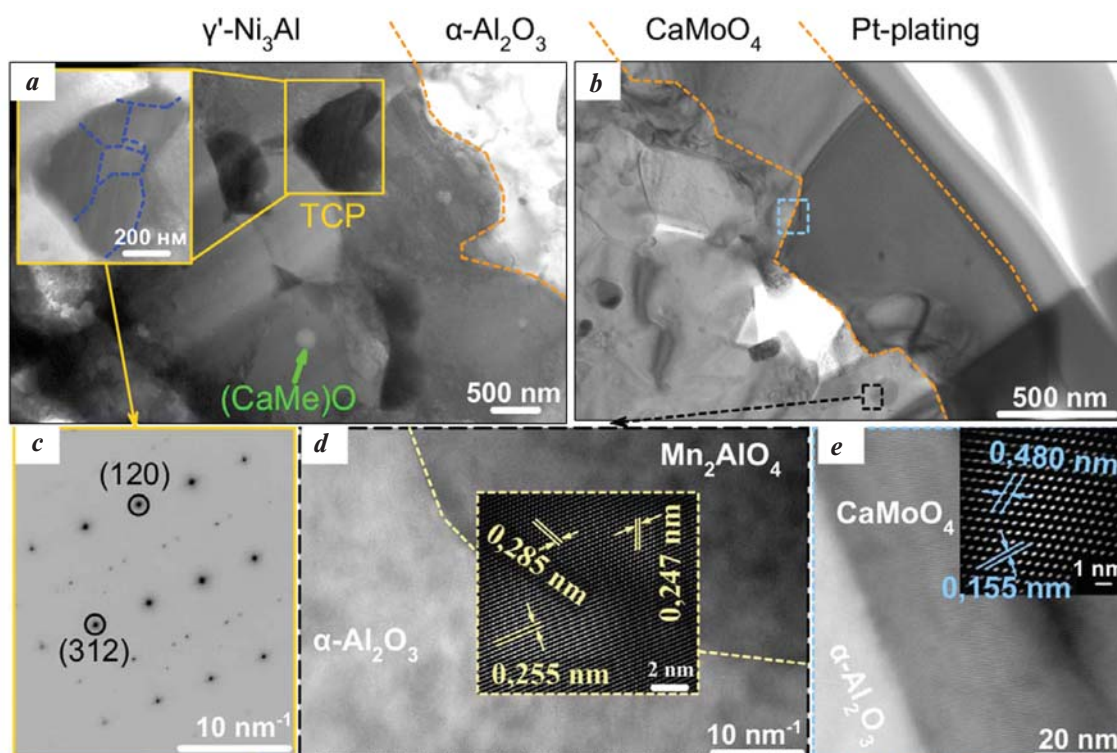


**Fig. 9.** TEM image of the structure of the 1 % Mn sample after 30 h of isothermal curing

*a* – boundary between the electrospark coating and  $\alpha$ - $\text{Al}_2\text{O}_3$ ; *b* – boundary between oxide layers of  $\alpha$ - $\text{Al}_2\text{O}_3$  and  $\text{CaMoO}_4$ ; *c* – diffraction pattern; *d, e* – HRTEM of the corresponding regions

**Рис. 9.** ПЭМ-изображение структуры образца, обработанного электродом с 1 % Mn, после 30 ч изотермической выдержки

*a* – граница между электроискровым покрытием и  $\alpha$ - $\text{Al}_2\text{O}_3$ ; *b* – граница между оксидными слоями  $\alpha$ - $\text{Al}_2\text{O}_3$  и  $\text{CaMoO}_4$ ; *c* – дифракционная картина; *d, e* – ПЭМ ВР-изображения соответствующих областей

between the  $\text{Cr}_2\text{O}_3$  layer and the substrate. In the second case, manganese supersaturation of the  $\text{Mn}_2\text{AlO}_4$  phase formed during annealing results in a change in the lattice parameter and accumulation of residual stresses at the interface [29] due to the dimensional mismatch between the crystal lattices of the phases causing loss of coherence and destruction of the oxide layer.

## Conclusions

1. The study of mass transfer kinetics during electrospark treatment of SLM samples made of EP741NP alloy with electrodes with different Mn content showed that the highest substrate mass gain ( $5.8 \cdot 10^{-4}$  g) was recorded when the near-eutectic Al–7%Ca–1%Mn alloy with a low degree of melt supercooling ( $\Delta t = 5$  °C) was used. During EST with the Al–6.5%Ca–1.5%Mn electrode, structural defects are formed and the Mn concentration in the coating reaches 1.0 at.%. For the other studied coatings, it did not exceed 0.5 at.%.

2. The results of tests revealed that wear resistance, hardness and modulus of elasticity enhance with in-

creasing manganese content in the coating. Increasing the mechanical properties start at manganese content of 0.5 at.% and its further growth up to 1.0 at.% leads also to a significant increase in wear resistance (adjusted wear of  $1.86 \cdot 10^{-5}$  mm<sup>3</sup>/(N·m)).

3. Electrospark treatment of EP741NP alloy with Al–Ca–Mn electrodes changes the oxidation kinetics from linear to parabolic. As the Mn content in the oxide layer increases, so does the volume fraction of calcium molybdate ( $\text{CaMoO}_4$ ) in the oxidative annealing process. However, as the manganese content in the electrode reaches 1.5 at.%, oxidation proceeds by a mixed mechanism and is accompanied by violation of the oxide layer integrity and unimpeded diffusion of oxygen deep into the nickel substrate. This can probably be put down to MnO particles forming in the oxide matrix and reducing the bonding strength of the oxide layer. Another explanation is that residual stresses accumulate due to the mismatch of the phases crystal lattice parameters and coherence is lost between  $\alpha$ - $\text{Al}_2\text{O}_3$  and  $\text{Mn}_2\text{AlO}_4$  nanoscale particles supersaturated with manganese.

## References

- De Barbadillo J.J. 14-Inconel alloy 740H. (Ed. A.Di Gianfrancesco). In: *Materials for ultra-supercritical and advanced ultra-supercritical power plants*. Sawston, Cambridge: Woodhead Publ., 2017. P. 469–510.  
<https://doi.org/10.1016/B978-0-08-100552-1.00014-2>
- Barella S., Boniardi M., Cincera S., Pellin P., Degive X., Gijbels S. Failure analysis of a third stage gas turbine blade. *Engineering Failure Analysis*. 2011;18(1):386–393.  
<https://doi.org/10.1016/j.engfailanal.2010.09.017>
- Yang M., Zhou Y., Yang J., Bao J., Wang D., Yu Q. Performance analysis of an efficient waste heat utilization system in an ultra-supercritical coal-fired power plant. *Energy Reports*. 2022;8: 5871–720.  
<https://doi.org/10.1016/j.egy.2022.04.044>
- Peng J.Q., Zhang H.T., Li Y.F. Review of blade materials for IGT. *Procedia Engineering*. 2015;130:668–675.  
<https://doi.org/10.1016/j.proeng.2015.12.295>
- Liang F., Meng A., Sun Y., Chen Zh., Jiang Zh., Zhang Y., Zhang Y., Zhu Y., Chen X. A novel wear-resistant Ni-based superalloy via high Cr-induced subsurface nanotwins and heterogeneous composite glaze layer at elevated temperatures. *Tribology International*. 2023;183:108383.  
<https://doi.org/10.1016/j.triboint.2023.108383>
- Kamalan Kirubaharan A.M., Kuppusami P., Ghosh Ch., Priya R., Ningshen S., Dinesh Kumar D., Divakar R. Metal-ceramic diffusion barrier nanocomposite coatings on nickel based superalloys for corrosion and high temperature oxidation resistance. *Ceramics International*. 2022;48:31281–31288.  
<https://doi.org/10.1016/j.ceramint.2022.06.203>
- Sanin V.V., Aheiev M.I., Kaplanskii Y.Y., Loginov P.A., Bychkova M.Y., Levashov E.A. The effect of dopants on structure formation and properties of cast SHS alloys based on nickel monoaluminide. *Materials*. 2023;16(9):3299.  
<https://doi.org/10.3390/ma16093299>
- Kurzynowski T., Smolina I., Kobiela K., Kuźnicka B., Chlebus E. Wear and corrosion behaviour of Inconel 718 laser surface alloyed with rhenium. *Materials & Design*. 2017;132:349–359.  
<https://doi.org/10.1016/j.matdes.2017.07.024>
- Behera A., Sahoo A.K. Wear behaviour of Ni based superalloy: A review. *Materials Today: Proceedings*. 2020;33(8):5638–5642.  
<https://doi.org/10.1016/j.matpr.2020.04.007>
- Yu W., Ming W., An Q., Chen M. Cutting performance and wear mechanism of honeycomb ceramic tools in interrupted cutting of nickel-based superalloys. *Ceramics International*. 2021;47(13):18075–18083.  
<https://doi.org/10.1016/j.ceramint.2021.03.123>
- Campos-Silva I., Contla-Pacheco A.D., Figueroa-López U., Martínez-Trinidad J., Garduño-Alva A., Ortega-Avilés M. Sliding wear resistance of nickel boride layers on an Inconel 718 superalloy. *Surface and Coatings Technology*. 2019;378:124862.  
<https://doi.org/10.1016/j.surfcoat.2019.06.099>
- Yang Sh., Gao S., Xue W., Wu B., Cheng H., Du-an D. Epitaxial growth and oxidation behavior of the NiCoCrAlYTa/Y<sub>2</sub>O<sub>3</sub> coating on a nickel-based single-crystal superalloy blade tips, produced by electro spark deposition. *Journal of Alloys and Compounds*. 2023;931:167600.  
<https://doi.org/10.1016/j.jallcom.2022.167600>
- Balaguru S., Gupta M. Hardfacing studies of Ni alloys: A critical review. *Journal of Materials Research and Technology*. 2021;10:1210–1242.  
<https://doi.org/10.1016/j.jmrt.2020.12.026>
- Jude S.A.A., Winowlin Jappes J.T., Adamkhan M. Thermal barrier coatings for high-temperature application on superalloy substrates — A review. *Materials Today: Proceedings*. 2022;60:1670–1675.  
<https://doi.org/10.1016/j.matpr.2021.12.223>
- Darolia R. Thermal barrier coatings technology: Critical review, progress update, remaining challenges and prospects. *International Materials Reviews*. 2013;58(6):315–348. <https://doi.org/10.1179/1743280413Y.0000000019>
- Jayalakshmi V., Subramanian K.R.V. Thermal barrier coatings: state-of-art developments and challenges: A mini review. *Transactions of the IMF*. 2022;100(1):6–9.  
<https://doi.org/10.1080/00202967.2021.1979813>
- Evans A.G., Clarke D.R., Levi C.G. The influence of oxides on the performance of advanced gas turbines. *Journal of the European Ceramic Society*. 2008;28(7): 1405–1419.  
<https://doi.org/10.1016/j.jeurceramsoc.2007.12.023>
- Mukanov S.K., Baskov F.A., Petrzhik M.I., Levashov E.A. Electro-spark treatment with low-melting Al–Si and Al–Ca electrodes in order to improve wear and oxidation resistance of EP741NP alloy prepared by selective laser melting. *Metallurgist*. 2022;66(3-4):317–326.  
<https://doi.org/10.1007/s11015-022-01331-0>  
Муканов С.К., Басков Ф.А., Петржик М.И., Левашов Е.А. Электроискровая обработка легкоплавкими электродами Al–Si и Al–Ca для повышения стойкости к износу и окислению сплава ЭП741НП, полученного селективным лазерным сплавлением. *Металлург*. 2022;3:70–77.
- Junwei Fu, Kai Cui Effect of Mn content on the microstructure and corrosion resistance of Al–Cu–Mg–Mn alloys. *Journal of Alloys and Compounds*. 2022;896:162903.  
<https://doi.org/10.1016/j.jallcom.2021.162903>
- Naumova E., Doroshenko V., Barykin M., Sviridova T., Lyasnikova A., Shurkin P. Hypereutectic Al–Ca–Mn–

- (Ni) alloys as natural eutectic composites. *Metals*. 2021;11:890. <https://doi.org/10.3390/met11060890>
21. Petrzhik M., Molokanov V., Levashov E. On conditions of bulk and surface glass formation of metallic alloys. *Journal of Alloys and Compounds*. 2017;707:68–72. <https://doi.org/10.1016/j.jallcom.2016.12.293>
  22. Arroyo-de Dompablo E., Ponrouch A., Johansson P., Palacín R. Achievements, challenges, and prospects of calcium batteries. *Chemical Reviews*. 2020;120(14):6331–6357. <https://doi.org/10.1021/acs.chemrev.9b00339>
  23. Potanin A.Yu., Astapov A.N., Pogozhev Yu.S., Rupasov S.I., Shvyndina N.V., Klechkovskaya V.V., Levashov E.A., Timofeev I.A., Timofeev A.N. Oxidation of HfB<sub>2</sub>–SiC ceramics under static and dynamic conditions. *Journal of the European Ceramic Society*. 2021;41(16):34–47. <https://doi.org/10.1016/j.jeurceramsoc.2021.09.018>
  24. Tian Sh., He A., Liu J., Zhang Y., Yang Y., Zhang Y., Jiang H. Oxidation resistance of TiAl alloy improved by hot-pack rolling and cyclic heat treatment. *Materials Characterization*. 2021;178:111196. <https://doi.org/10.1016/j.matchar.2021.111196>
  25. Zhou B., He J., Liu L., Wang S., Sun J., Wei L., Guo H. The interaction between Dy, Pt and Mo during the short–time oxidation of ( $\gamma'$  +  $\beta$ ) two-phase Ni–Al coating on single crystal superalloy with high Mo content. *Surface and Coatings Technology*. 2022;430:127999. <https://doi.org/10.1016/j.surfcoat.2021.127999>
  26. Bsaibess E., Delorme F., Monot-Laffez I., Giovannelli F. Ultra-low thermal conductivity in scheelite and A-deficient scheelite ceramics. *Scripta Materialia*. 2021;201:113950. <https://doi.org/10.1016/j.scriptamat.2021.113950>
  27. Ait Laasri H., Bsaibess E., Delorme F., Nataf G.F., Giovannelli F. Ultra-low lattice thermal conductivity in tungsten-based scheelite ceramics. *Journal of Alloys and Compounds*. 2023;955:170167. <https://doi.org/10.1016/j.jallcom.2023.170167>
  28. Yun D. W., Seo S.M., Jeong H.W., Yoo Y.S. The effects of the minor alloying elements Al, Si and Mn on the cyclic oxidation of Ni–Cr–W–Mo alloys. *Corrosion Science*. 2014;83:176–188. <https://doi.org/10.1016/j.corsci.2014.02.015>
  29. Zhou B., He J., Peng H., Sun J., Guo H. The influence of Hf content on oxide scale microstructure and HfO<sub>2</sub> formation mechanisms in two-phase ( $\gamma'$  +  $\beta$ ) Ni–Al alloys. *Materials Characterization*. 2022;184:111659. <https://doi.org/10.1016/j.matchar.2021.111659>

## Information about the authors

**Samat K. Mukanov** – Cand. Sci. (Eng.), Junior Research Scientist of the Laboratory “In situ Diagnostics of Structural Transformations” of Scientific Educational Center of Self-Propagating High-Temperature Synthesis (SHS-Center) of MISIS–ISMAN, National University of Science and Technology “MISIS” (NUST MISIS). <https://orcid.org/0000-0001-6719-6237>  
E-mail: smukanov@misis.ru

**Mikhail I. Petrzhik** – Dr. Sci. (Eng.), Professor of the Department of Powder Metallurgy and Functional Coatings (PM&FC) of NUST MISIS; Leading Research Scientist of the Laboratory “In situ Diagnostics of Structural Transformations” of SHS-Center of MISIS–ISMAN. <https://orcid.org/0000-0002-1736-8050>  
E-mail: petrzhik@shs.misis.ru

**Pavel A. Loginov** – Cand. Sci. (Eng.), Senior Lecturer of the Department of PM&FC of NUST MISIS; Senior Research Scientist of the Laboratory “In situ Diagnostics of Structural Transformations” of SHS-Center of MISIS–ISMAN. <https://orcid.org/0000-0003-2505-2918>  
E-mail: pavel.loginov.misis@list.ru

**Evgeny A. Levashov** – Dr. Sci. (Eng.), Prof., Academic of the Russian Academy of Natural Science, Head of the Department of PM&FC of NUST MISIS, Head of SHS-Center of MISIS–ISMAN. <https://orcid.org/0000-0002-0623-0013>  
E-mail: levashov@shs.misis.ru

## Информация об авторах

**Самат Куандыкович Муканов** – к.т.н., мл. науч. сотрудник лаборатории «In situ диагностика структурных превращений» Научно-учебного центра (НУЦ) СВС МИСИС–ИСМАН, Национальный исследовательский технологический университет «МИСИС» (НИТУ МИСИС). <https://orcid.org/0000-0001-6719-6237>  
E-mail: smukanov@misis.ru

**Михаил Иванович Петржик** – д.т.н., профессор кафедры порошковой металлургии и функциональных покрытий (ПМиФП) НИТУ МИСИС; вед. науч. сотрудник лаборатории «In situ диагностика структурных превращений» НУЦ СВС МИСИС–ИСМАН. <https://orcid.org/0000-0002-1736-8050>  
E-mail: petrzhik@shs.misis.ru

**Павел Александрович Логинов** – к.т.н., ст. преподаватель кафедры ПМиФП НИТУ МИСИС; ст. науч. сотрудник лаборатории «In situ диагностика структурных превращений» НУЦ СВС МИСИС–ИСМАН. <https://orcid.org/0000-0003-2505-2918>  
E-mail: pavel.loginov.misis@list.ru

**Евгений Александрович Левашов** – д.т.н., акад. РАЕН, профессор, зав. кафедрой ПМиФП НИТУ МИСИС; директор НУЦ СВС МИСИС–ИСМАН. <https://orcid.org/0000-0002-0623-0013>  
E-mail: levashov@shs.misis.ru

## Contribution of the authors

**S.K. Mukanov** – preparation and conduct of experiments, writing the text of the article, data analysis, visualization, discussion of the results.

**M.I. Petrzhih** – setting the purpose and objectives of the study, mechanical property research, data analysis, correcting the text, formulating conclusions.

**P.A. Loginov** – conducting transmission electron microscopy studies and discussing the results.

**E.A. Levashov** – forming the main concept, adjusting the text and conclusions.

## Вклад авторов

**С.К. Муқанов** – подготовка и проведение экспериментов, написание текста статьи, анализ данных, визуализация, обсуждение результатов.

**М.И. Петржи́к** – постановка цели и задачи исследования, исследование механических свойств, анализ данных, корректировка текста, формулировка выводов.

**П.А. Логинов** – проведение исследований методом просвечивающей электронной микроскопии, обсуждение результатов.

**Е.А. Левашов** – формирование основной концепции, корректировка текста и выводов.

---

*The article was submitted 26.03.2024, revised 22.04.2024, accepted for publication 26.04.2024*

*Статья поступила в редакцию 26.03.2024, доработана 22.04.2024, подписана в печать 26.04.2024*